MASTER'S THESIS ASSIGNMENT

I. Personal and study details

Student's name: **Klöser Daniel** Personal ID number: **456197**

Faculty / Institute: **Faculty of Electrical Engineering**

Department / Institute: **Department of Cybernetics**

Study program: **Cybernetics and Robotics**

Branch of study: **Robotics**

II. Master's thesis details

Master's thesis title in English:

Hierarchical Model Predictive Control for the Dynamical Power Split of a Fuel Cell Hybrid Vehicle

Master's thesis title in Czech:

Hierarchické prediktivní řízení pro dynamické rozdělení výkonu hybridních vozidel s palivovými články

Guidelines:

- Topic of the thesis is to develop and implement a hierarchical model predictive control of a Fuel Cell Hybrid Vehicle (FCHV)
- High level controller: Optimize the power split between battery and fuel cell system based on the predicted power demand and current state of the vehicle such as hydrogen state-of-charge (SOC) and efficiencies of the fuel cell and battery systems
- Low Level Controller: Dynamic power split between battery and fuel cell system in order to provide the demanded power with high dynamics and ensure a safe and energy efficient operation
- The controller will be implemented within Simulink into a model of a FCHV based on Stefanopoulou et. al [1]
- Evaluation based on Standard Drive Cycles such as WLTC3

Bibliography / sources:

[1] Jay T. Pukrushpan, Anna G. Stefanopoulou and Huei Peng, Control of Fuel Cell Power Systems, Springer, 2005.
[2] R. K. Ahluwalia and X. Wang, “Fuel cell systems for transportation: Status and trends”, Journal of Power Sources, vol. 177, no. 1, pp. 167–176, 2008.
[3] J. T. Pukrushpan, A. G. Stefanopoulou, and H. Peng, Control of Fuel Cell Power Systems: Principles, modeling, analysis and feedback design, 2. printing, ser. Advances in industrial control. London: Springer, 2005.
[4] D. P. Bertsekas, Dynamic programming and optimal control, 3. ed., ser. Athena scientific optimization and computation series. Belmont, Mass.: Athena Scientific, 2005, vol. 3.

Name and workplace of master's thesis supervisor:

Philip von Platen, M.Sc., RWTH Aachen University

Name and workplace of second master's thesis supervisor or consultant:

Ing. Martin Hlinovský, Ph.D., Department of Control Engineering, FEE

Date of master's thesis assignment: **05.02.2019** Deadline for master's thesis submission: **07.06.2019**

Assignment valid until: **30.09.2020**

Philip von Platen, M.Sc. Supervisor's signature	doc. Ing. Tomáš Svoboda, Ph.D. Head of department's signature	prof. Ing. Pavel Ripka, CSc. Dean's signature

III. Assignment receipt

The student acknowledges that the master's thesis is an individual work. The student must produce his thesis without the assistance of others, with the exception of provided consultations. Within the master's thesis, the author must state the names of consultants and include a list of references.

.

Date of assignment receipt	Student's signature

Master Thesis

Daniel Klöser

Hierarchical Model Predictive Control for the Dynamical Power Split of a Fuel Cell Hybrid Vehicle

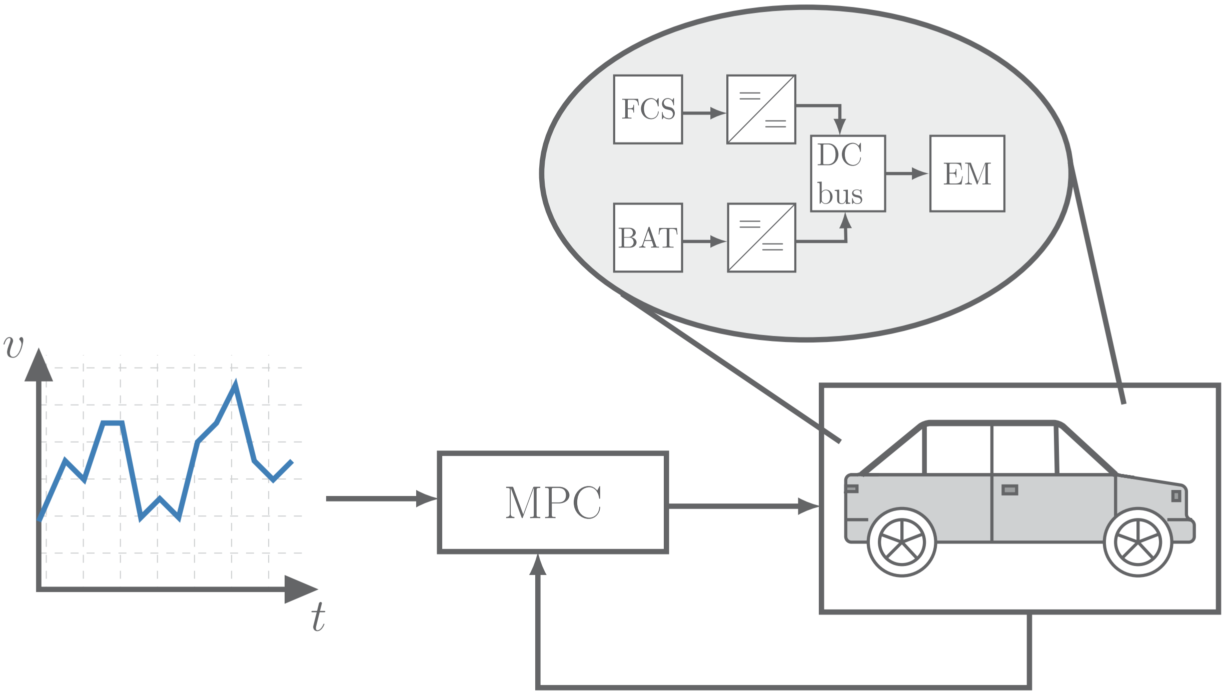

MEDICAL INFORMATION TECHNOLOGY & INSTITUTE OF AUTOMATIC CONTROL
Faculty of Electrical Engineering and Information Technology, RWTH Aachen
Univ.-Prof. Dr.-Ing. Dr. med. Steffen Leonhardt
Supervisor: Philip von Platen, M.Sc. & Verena Neisen, M.Sc.
Date: May 9, 2019

Acknowledgments

In the last 6 months, I was fortunate to be able to write my master thesis at the Institute of Automatic Control and Medical Information Technology. It was a great but also a very intense time. Therefore, I would like to give my gratitude to some people who accompanied me on my way.

I would first like to thank my supervisor at the Institute of Automatic Control M.Sc. Verena Neisen. The door was always open whenever I ran into a trouble spot or had a question about my research. She steered me in the right direction whenever I needed it.

Furthermore, I want to express my gratitude to my supervisor at the Medical Information Technology M.Sc. Philip von Platen who rendered this work possible. Especially during the tough periods, he supported me a lot and motivated me to keep going.

Moreover, a special gratitude goes to Univ.-Prof. Dr.-Ing. Dr. med. Steffen Leonhardt who gave me the possibility to write my thesis externally and enabled me to further strive for my passion of control theory.

I appreciate the great atmosphere which I experienced at the Institute of Automatic Control. Therefore, I would like to acknowledge Univ.-Prof. Dr.-Ing. Dirk Abel and all employees of the Institute of Automatic Control.

I also want to state my gratitude to the "Modellfabrik crew" B.Sc. Thuc Anh Nguyen, B.Sc. Andreas Klein and B.Sc. Marc Üdelhofen. It has been a great time and the conceiving talks we had were elementary for our all achievements.

In addition, I acknowledge all my friends for giving me hand in the intense moments. A special gratitude goes to B.Sc. Jasmin Suhr who gave my work the linguistic refinement.

Last but not least, I want to thank my parents, Christine Klöser and Dipl.-Ing. Bernd Klöser, and my sister B.A. Tanja Klöser, who supported me with all their strength during my entire educational path. I am so grateful for the possibilities you gave me!

Daniel Klöser,
Aachen,
May 9, 2019

Eidesstattliche Versicherung

Name, Vorname

Matrikelnummer (freiwillige Angabe)

Ich versichere hiermit an Eides Statt, dass ich die vorliegende Arbeit/Bachelorarbeit/ Masterarbeit* mit dem Titel

selbständig und ohne unzulässige fremde Hilfe erbracht habe. Ich habe keine anderen als die angegebenen Quellen und Hilfsmittel benutzt. Für den Fall, dass die Arbeit zusätzlich auf einem Datenträger eingereicht wird, erkläre ich, dass die schriftliche und die elektronische Form vollständig übereinstimmen. Die Arbeit hat in gleicher oder ähnlicher Form noch keiner Prüfungsbehörde vorgelegen.

Ort, Datum

Unterschrift

*Nichtzutreffendes bitte streichen

Belehrung:

§ 156 StGB: Falsche Versicherung an Eides Statt

Wer vor einer zur Abnahme einer Versicherung an Eides Statt zuständigen Behörde eine solche Versicherung falsch abgibt oder unter Berufung auf eine solche Versicherung falsch aussagt, wird mit Freiheitsstrafe bis zu drei Jahren oder mit Geldstrafe bestraft.

§ 161 StGB: Fahrlässiger Falscheid; fahrlässige falsche Versicherung an Eides Statt

(1) Wenn eine der in den §§ 154 bis 156 bezeichneten Handlungen aus Fahrlässigkeit begangen worden ist, so tritt Freiheitsstrafe bis zu einem Jahr oder Geldstrafe ein.

(2) Straflosigkeit tritt ein, wenn der Täter die falsche Angabe rechtzeitig berichtigt. Die Vorschriften des § 158 Abs. 2 und 3 gelten entsprechend.

Die vorstehende Belehrung habe ich zur Kenntnis genommen:

Ort, Datum

Unterschrift

Abstract

In order to reduce emissions of the transport sector, fuel cell hybrid vehicles (FCHVs) constitute a promising alternative as they have zero local emissions and overcome the limited range of electric vehicles. The power management of the propulsion system poses many challenges since it is a highly nonlinear, constrained, strongly coupled, multiple-input multiple-output (MIMO) system. The control objectives aim at dynamic power delivery, minimization of hydrogen consumption and charge sustainability of the battery. This thesis presents a hierarchical model predictive control (MPC) with three levels approaching the control problem on different time scales.

The high-level control (HLC) implemented as a nonlinear MPC optimizes the static power split between battery and fuel cell system. The intermediate-level control (ILC) uses static optimization to determine the optimal operating point of the air supply. The low-level control (LLC) is a nonlinear MPC and tracks the reference trajectories received from the higher levels.

The hierarchical MPC is evaluated on a detailed model of an FCHV using the worldwide harmonized light vehicles test cycle. Utilizing predictive information about the power demand, the HLC provides a power split that assures charge sustainability of the battery and only deviates by 0.2 % from the optimal solution in terms of hydrogen consumption. Due to the predictive behavior and inherent decoupling capability of an MPC, the LLC achieves dynamic power delivery while explicitly considering the system constraints caused by prevention of oxygen starvation and limited operating range of the compressor. Moreover, the actual hydrogen consumption deviates only by 1 % from the hydrogen consumption that is predicted by the HLC. Even for uncertain power demand prediction, the LLC attains dynamic power delivery by deviating from the reference trajectories to relieve the fuel cell system when operating under system constraints.

Kurzfassung

Um die Emissionen des Verkehrssektors zu reduzieren, stellen Brennstoffzellen-Hybridfahrzeuge (FCHVs) eine vielversprechende Alternative dar, da sie keine lokalen Emissionen aufweisen und die begrenzte Reichweite von Elektrofahrzeugen überwinden. Das Leistungsmanagement des Antriebssystems stellt viele Herausforderungen dar, da es sich um ein hochgradig nichtlineares, beschränktes, stark gekoppeltes MIMO System handelt. Die Regelungsziele sind eine dynamische Leistungsbereitstellung, die Minimierung des Wasserstoffverbrauchs und die Ladungserhaltung der Batterie. Diese Arbeit präsentiert eine hierarchische MPC mit drei Ebenen, die die Regelungsziele auf verschiedenen Zeitskalen behandelt.

Die als nichtlineare Modellprädiktive Regelung implementierte High-Level Regelung (HLC) optimiert die statische Leistungsverteilung zwischen der Batterie und dem Brennstoffzellensystem. Die Intermediate-Level Regelung (ILC) ermittelt mittels statischer Optimierung den optimalen Betriebspunkt der Luftzufuhr. Die Low-Level Regelung (LLC) ist eine nichtlineare MPC und folgt den von den höheren Ebenen empfangenen Referenztrajektorien.

Die hierarchische MPC wird an einem detaillierten Modell eines FCHVs unter Verwendung des WLTC Fahrzykluses ausgewertet. Unter Verwendung von prädiktiven Informationen über den Leistungsbedarf erreicht die HLC eine Leistungsverteilung, die die Ladungserhaltung der Batterie gewährleistet und nur um 0.2 % von der optimalen Lösung in Bezug auf den Wasserstoffverbrauch abweicht. Aufgrund des prädiktiven Verhaltens und der inhärenten Entkopplungsfähigkeit der MPC erreicht die LLC eine dynamische Leistungsabgabe unter expliziter Berücksichtigung der Systembeschränkungen, die durch die Vermeidung von Sauerstoffmangel und den begrenzten Betriebsbereich des Kompressors verursacht werden. Darüber hinaus weicht der tatsächliche Wasserstoffverbrauch nur um 1 % vom Wasserstoffverbrauch ab, der durch die HLC prädiziert wird. Selbst bei ungewissen Leistungsbedarfsvorhersagen erreicht die LLC eine dynamische Leistungsabgabe, indem sie von den Referenztrajektorien abweicht, um das Brennstoffzellensystem bei Betrieb unter Systemzwängen zu entlasten.

Table of Contents

List of Symbols

Acronyms

DMC	dynamic matrix control
DP	dynamic programming
ECMS	equivalent consumption minimization strategy
FCHV	fuel cell hybrid vehicle
FCS	fuel cell system
HJB	Hamilton-Jacobi-Bellmann
HLC	high-level control
ICE	internal combustion engine
ILC	intermediate-level control
LLC	low-level control
LQR	linear quadratic regulator
MIMO	multiple-input multiple-output
MPC	model predictive control
NEDC	new european driving cycle
NiMH	nickel metal hydride battery
NMPC	nonlinear model predictive control
OCP	optimal control problem
OCV	open circuit voltage
ODE	ordinary differential equation
PEM	proton-exchange membrane
PEMFC	proton-exchange membrane fuel cell
PMP	Pontryagin's minimum principle
RGA	relative gain array
RMSE	root mean square error
SC	supercapacitor
SISO	single-input single-output
SOC	state-of-charge
UNO	United Nations Organization
WLTC	worldwide harmonized light vehicles test cycle
WLTP	worldwide harmonized light vehicle test procedure

Physical Quantities

A	area	m^2
C_d	nozzle discharge coefficient	-

$c^{(1)}$	concentration	-
$c^{(2)}$	specific heat capacity	$\frac{\mathrm{J\,K}}{\mathrm{kW}}$
E	energy	kW h
E^{rev}	reversible voltage	V
I	current	A
J	inertia	$\mathrm{kg\,m^2}$
H	heating value	$\frac{\mathrm{J}}{\mathrm{mol}}$
h	valve opening position	-
h_{n}	relative frequency	-
k_{T}	motor torque constant	$\frac{\mathrm{N\,m}}{\mathrm{A}}$
k_{t}	temperature coefficient of reversible cell voltage	$\frac{\mathrm{N\,m}}{\mathrm{A}}$
M	molar mass	mol
m	mass	kg
$\dot{m}$	mass flow rate	$\frac{\mathrm{kg}}{\mathrm{s}}$
m_{H_2}	hydrogen consumption	g
$\dot{m}_{H_2}$	hydrogen consumption	$\frac{\mathrm{g}}{\mathrm{s}}$
N	rotational speed	rpm
$\dot{n}$	mole flow rate	$\frac{\mathrm{mol}}{\mathrm{s}}$
P	power	W
Q	battery storage capacity	A h
p	pressure	Pa
R	resistance	Ω
T	temperature	K
U	voltage	V
ΔU	voltage loss	V
V	volume	$\mathrm{m^3}$
X_{O_2}	mole fraction of oxygen	-

η	efficiency	-
γ	ratio of specific heats	-
λ_{O_2}	oxygen excess ratio	-
Π	pressure ratio	-
τ	torque	N m
ω	rotational speed	$\frac{\mathrm{rad}}{\mathrm{s}}$

Mathematical Quantities

$\mathbf{A}$	system matrix
$\mathbf{B}$	input matrix
$\mathbf{C}^{(1)}$	output matrix
$\mathbf{C}^{(2)}$	penalty matrix
c	penalty coefficients
$\mathbf{D}$	feed-forward matrix

$d^{(1)}$	measured disturbance
$d^{(2)}$	gradient direction
g	equality constraint
H	Hamiltonian
h	inequality constraint
J^c	optimal cost-to-go
J	cost
l	Lagrange term
N_C	control horizon
N_P	prediction horizon
$\mathbf{p}$	parameter vector
$\mathbf{Q}$	weighting matrix on states
$\mathbf{R}$	weighting matrix on inputs
$\mathbf{r}$	reference trajectory
$\mathbf{u}$	control input vector
$\mathbf{w}$	set point trajectory
$\mathbf{x}$	state vector
$\mathbf{y}$	system output vector
$\mathbf{z}$	disturbance vector

α	step size
ϵ	threshold
μ	Lagrange multiplier
$\lambda^{(1)}$	costate
$\lambda^{(2)}$	eigenvalue
ρ	robustness factor
Φ	Mayer term

Subscripts

0	initial value
bat	battery
bus	at DC bus
cp	compressor
cm	compressor motor
cat	cathode
del	delivered
dem	demanded
fc	elementary fuel cell
fcs	fuel cell system
im	inlet manifold
k	time step k
lhv	lower heating value

net	at output of component
om	outlet manifold
op	operating point
ref	reference
sca	scaled
st	fuel cell stack

Superscripts

h	high-level control
i	intermediate level control
l	low-level control
$*$	optimal value
$\sim$	augmented
$\cdot$	derivative with respect to time
$-$	average value

Constants

c_p	average specific heat capacity of air	$1.00\,\frac{\mathrm{kJ}}{\mathrm{kg\,K}}$
F	Faraday constant	$26.80\,\frac{\mathrm{A\,h}}{\mathrm{mol}}$
H_{H_2}	lower heating value of hydrogen	$241.83\,\frac{\mathrm{kJ}}{\mathrm{mol}}$
M_a	Molar mass of air	$28.96\,\frac{\mathrm{g}}{\mathrm{mol}}$
M_H	Molar mass of hydrogen	$1.01\,\frac{\mathrm{g}}{\mathrm{mol}}$
M_O	Molar mass of oxygen	$16.00\,\frac{\mathrm{g}}{\mathrm{mol}}$
p^0	nominal pressure	$101.33\,\mathrm{kPa}$
R_u	gas constant	$8.31\,\frac{\mathrm{J}}{\mathrm{K\,mol}}$
T^0	nominal temperature	$25\,^{\circ}\mathrm{C}$
γ	ratio of specific heats of air	1.40

List of Figures

List of Tables

1 Introduction

1.1 Motivation

As a result of global warming, 196 members of the United Nations Framework Convention on Climate Change (UNFCCC) signed the Paris Agreement in December 2015 [1]. The central goal is to strengthen the global response to approach the causes of climate change and keep the global temperature rise below 2 °C. In consequence of this agreement, the German government set the target to reduce the greenhouse gas emissions until 2020 by 40 % compared to 1990 [2].

In 2016, passenger traffic was responsible for 15 % of the overall greenhouse gas emissions in Germany [3]. Up to now, the automotive industry is dominated by combustion engines. However, recent public debates on the diesel emissions scandal led to a trend towards alternative concepts such as hybrid, electric and fuel cell hybrid vehicles. Hybrid and electric cars are currently paving their way to the mass market. Nevertheless, also fuel cell hybrid vehicles constitute a promising solution as they have zero local emissions and overcome the limited range and long charging time of electric cars [3].

Fuel cell hybrid vehicles are driven by an electric motor and are powered by a fuel cell system which generates electrical power from the electrochemical reaction of hydrogen and oxygen. The reactants need to be supplied by peripheral components. In automotive applications, pure hydrogen is supplied from high pressure tanks while the oxygen is delivered by ambient air utilizing a compressor. Thereby, the compressor motor can consume up to 20 % of the electrical power produced by the fuel cell stack [4]. Additionally, the air supply limits the response time of the power delivery. Thus, the air supply should be considered in the power management.

Besides the fuel cell system, a secondary power source is included leading to an additional degree of freedom in the power delivery. This can be utilized to reduce the hydrogen consumption by increasing the efficiency of both components. Knowing the whole driving cycle in advance, this additional degree of freedom can be used in a global optimal manner [5]. In practice, this approach is not applicable because the predictive information about the power demand is of limited accuracy. Consequently, adequate control methods for the power split are required.

The increase in computational power in recent years enables more sophisticated approaches for the control of fuel cell hybrid vehicles. Model predictive control (MPC) can optimize the manipulated variables with regard to user defined objectives based on an internal prediction model of the propulsion system. Additionally, MPCs are capable of explicitly considering input as well as state constraints of the system and of utilizing predictive information which is accomplished by iteratively solving an optimal control problem [6].

1.2 Thesis Goals

Central objectives to the power management of the FCHV include dynamic power delivery, hydrogen consumption minimization, charge sustainability of the battery and compliance with system constraints. In order to achieve these objectives, several challenges have to be resolved.

- The afore mentioned objectives have to be considered on different time scales. While the dynamic power delivery should be handled within milliseconds, charge sustainability and hydrogen consumption minimization take into account a few seconds or even minutes.

- The propulsion system of the FCHV is a strongly coupled, nonlinear MIMO system. The battery and the fuel cell system constitute two power delivery units. Moreover, the fuel cell system comprises several peripheral components such as a compressor, valves and pumps. Consequently, the resulting redundancy of the system should be utilized optimally in regard to the objectives.

- Furthermore, the power management has to comply with several system constraints in order to ensure safety and preserve the components. These include, e.g., power limitations of the battery and the fuel cell system, operating boundaries of the compressor and prevention of oxygen starvation.

- The power management must deal with uncertain power demand predictions that can arise due to unexpected events or unpredictable intentions of the driver.

The aim of this thesis is to design a hierarchical MPC that accomplishes the central objectives and resolves the related challenges. Therefore, the levels of the hierarchical MPC are defined based on the dominant time constants of the system. Furthermore, partial objectives get assigned to each control level and the nonlinear prediction model for each level is derived. Moreover, the corresponding optimal control problems is stated and solved with an appropriate method. Finally, the hierarchical control is validated on a detailed model of an FCHV.

1.3 Outline

Chapter 2 presents an overview of the fundamentals relevant for this thesis. Firstly, the chosen vehicle configuration is introduced. Subsequently, the fundamentals of MPC and optimal control are presented. Finally, a literature review is conducted summarizing current approaches for the power management of an FCHV.

In **Chapter 3**, the component models of the FCHV which are utilized for the prediction model of the MPC are presented. The model is derived with a gray box modeling technique.

In **Chapter 4**, the hierarchical control structure is introduced. Therefore, the control levels are established based on the dominant time constants of the system. Apart from that, the objectives of each level are summarized and the resulting optimal control problems are stated. Moreover, an appropriate solution method is chosen and implementation details are stated.

In **Chapter 5**, the hierarchical MPC is evaluated on a detailed model of an FCHV using the worldwide harmonized light vehicles test cycle (WLTC). Thereby, the individual control levels are validated with regards to the partial objectives. Moreover, the cooperation between the control levels is examined. Finally, the capabilities of handling uncertain power demand predictions are investigated.

Chapter 6 concludes the achievements of this thesis and presents an outlook for further investigations.

2 Fundamentals and State of the Art

In this chapter, the fundamentals and state of the art relevant for this thesis are presented. In Section 2.1, the components of a fuel cell hybrid vehicle are introduced. The control methods for the high-level control (HLC) and the low-level control (LLC) are based on nonlinear optimal control which is presented in Section 2.2 including the fundamental idea as well as solution methods. Additionally, the linkage to model predictive control (MPC) is explained. Finally, in Section 2.3, current energy management strategies in fuel cell hybrid vehicles are presented.

2.1 Fuel Cell Hybrid Vehicle

This section provides basic information about the setup of a fuel cell hybrid vehicle (FCHV). The vehicle model used in this thesis is based on the work of Dirkes [7]. In Section 2.1.1, an overview of different possible topologies of an FCHV is provided. Additionally, the configurations chosen for this thesis are specified. Basic explanations of the fuel cell electrochemistry are given in Section 2.1.2. In Section 2.1.3, the peripheral components which are required for a safe and dynamic operation are presented. Finally, in Section 2.1.4, battery fundamentals are presented.

2.1.1 Vehicle Setup

The first FCHV was developed by General Motors in 1967 but for reasons of safety it was never publicly available [8]. It was powered only by the fuel cell itself without any additional power source, which has many disadvantages. Nowadays, there are around a dozen FCHVs, either publicly available or still under development, such as Mercedes-Benz-F-Cell (GER,2018), Toyota Mirai (JPN, 2016), Hyundai Nexo (KOR, 2018), FEV Fiat 500 Breeze (GER,2017) and others. All of these cars come with additional power sources (e.g. battery or supercapacitor (SC)) due to the following advantages:

- **Efficient operation**: The fuel cell system (FCS) has its highest efficiency at part load. The additional power source can be used to shift the operating point of the FCS into higher efficiencies.

- **Regenerative braking**: The battery can be utilized to store energy from regenerative braking with high efficiency.

- **Dynamic behavior**: The dynamics of the fuel cell system are limited by the air supply due to the inertia of the compressor [3]. The additional power source can be utilized to increase the dynamic response to power demand changes [9].

- **Start-up support**: The fuel cell system cannot run at full load during start-up phase, especially at freezing temperature. The battery can be used to supports the fuel cell system until its warmed up [3].
- **Cost scaling**: The cost of an additional power source roughly scales with the capacity, while the cost of the FCS scales with the peak power. Therefore, a combination of both can optimize the overall cost by reducing the peak power of the FCS and the capacity of the battery [10].
- **Low integration complexity**: Since the FCHV is powered by an electric motor, an additional electrical power source can be coupled with the FCS electrically. This is simpler than coupling the systems mechanically by gearing mechanisms as it is often done for internal combustion engine (ICE) hybridization [11].

The optimal choice of the additional power sources and its sizing depend on the specifications of the vehicle and requirements for the performance. This topic is not investigated in this thesis but investigations by *Yi et al* [12], *Hu et al.* [13] and *Jain et al.* [14] are recommended for the interested reader.

There exist different classifications for FCHVs. Firstly, the FCHV can be classified into two categories according to the sizing of the FCS compared to the additional power source [8]:

- **Full-hybrid FCHV**: The FCS is the main power source and the electrical energy storage system is mainly used for regenerative braking, shifting the FCS to more efficient operating points and increasing the dynamic response to load changes (e.g. Mercedes-Benz GLC F-CELL, Honda FCX Clarity, Toyota Mirai).
- **Fuel cell range extender**: The main power source is the electrical energy storage system and the FCS extends the vehicle range, thereby tackling one of the major disadvantages of fully electric vehicles (e.g. FEV Fiat 500 Breeze).

Secondly, the FCHV can be classified according to the type of refueling of the electrical energy storage system [8]:

- **Plug-in hybrid**: It can be charged by the electric grid. In this case, the additional power source is a large battery. It can be used to cover short distances without the FCS. This type often corresponds to a fuel cell range extender (e.g. FEV Fiat 500 Breeze, Mercedes-Benz GLC F-CELL).
- **Hydrogen station refueling**: In this case the battery cannot be charged externally. This means that all the electricity stored in the additional power source either comes from regenerative braking or from the FCS (e.g. Honda FCX Clarity, Toyota Mirai).

The chosen system in this thesis is a full hybrid FCHV with gas station refueling. In Figure 2.1, the component configuration is presented. The battery and the FCS are connected in parallel through a DC bus. Two DC/DC converters are used to maintain a constant voltage level at the bus. The electric motor (EM) is connected to the bus via a DC/AC converter and connected to the wheels via a differential gear. Marked in red are the electrical power values that are utilized throughout the thesis. $P_{\text{fcs,net}}$ and $P_{\text{bat,net}}$ are the fuel cell system and battery power at the output of the components while $P_{\text{fcs,bus}}$ and $P_{\text{bat,bus}}$ are the power values at the DC bus. P_{del} is the delivered to the motor. Marked in green is the point of the power split between the battery and FCS. At this point the demanded power P_{dem} which is the reference value of the delivered power is calculated based on the speed profile of the driving cycle. Three modes of operation can be distinguished [7]:

1. **Parallel powering** (solid arrows): The FCS and the battery are used in parallel for powering the motor.

2. **Charging** (dotted arrows): The FCS powers the motor and charges the battery simultaneously.

3. **Recuperation** (striped arrows): The battery is charged by regenerative braking.

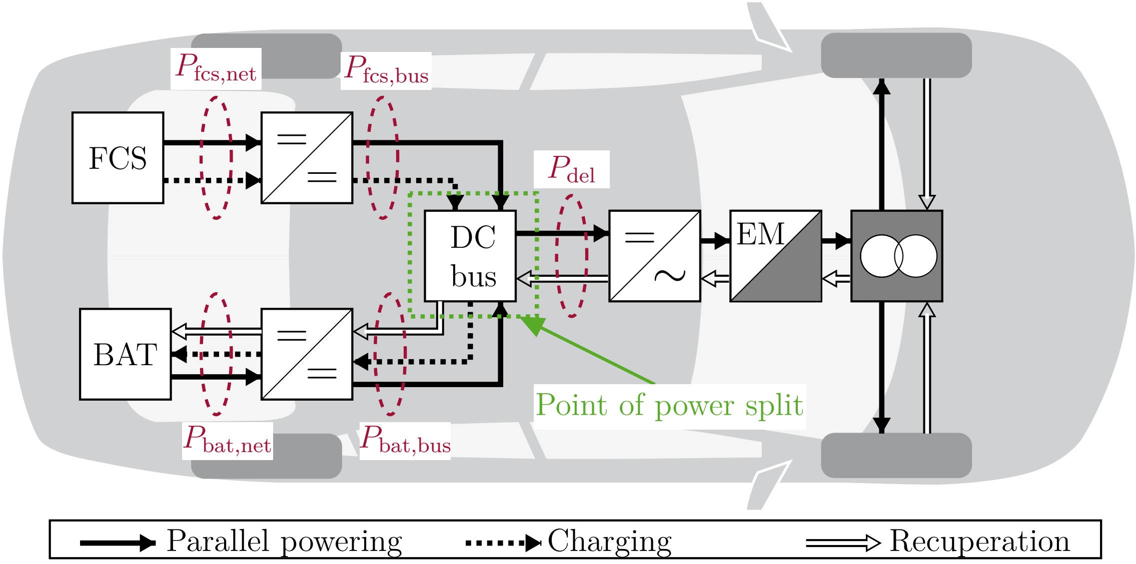

Fig. 2.1: Configuration of the fuel cell hybrid vehicle [7].

The battery, which is the only additional power source, has a capacity of 6.5 Ah and the maximum power of the FCS is 50 kW. This corresponds to the specifications needed for a medium-sized car. Other vehicle parameters required to compute the power demand P_{dem} are based on the specifications of the Toyota Mirai and can be found in Table A.1. Electric motor and differential gear are modeled by constant efficiencies η_{mot} and η_{gear} as they have no influence on the power split between the battery and FCS at the DC bus.

2.1.2 Fuel Cell Basics

In recent years, several types of fuel cells have been developed. In general, they are categorized by the type of electrolyte that is used for the membrane. Besides that, there are other differences such as the operating temperature, fuel and pressure. In automotive applications, the proton-exchange membrane fuel cell (PEMFC) has been established. It was first developed by General Electric in the 1960s for space applications carried out by the NASA [4]. The PEMFC has several advantages compared to other technologies [15, p.78] [4, p.67]. The membrane is very thin and can therefore be stacked compactly. The operating temperature is low which reduces the start-up time. Furthermore, the cell can work in any orientation and has a good dynamic response. Disadvantages are the purity of the hydrogen that is needed and the involved water management because the membrane needs to be properly humidified. Apart from that, the catalyst requires a large amount of platinum. Even though this amount was reduced by several orders in recent years, it is still a major cost factor of the FCS [3, 4, 16].

Subsequently, the basic principle of a PEMFC is explained based on *O'Hayre et al.* [17, Chapter 1-5] and *Larminie et al.* [4, Chapter 1-3]. The fuel cell is a galvanic cell, which converts chemical energy to electrical energy. There are always two reactions taking place: one at the anode and one at the cathode. A simple anode-electrolyte-cathode structure of a fuel cell is illustrated in Figure 2.2. The anode refers to the electrode where oxidation is taking place (electrons are liberated) and the cathode to the electrode where reduction is taking place (electrons are consumed). The proton-exchange membrane (PEM) only allows the charge carriers (H^+-ions) to pass from the anode to the cathode.

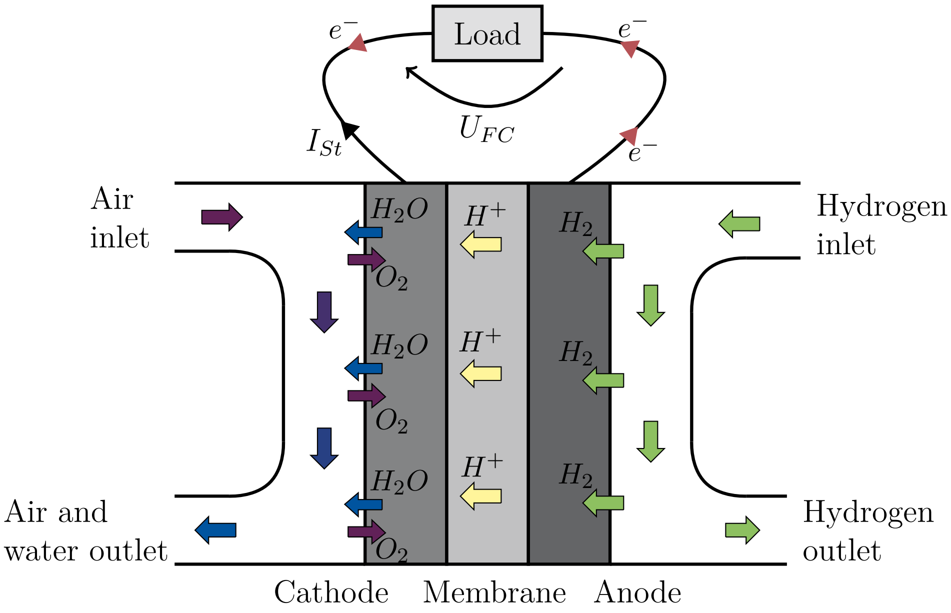

Fig. 2.2: Schematics of an elementary fuel cell.

The process of producing electricity in a fuel cell can be divided into four steps:

1. **Reactant supply**: Oxygen (reductant) is supplied to the cathode and hydrogen (oxidant) to the anode. In automotive applications, pure hydrogen is supplied from high pressure tanks while oxygen is supplied in form of ambient air to the cathode. Besides 21 % of oxygen, ambient air also consists of 79 % nitrogen which lowers the efficiency of the FCS and makes the system prone to oxygen starvation [4]. This occurs when not enough reactants are supplied to the electrode, resulting in severe damage of the membrane.

2. **Electrochemical reaction**: At the anode, an oxidation following Equation 2.1 is taking place. The electrons are liberated from the H_2 molecules. At the cathode a reduction following Equation 2.2 is taking place. Here, the electrons are consumed by the H^+-ions that pass through the membrane.

$$2H_2 \rightarrow 4H^+ + 4e^- \qquad \text{(Anode)} \tag{2.1}$$

$$O_2 + 4H^+ + 4e^- \rightarrow 2H_2O \qquad \text{(Cathode)} \tag{2.2}$$

3. **Ionic and electronic conduction**: Caused by the electrochemical potential of the redox reaction, the electrons and charge carriers pass from the anode to the cathode. H^+-ions can diffuse through the membrane while electrons need to propagate through the wire leading to an electric current I_{St}.

4. **Product removal**: At the cathode, water is produced which needs to be removed in order to prevent the fuel cell from "flooding" which means that water is condensing inside the fuel cell. This leads to severe damage of the membrane. The removal of water is achieved by evaporation. Additionally, a small fraction of water and nitrogen drifts back through the membrane to the anode. Therefore, the anode needs to be purged in regular intervals meaning that the hydrogen outlet is opened to remove byproducts.

2.1.3 Peripherals of a Fuel Cell System

In order to preserve the fuel cell, it must be operated under certain conditions in terms of humidity and reactant supply. Therefore, the fuel cell needs peripheral components. In Figure 2.3, an overview of the peripherals is given. They can be categorized into three subsystems (heat transfer in red, air supply in blue and hydrogen supply in green), which are explained in the following subsections. The explanations are based on *Larminie et al.* [4, Chapter 4] and *Pukrushpan et al.* [9, Chapter 2].

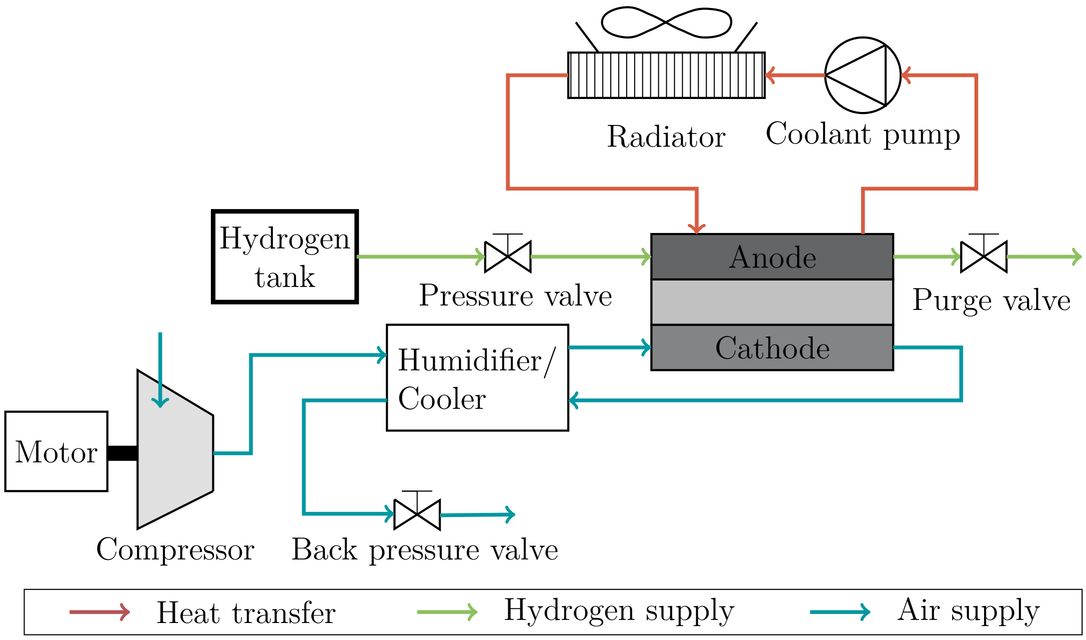

Fig. 2.3: Overview of peripherals installed in a fuel cell system with dead-end anode [4].

Heat transfer

The PEMFC is operated at about 80 °C. Since the electrochemical process is not reversible and some of the energy is lost to heat, the fuel cell stack needs to be cooled. In automotive applications, where a high power density is demanded, water cooling is utilized. The hot water coming from the fuel cell, gets pumped through a radiator and exchanges the heat with the ambient air. Because the temperature difference between the FCS and the ambient air is small, a large radiator needs to be utilized.

Hydrogen supply

The hydrogen is stored in a high pressure gas tank at 700 bars and supplied via the pressure valve. The pressure in the anode is between 1.5 bar to 3 bar during operation. The fuel cell, which is used in the chosen system, has a dead-end anode, which means that the pressure is not regulated by an outlet valve or reused by a circulation pump. The main pressure reduction is caused by the oxidation of the hydrogen at the membrane. Nevertheless, the anode has an outlet valve for purging.

Air supply

The air supply is critical for the operation of the fuel cell as it limits the dynamics of the power delivery. From the electrochemical point of view, the power can be delivered nearly instantaneously because the electrochemical dynamics are of order $\mathcal{O}(10^{-19}\,\mathrm{s})$. However, the dynamics of the power delivery are coupled to the dynamics of the air supply which are of order $\mathcal{O}(10^{-1}\,\mathrm{s})$ due to the prevention of oxygen starvation. In order to quantify the oxygen supply, the oxygen excess ratio λ_{O_2} is introduced [9].

$$\lambda_{O_2} = \frac{\dot{n}_{\mathrm{cat,in}}}{\dot{n}_{\mathrm{react}}(I_{\mathrm{St}})} \tag{2.3}$$

$\dot{n}_{\mathrm{in}}$ is the oxygen molar flow rate into the cathode and $\dot{n}_{\mathrm{react}}$ is the oxygen molar flow rate reacting at the cathode. The amount is proportional to the stack current I_{St}. The oxygen excess ratio should not fall below 1.5 and therefore limits the dynamics of the stack current I_{St} [18].

As presented in Figure 2.3, the components which regulate the air supply of the system are the compressor and the back pressure valve. The operation of the compressor has a significant influence on the overall system efficiency because the power consumption of the compressor has to be subtracted from the power production of the FCS. The compressor can use up to 20 % of the produced power and therefore has a direct influence on the overall system efficiency [4]. There are four types of compressors suitable for fuel cell applications [4, Chapter 9]:

1. **Roots compressor**: The roots compressor is cheap to produce and works over a wide range of air mass flow rates. However, it only works with high efficiency at low pressure rate.

2. **Lysholm or screw compressor**: The compressor has a wide range of compression ratios and operates with good efficiencies over a wide range of flow rates. However, they are expensive to manufacture, since they require precision work.

3. **Centrifugal or radial compressor**: This type is of low cost and can cover a wide range of flow rates. The efficiency of the compressor is good but it has to be operated within a well-defined ratio of air mass flow rate and pressure.

4. **Axial flow compressor**: The axial flow compressor has good efficiency but is expensive to produce and can only cover a narrow range of air mass flow rates.

The chosen system utilizes the centrifugal compressor, which is the standard for portable fuel cells between 10 kW and 100 kW [4]. The compressor flow map is illustrated in Figure 2.4. The pressure ratio Π which is defined by (2.4) is depicted on the y-axis. $p_{\mathrm{cp,in}}$ is the pressure of the inlet air to the compressor and $p_{\mathrm{cp,out}}$ is the outlet pressure of the

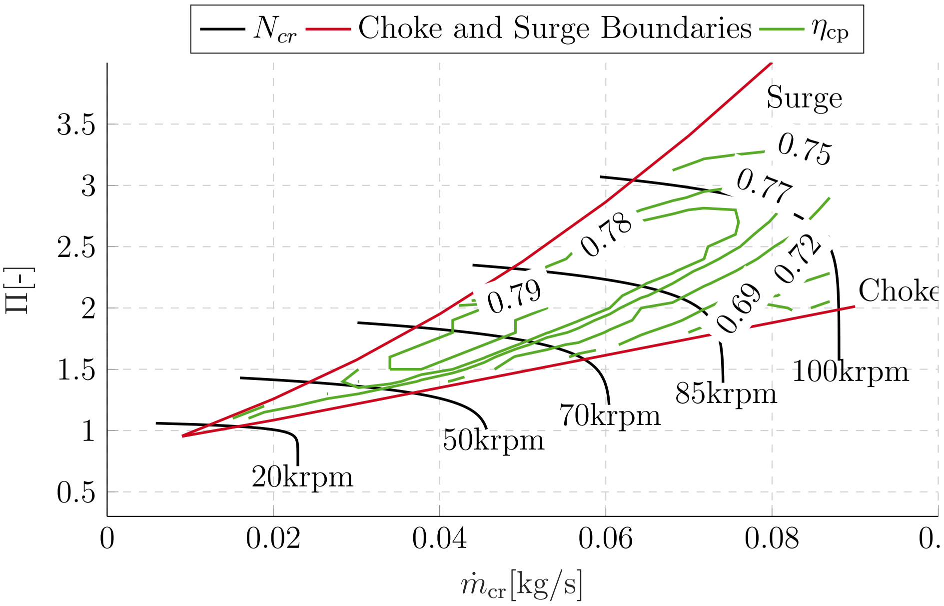

Fig. 2.4: Compressor map including efficiency [9].

compressor.

$$\Pi = \frac{p_{\mathrm{cp,out}}}{p_{\mathrm{cp,in}}} \tag{2.4}$$

The corrected air mass flow rate $\dot{m}_{\mathrm{cr}}$ in (2.5) is depicted on the x-axis. It depends on the temperature of the inlet air $T_{\mathrm{cp,in}}$, the air mass flow rate out of the compressor $\dot{m}_{\mathrm{cp}}$ as well as the ambient pressure $p_{\mathrm{cp,in}}$.

$$\dot{m}_{\mathrm{cr}} = \frac{\dot{m}_{\mathrm{cp}} \cdot \sqrt{T_{\mathrm{cp,in}}}}{p_{\mathrm{cp,in}}} \tag{2.5}$$

The black lines represent the equipotential lines of a constant rotational speed factor N_{cr} which is defined by (2.6). It depends on the rotational shaft speed N_{cp} and the temperature of the inlet air $T_{\mathrm{cp,in}}$. The rotational speed factor varies from 20 krpm to 100 krpm.

$$N_{\mathrm{cr}} = N_{\mathrm{cp}} \sqrt{\frac{288\,\mathrm{K}}{T_{\mathrm{cp,in}}}} \tag{2.6}$$

The green equipotential lines represent the points of constant compressor efficiency $\eta_{\mathrm{cp}}(\Pi, \dot{m}_{\mathrm{cr}})$ which is the ratio between the work that would have been needed for an isentropic (ideal) process and the actual work. These values are determined experimentally and are often given by lookup tables. The red lines represent the choke and surge boundaries. At the choke boundary, a high air mass flow rate $\dot{m}_{\mathrm{cr}}$ is present at low pressure ratio Π. In this case, the Mach number gets close to one and the inlet gas reaches sonic velocity. Therefore, the air mass flow rate $\dot{m}_{\mathrm{cr}}$ cannot be further increased. At the surge boundary, a low air mass flow rate$\dot{m}_{\mathrm{cr}}$ is present at high pressure ratio Π. On the left side of the boundary, the compressor has no gas to 'work on' and the upstream of the compressor flows back and gets pumped again. This leads to an unstable behavior and should thus be avoided. Consequently, the pressure ratio Π cannot be kept constant if a wide range of air mass flow rates $\dot{m}_{\mathrm{cr}}$ and good efficiencies η_{cp} are to be achieved.

There are two other components for the air supply shown in Figure 2.3, namely the cooler and the humidifier. Besides increasing the pressure $p_{\mathrm{cp,out}}$, the compressor also increases the air temperature $T_{\mathrm{cp,out}}$. In order to preserve membrane, a cooler is added. It cools down the air of the compressor to the stack temperature T_{St}. The other component is the humidifier, which has a significant influence on the lifetime of the PEMFC. The relative humidity of the air should stay above 80 % to prevent excess drying and below 100 % to prevent "flooding" of the membrane. For fuel cells with operating temperature above 60 °C, external humidification is inevitable. There are different methods to humidify air. Yet, there is no standard that has been established. A common method that is used for fuel cells in the power range of 10 kW to 100 kW is the water injection as a spray. A promising approach which has recently been investigated are self-humidifying membranes. Nevertheless, they are not yet applicable for high power fuel cells [4].

2.1.4 Battery Basics

Just like the fuel cell, the battery is a galvanic cell. It converts chemical energy to electrical energy. However, there is a fundamental difference. While the fuel cell has to be constantly supplied with the reactants oxygen and hydrogen, the battery is an energy storage system. When the battery is fully charged, all charge carriers are stored at the anode and when the battery is discharging, the charge carriers move to the cathode. Note that the names anode and cathode refer to the discharging process. When the battery is charged, oxidation and reduction switch sides. However, in many literature sources, the electrodes are still called anode and cathode as for the discharging process [19]. As soon as reactants are fully consumed at the anode or the cathode, the battery is completely discharged.

There are many types of batteries, which differ in the materials used for the electrodes and the membrane. Common types of batteries in automotive applications are Lithium-Ion (Li-Ion) and Nickel Metal Hydride (NiMH) batteries. Both batteries have a similar storage capacity but Li-Ion batteries can charge and discharge more rapidly than NiMH batteries. They also do not suffer as much from the "memory effect" which occurs when the battery is recharged before it is fully empty leading to a lower storage capacity. NiMH batteries are less sensible to extreme environmental influences such as hot temperature and are less costly [20]. The Toyota Mirai utilizes a NiMH battery with a capacity of 6.5 Ah.

2.2 Nonlinear Optimal Control

In this section, an optimal control problem is introduced and the common solution methods are presented. In Section 2.2.1, the most general optimal control problem that is required for the control of the FCHV is explained. In Section 2.2.2, general methods to solve this problem are presented. The approach utilized for the low-level control (LLC) is the augmented Lagrangian which is an indirect method. It is presented in more detail in Section 2.2.3 including implementation specific information about the toolbox GRAMPC [21]. Finally, in Section 2.2.4, the concept of Model Predictive Control, which solves the optimal control problem in an iterative manner, is explained.

2.2.1 Optimal Control Problem Formulation

The continuous time optimal control problem is presented in (2.7) [22]. It is the most general form that is required for the purpose of this thesis. The cost function in (2.7a) is composed of the terminal cost Φ (also called Mayer term) and the integral cost l (also called Lagrange term). The constraints are given by the ordinary differential equation (ODE) in (2.7b), the initial state conditions in (2.7c), inequality constraints in (2.7d) and equality constraints in (2.7e). In (2.7f), box constraints on the input vector are stated that can be treated differently than inequality constraints. The goal is to minimize the cost function with respect to the input trajectory $\mathbf{u}(t)$ meeting all constraints. In continuous time, this is an infinite dimensional problem which is in most cases not analytically solvable.

$$\begin{aligned}
\min_{\mathbf{u}} \quad & J = \Phi(\mathbf{x}(T)) + \int_{t_0}^{T} l(\mathbf{x}(t), \mathbf{u}(t))dt && (2.7a)\\
s.t. \quad & \dot{\mathbf{x}}(t) = \mathbf{f}(\mathbf{x}(t), \mathbf{u}(t)) && (2.7b)\\
& \mathbf{x}(t_0) = \mathbf{x}_0 && (2.7c)\\
& \mathbf{h}(\mathbf{x}(t), \mathbf{u}(t)) \leq 0 && (2.7d)\\
& \mathbf{g}(\mathbf{x}(t), \mathbf{u}(t)) = 0 && (2.7e)\\
& \mathbf{u} \in \begin{bmatrix} \mathbf{u}_{\min} & \mathbf{u}_{\max} \end{bmatrix} && (2.7f)
\end{aligned}$$

The problem can be nonlinear and non-convex. Convex optimization problems consist of a convex objective function J and a convex set of feasible solutions. In this case, every local minimum is also the global minimum. This property is desirable because the search for a local optimum is computationally cheaper than finding the global optimal solution of a non-convex function [22]. However, the optimal control problems stated in this thesis are not necessarily convex. Nevertheless, methods to find the local optimum are applied assuming that they can find the global or at least a sufficiently good local optimum.

2.2.2 Solution Methods for Nonlinear Optimal Control Problems

In Figure 2.5, an overview of solution methods for optimal control problems is given. Three different families of solution methods exist.

- Dynamic programming (DP) was originally invented for discrete time and state problems by Richard Bellmann and is extensively used in game theory. However, to some extent, it can also be used for continuous time optimal control utilizing the partial differential Hamilton-Jacobi-Bellmann (HJB) equation. Compared to the other methods, DP has the major advantage that it is capable of finding the global optimum in non-convex optimization problems. On the other hand, DP has large computational costs for high dimensional problems suffering from the so called "curse of dimensionality" [23].

- The indirect methods follow the principle of "first optimize, then discretize" which means that the optimal control problem is firstly solved subsequently discretized. Indirect methods utilize necessary conditions for optimality derived from the HJB equation for the solution. These conditions are called Pontryagin's minimum principle (PMP). One the one hand, indirect methods are only capable of finding a local optimal solution but they do not suffer from the curse of dimensionality on the other hand[22].

- The direct methods follow the principle of "first discretize, then optimize". In this case, the continuous time optimal control problem is first discretized resulting in a finite dimensional nonlinear program. It is widely used in academical and industrial applications because advanced solvers for the nonlinear program are available. As for the indirect methods, it is not capable of finding the global optimum but it also does not suffer from computational costs for high dimensional problems [22].

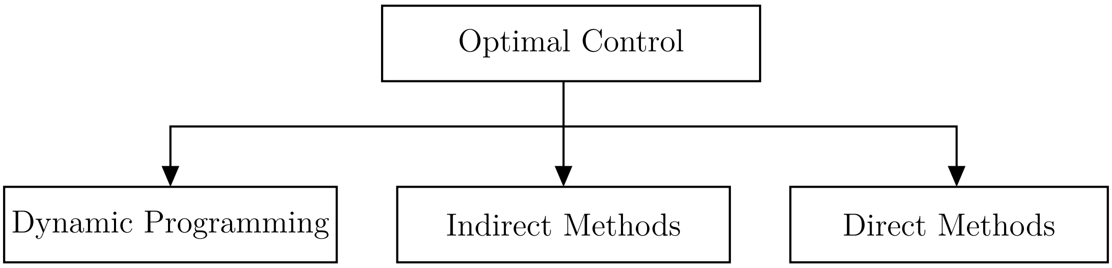

Fig. 2.5: Overview of solution methods for an optimal control problem [22].

In the following, an introduction to the three methods is given. For the low-level control, the indirect method is used and is consequently the focus of this section. Nevertheless, it is helpful to understand the concept of DP in order to derive the PMP conditions. Moreover, the concept of direct methods is introduced because it is utilized for the high-level control. If not other stated, the upcoming derivations are adapted from *Bertsekas* [23], *Rawlings et al.* [6], and *Diehl et al.* [22]. For reasons of conciseness, the time dependency of the states $\mathbf{x}(t)$ and the inputs $\mathbf{u}(t)$ is not explicitly stated in this section.

Dynamic Programming

A fundamental principle in optimal control is the principle of optimality. It was first stated by Richard Bellmann in 1957.

Principle of optimality. *An optimal policy has the property that whatever the initial state and initial decisions are, the remaining decisions must constitute an optimal policy with regards to the state resulting from the first decision. [24]*

The principle is illustrated in Figure 2.6. If the input trajectory $\mathbf{u}^*$ and state trajectory $\mathbf{x}^*$ from time t_0 to T describe the optimal trajectory, any subarc starting at any time $\bar{t}$ between t_0 and T on the optimal trajectory also describe the optimal trajectory. This seems a trivial statement but it gives the fundamental idea of DP and the indirect methods.

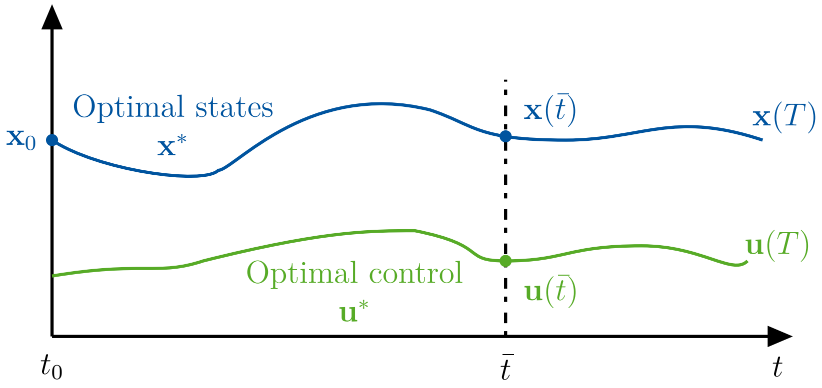

Fig. 2.6: Illustration of the principle of optimality [22].

In discrete DP, the principle of optimality is utilized to divide the problem into subproblems that are successively solved. The advantage that comes with the principle of optimality is that not all possible states have to be evaluated but only the ones that can still possibly be on the optimal trajectory. Thus, dynamic programming is an intelligent way to enumerate all possible trajectories.

The principle of optimality is mathematically introduced in terms of the optimal cost-to-go $J^c(\mathbf{x}, t)$. Referring to Figure 2.6, it represents the minimum cost from any intermediate state $\mathbf{x}(\bar{t})$ to the final state $\mathbf{x}(T)$.

In continuous dynamic programming, the optimal control problem can be solved by the partial differential HJB equation. The evolution of the optimal cost-to-go $\frac{dJ^c}{dt}$ can be calculated by backward integrating from the finale state cost Φ in (2.8a). For this purpose, the Hamilton-Jacobi-Bellmann (HJB) equation in (2.8b) has to be solved at any point of time. The interested reader can find the derivation of the HJB equation in [23, Chapter 3].

Knowing the evolution of the optimal cost-to-go $\frac{dJ^c}{dt}$, the optimal input trajectory $\mathbf{u}^*$ can be calculated by the forward integration of (2.8c).

$$\begin{aligned} J^c(\mathbf{x}, T) &= \Phi(\mathbf{x}(T)) && (2.8a)\\ -\frac{dJ^c}{dt}(\mathbf{x}, t) &= \min_{\mathbf{u}} \left[l(\mathbf{x}, \mathbf{u}) + \nabla_x J^c(\mathbf{x}, t)^T \mathbf{f}(\mathbf{x}, \mathbf{u})\right] && (2.8b)\\ \mathbf{u}^*(\mathbf{x}, t) &= \arg\min_{\mathbf{u}} l(\mathbf{x}, \mathbf{u}) + \nabla_x J^c(\mathbf{x}, t)^T \mathbf{f}(\mathbf{x}, \mathbf{u}) && (2.8c) \end{aligned}$$

The HJB equation is in general not analytically solvable and needs to be solved numerically. The numerical solution, however, suffers from the "curse of dimensionality". It means that the computational cost increases exponentially with the number of states. Consequently, it is only suitable for small dimensional problems. Nevertheless, it provides the fundamentals for the indirect methods, which utilize the HJB equation and derive necessary conditions of optimality.

Indirect Methods

The indirect methods became popular with the studies of Lev Pontryagin leading to the PMP in 1961 [22]. One ought to observe that the HJB equation in (2.8) does not depend on the optimal cost-to-go J^c but only on $\nabla_x J^c$. Therefore, the costate $\boldsymbol{\lambda}$ is introduced.

$$\boldsymbol{\lambda} = \nabla_x J^c(\mathbf{x}, t) \tag{2.9}$$

This leads to the definition of the Hamiltonian equation.

$$H(\mathbf{x}, \boldsymbol{\lambda}, \mathbf{u}) = l(\mathbf{x}, \mathbf{u}) + \boldsymbol{\lambda}^\top f(\mathbf{x}, \mathbf{u}) \tag{2.10}$$

The Hamiltonian can be substituted into the HJB equations in (2.8).

$$\begin{aligned} J^c(\mathbf{x}, T) &= \Phi(\mathbf{x}(T)) && (2.11a)\\ -\frac{\partial J^c}{\partial t}(\mathbf{x}, t) &= \min_{\mathbf{u}} H(\mathbf{x}, \nabla_x J^c(\mathbf{x}, t), \mathbf{u}) = H(\mathbf{x}^*, \boldsymbol{\lambda}^*, \mathbf{u}^*) && (2.11b)\\ \mathbf{u}^* &= \arg\ \min_{\mathbf{u}} H(\mathbf{x}^*, \boldsymbol{\lambda}^*, \mathbf{u}) && (2.11c) \end{aligned}$$

The goal in the following is to find an explicit formulation for the derivative of the optimal costate $\dot{\boldsymbol{\lambda}}^*$. It is assumed that the optimal trajectory $(\mathbf{x}^*, \boldsymbol{\lambda}^*, \mathbf{u}^*)$ is minimizing the HJB equation. Subsequently, (2.11b) is totally derived with respect to $\mathbf{x}$. Therefore, the chain rule is applied while it is assumed that $\frac{\partial H}{\partial u}$ is 0 on the optimal trajectory due to the first-order necessary condition of optimality [23].

$$\begin{aligned} -\frac{\partial^2 J^{\mathrm{c}}}{\partial \mathbf{x} \partial t}(\mathbf{x}^*, t) &= \frac{dH(\mathbf{x}^*, \boldsymbol{\lambda}^*, \mathbf{u}^*)}{d\mathbf{x}} \\ &= \frac{\partial H(\mathbf{x}^*, \boldsymbol{\lambda}^*, \mathbf{u}^*)}{\partial \mathbf{x}} \frac{\partial \mathbf{x}}{\partial \mathbf{x}} + \underbrace{\frac{\partial H(\mathbf{x}^*, \boldsymbol{\lambda}^*, \mathbf{u}^*)}{\partial \boldsymbol{\lambda}}}_{\mathbf{f}(\mathbf{x}^*, \mathbf{u}^*) = \dot{\mathbf{x}}^*} \underbrace{\frac{\partial \boldsymbol{\lambda}}{\partial \mathbf{x}}}_{\nabla_x^2 J^{\mathrm{c}}(\mathbf{x}^*, t)} + \underbrace{\frac{\partial H(\mathbf{x}^*, \boldsymbol{\lambda}^*, \mathbf{u}^*)}{\partial \mathbf{u}}}_{\mathbf{0}} \frac{\partial \mathbf{u}}{\partial \mathbf{x}} \end{aligned} \tag{2.12}$$

Replacing the partial derivatives by gradients leads to

$$-\frac{\partial}{\partial t} \nabla_x J^{\mathrm{c}}(\mathbf{x}^*, t) = \nabla_x H(\mathbf{x}^*, \boldsymbol{\lambda}^*, \mathbf{u}^*) + \nabla_x^2 J^{\mathrm{c}}(\mathbf{x}^*, t) \dot{\mathbf{x}}^*. \tag{2.13}$$

Rearranging this equation results in a condition for the derivative of the optimal costate $\dot{\boldsymbol{\lambda}}^*$.

$$\frac{\partial}{\partial t} \nabla_x J^{\mathrm{c}}(\mathbf{x}^*, t) + \nabla_x^2 J^{\mathrm{c}}(\mathbf{x}^*, t) \dot{\mathbf{x}}^* = \frac{d}{dt} \nabla_x J^{\mathrm{c}}(\mathbf{x}^*, t) = \dot{\boldsymbol{\lambda}}^* = -\nabla_x H(\mathbf{x}^*, \boldsymbol{\lambda}^*, \mathbf{u}^*) \tag{2.14}$$

At this point, it is worth summarizing all conditions that need to be satisfied by the optimal trajectory $(\mathbf{x}^*, \boldsymbol{\lambda}^*, \mathbf{u}^*)$.

$$\begin{aligned} \mathbf{x}^*(t_0) &= \mathbf{x}_0, && && \text{(initial value)} && \text{(2.15a)} \\ \dot{\mathbf{x}}^*(t) &= \mathbf{f}(\mathbf{x}^*(t), \mathbf{u}^*(t)), && t \in [0, T], && \text{(ODE model)} && \text{(2.15b)} \\ \dot{\boldsymbol{\lambda}}^*(t) &= -\nabla_x H(\mathbf{x}^*(t), \boldsymbol{\lambda}^*(t), \mathbf{u}^*(t)), && t \in [0, T], && \text{(adjoint equations)} && \text{(2.15c)} \\ \mathbf{u}^*(t) &= \arg\min_{\mathbf{u}} H(\mathbf{x}^*(t), \boldsymbol{\lambda}^*(t), \mathbf{u}(t)), && t \in [0, T], && \text{(minimum principle)} && \text{(2.15d)} \\ \boldsymbol{\lambda}^*(T) &= \nabla_x J^{c}(\mathbf{x}, T) = \nabla_x \Phi(\mathbf{x}^*(T)) && && \text{(adjoint final value)} && \text{(2.15e)} \end{aligned}$$

The conditions in (2.15) relate to the PMP conditions and give the necessary conditions for the optimal control problem. They can either be utilized to check if a trajectory is optimal or more interestingly to find a local optimal solution with numerical optimization. Because the conditions are necessary but not sufficient, the trajectory fulfilling the PMP might not be the global optimum. When the problem formulation as given in (2.7) is convex, the PMP conditions also provide a sufficient condition. Note that the result can be interpreted as an ODE with the state vector $\tilde{\mathbf{x}} = [\mathbf{x} \quad \boldsymbol{\lambda}]$ whereby the initial state $\mathbf{x}_0^*$ and the finale costate $\boldsymbol{\lambda}^*(T)$ are known. It is called a two point boundary value problem (TPBVP). In Section 2.2.3, a solution approach to this conditions based on augmented Lagrangian including inequality and equality constraints is presented.

Direct Methods

In contrast to the indirect methods, direct methods use the principle of "first discretize, then optimize". Therefore, the continuous time optimal control problem is discretized resulting in a finite-dimensional nonlinear program. This can be solved online using advanced mathematical optimization toolboxes. This chapter shortly introduces possible discretization and solution methods. For further information *Diehl et al.* [22] and *Nocedal* [25] are recommended.

There are three main approaches to discretize the continuous time optimization problem given in (2.7), namely single shooting, multiple shooting and the collocation methods [22]. Single shooting is a sequential approach which discretizes the whole prediction horizon with respect to the input trajectory. This leads to an optimization problem having only the inputs $\mathbf{u}$ as optimization variables. However, the optimization is very sensitive to disturbances and not suited for unstable processes. Multiple shooting splits the prediction horizon into subarcs and only discretizes over the subarcs. The continuity at the transition from one subarc to the next is ensured by additional equality constraints. When multiple shooting is applied, all states $\mathbf{x}$ and inputs $\mathbf{u}$ are optimization variables but the resulting optimization problem has sparse matrices which can be utilized by the underlying optimization.

Two methods have proven to solve the resulting nonlinear optimization problem well. Sequential Quadratic Programming (SQP) iteratively approximates a quadratic program (QP) that can be efficiently solved by active-set or interior-point QP methods [6]. Nonlinear interior-point methods approximate the inequality constraints by logarithmic penalty terms. Since the logarithm converges against infinity at the border of the inequality constraint, the constraints are always met when the solution once lies inside the feasible set [25]. A widespread software package for nonlinear interior point methods is IPOPT (**I**nterior **P**oint **OPT**imizer)[26].

2.2.3 Gradient-Based Augmented Lagrangian

In the last section, three approaches which can solve the optimal control problem were presented. The method chosen for the LLC is an indirect method, more specifically the augmented Lagrangian method invented in the 1970s by Rockafellar, Bertsekas and others [27, 28]. The core idea is to replace the constrained optimization problem by its unconstrained dual problem and solve the PMP as stated in (2.15).

In order to apply the augmented Lagrangian method, the toolbox GRAMPC is utilized [21]. It can handle optimal control problems including parameter estimation, terminal constraints, free end-time and differential-algebraic equations. For conciseness of this chapter, only the functionalities required for the solution of the optimal control problem as given in (2.7) are presented. The toolbox has proven to be real-time capable for many state of the art problems and is suitable to be implemented on embedded devices [21].

In order to consider equality and inequality constraints in the optimal control problem, the original optimization problem is replaced by its unconstrained dual problem [21, 25].

This reformulation leads to a problem that is easier to solve [25, Chapter 12.9]. The inequality constraints $\mathbf{h}$ in (2.7d) are transformed into equality constraints by means of slack variables [27]. This inherently leads to additional optimization variables. However, as derived by *Bertsekas* [27], the optimization with respect to the slack variables can be solved analytically. Therefore, the extended equality constraints $\tilde{\mathbf{g}}$ can be formulated as given in (2.16). $\mathbf{C}_h$ is a diagonal matrix of the penalty parameters $\mathbf{c}_h$ and $\boldsymbol{\mu_h}$ is a vector of multipliers of the Lagrangian as stated in (2.17b). The maximization function denotes a component-wise operator.

$$\tilde{\mathbf{g}}(\mathbf{x},\mathbf{u},t,\boldsymbol{\mu}_h,\mathbf{c}_h) = \begin{bmatrix} \mathbf{g}(\mathbf{x},\mathbf{u},t) \\ \max\left(\mathbf{h}(\mathbf{x},\mathbf{u},t), -\mathbf{C}_h^{-1}\boldsymbol{\mu}_h\right) \end{bmatrix} \tag{2.16}$$

The augmented Lagrangian formulation adjoins the extended equality constraints in (2.16) to the cost functional in (2.7a) as stated by (2.17a) by the augmented cost $\tilde{J}$. The terminal cost Φ is the same as in the original problem (2.7) because no terminal constraints are present.

The augmented integral cost $\tilde{l}$ in (2.17b) comprises the Lagrangian and an "Augmentation" term applied as a quadratic penalty function [25]. The quadratic penalty alone would need to increase its penalty parameters $\mathbf{c} = [\boldsymbol{c}_h, \quad \boldsymbol{c}_g]$ to infinity in order to converge against the optimal trajectory $(\mathbf{x}^*, \mathbf{u}^*)$ of the original problem. Consequently, the Lagrangian term with the multipliers $\boldsymbol{\mu} = [\boldsymbol{\mu}_h, \quad \boldsymbol{\mu}_g]$ is added. It can be shown that this leads to a less ill-conditioned problem [25].

$$\tilde{J}(\mathbf{x},\mathbf{u},t,\boldsymbol{\mu},\mathbf{c}) = \Phi(\mathbf{x}(T),\mathbf{u}(T),T) + \int_{t_0}^{T} \tilde{l}(\mathbf{x}(t),\mathbf{u}(t),t)dt \tag{2.17a}$$

$$\tilde{l}(\mathbf{x},\mathbf{u},t,\boldsymbol{\mu},\mathbf{c}) = \underbrace{l(\mathbf{x},\mathbf{u},t) + \boldsymbol{\mu}^T\tilde{\mathbf{g}}(\mathbf{x},\mathbf{u},t,\boldsymbol{\mu}_h,\mathbf{c}_h)}_{Lagrangian} + \underbrace{\frac{1}{2}||\tilde{\mathbf{g}}(\mathbf{x},\mathbf{u},t,\boldsymbol{\mu}_h,\boldsymbol{c}_h)||_{\mathbf{c}}^2}_{"Augmentation"} \tag{2.17b}$$

The augmented cost function $\tilde{J}$ allows to formulate the dual problem as stated in (2.18). The dual problem is easier to solve than the original optimal control problem in (2.7). $\mathbf{c}$ and $\boldsymbol{\mu}$.

$$\max_{\tilde{\boldsymbol{\mu}},\tilde{\mathbf{c}}} \quad \min_{\mathbf{u}} \quad \tilde{J}(\mathbf{u},\bar{\boldsymbol{\mu}},\bar{\mathbf{c}},\mathbf{x}_0) \tag{2.18a}$$

$$s.t. \quad \dot{\mathbf{x}}(t) = f(\mathbf{x},\mathbf{u},t), \tag{2.18b}$$

$$\mathbf{x}(0) = \mathbf{x}_0, \tag{2.18c}$$

$$\mathbf{u} \in \begin{bmatrix}\mathbf{u}_{\min} & \mathbf{u}_{\max}\end{bmatrix} \tag{2.18d}$$

The problem formulation is solved by an alternating manner of inner minimization and an outer maximization. The inner minimization is realized by a by a projected gradient method with constant penalty parameters $\tilde{\mathbf{c}}$ and multipliers $\tilde{\boldsymbol{\mu}}$. The outer maximization is applied via a steepest descent update of the multipliers $\boldsymbol{\mu}$ and a heuristic update of the penalties $\mathbf{c}$.

Inner Minimization via Projected Gradient Method

The inner minimization solves the dual problem as stated in (2.18) with fixed penalty parameters $\boldsymbol{c}$ and multipliers $\boldsymbol{\mu}$. Therefore, the algorithm iteratively searches for a solution of the necessary conditions of optimality as stated by the PMP conditions in (2.15). It is a steepest descent method that can consider the input box constraints in (2.18d) by projecting them into the feasible region via clipping. Initialized with a first guess of the input trajectory $\mathbf{u}^0$ and of the state trajectory $\mathbf{x}^0$, the projected gradient method iterates to the optimal point by the following procedure whereby the current iteration is denoted by j:

1. **Backward integration of the costate $\boldsymbol{\lambda}$**: At first the trajectory of the costate is backward integrated by (2.15e) and (2.15c). GRAMPC offers different integration schemes. Euler, modified Euler and Heun are three integration schemes with fixed step size. They are the easiest to calculate but might need a small step size for stiff systems [29]. In addition to the fixed step size integration methods, a variable step size 4th-Runge-Kutta integration method is offered leading to a higher robustness but also increases the computational cost. Stiffness of a system is a guideline to choose the adequate integration methods but it is often chosen empirically [29].

2. **Calculate search direction $\mathbf{d}_u^j$**: With the knowledge of an input trajectory $\mathbf{u}^j$, a state trajectory $\mathbf{x}^j$ and a costate trajectory $\boldsymbol{\lambda}^j$, the minimization problem as given in (2.15d) is solved. Firstly, the steepest descent search direction $\mathbf{d}_u^j$ is calculated by differentiating the Hamiltonian H with respect to $\mathbf{u}$.

$$\mathbf{d}_u^j = \frac{dH(\mathbf{x}, \boldsymbol{\lambda}, \mathbf{u})}{d\mathbf{u}} \tag{2.19}$$

3. **Calculate step size α**: Choosing the step size α is a relevant choice in order to increase robustness and convergence speed of the algorithm. GRAMPC offers two different methods to solve the line search problem in (2.20). The adaptive strategy approximates the cost function by a polynomial of second order and finds the optimal α of the approximated cost function. The disadvantage of this approach is that it requires high computational cost. It can be reduced by choosing an explicit line search strategy that gives the solution analytically [30].

$$\min_{\alpha > 0} \tilde{J}(\mathbf{u}^j - \alpha \mathbf{d}_u^j; \mathbf{x}_0) \tag{2.20}$$

   Because the choice of the step size α is performed in all search directions simultaneously, the states $\mathbf{x}$ and inputs $\mathbf{u}$ should be of the same order of magnitude. Therefore, the system needs to be scaled. GRAMPC offers an internal scaling procedure. However, it is recommended to scale the system beforehand in order to increase the computational speed.

4. **Update input trajectory $\mathbf{u}^j$**: Utilizing the gradient direction $\mathbf{d}_u^j$ and the step size α, the updated input trajectory $\mathbf{u}^j$ can be calculated by (2.21). In order to consider the box constraint on the inputs $\mathbf{u}$, the inputs are clipped to their minimum and maximum values respectively.

$$\mathbf{u}^{j+1} = \begin{cases} \mathbf{u^j} - \alpha \mathbf{d}_u, & \text{if} \quad \mathbf{u}^{j+1} > \mathbf{u}_{\text{min}} \land \mathbf{u}^{j+1} < \mathbf{u}_{\text{max}} \\ \mathbf{u}_{\text{max}}, & \text{else if} \quad \mathbf{u}^{j+1} > \mathbf{u}_{\text{max}} \\ \mathbf{u}_{\text{min}}, & \text{else if} \quad \mathbf{u}^{j+1} < \mathbf{u}_{min} \end{cases} \tag{2.21}$$

5. **Update state trajectory $\mathbf{x}^j$**: Subsequently, the state trajectory $\mathbf{x}^j$ is forward integrated according to (2.15a) and (2.15b). For the integration, the same approaches as in step 1 can be utilized.

6. **Convergence check**: The inner minimization can stop due to two criterion. In order to find the optimal point, a convergence check can be utilized by calculating the relative gradients of the input trajectory $\mathbf{u}^j$. Alternatively, the loop is terminated after a fixed number of iterations j_{max}.

Outer Maximization via Steepest Descent

When the inner minimization of the problem formulation as stated by (2.18) with fixed penalties $\mathbf{c}$ and multipliers $\boldsymbol{\mu}$ returns a solution, the outer maximization is applied. In this step, the multipliers $\boldsymbol{\mu}$ are updated by means of a steepest descent and the penalty parameters $\mathbf{c}$ by a heuristic approach [25]. In (2.22), the multipliers μ_g^i and μ_h^i are updated for a single equality constraint g^i or inequality constraint h^i at the current iteration step i. The direction is the residual of the constraint g^i or h^i while the penalty parameter c^i serves as a step size parameter. The factor ρ is introduced in order to increase the robustness. The update is skipped if the constraints g^i or h^i are satisfied within some limit ϵ_g or ϵ_h or if the inner minimization did not converge. The convergence is checked by the maximum relative gradient η^i which has to be lower than a threshold $\epsilon_{\text{rel,u}}$. The multipliers μ^i of the inactive inequality constraints h^i are always updated.

$$\mu_g^{i+1} = \begin{cases} \mu_g^i + (1-\rho) c_g^i g^i(\mathbf{x}^i, \mathbf{u}^i), & \text{if} \quad |g^i| > \epsilon_g \land \eta^i \leq \epsilon_{\text{rel,u}} \\ \mu_g^i, & \text{else} \end{cases} \tag{2.22a}$$

$$\mu_h^{i+1} = \begin{cases} \mu_h^i + (1-\rho) c_h^i h^i(\mathbf{x}^i, \mathbf{u}^i), & \text{if} \quad (|h^i| > \epsilon_h \land \eta^i \leq \epsilon_{\text{rel,u}}) \lor h^i < 0 \\ \mu_h^i, & \text{else} \end{cases} \tag{2.22b}$$

The penalty update is given by a heuristic approach as stated in (2.23). The penalties c_g and c_h are increased by the factor β_{in} if the inner minimization is converged and the last iteration showed insufficient improvement which is quantified by the parameter γ_{in}. The penalties are decreased by the factor β_{de} if the inner minimization converged and the last iteration had sufficient improvement which is quantified by the parameter γ_{de}. In addition, the penalty parameters c_g^i and c_h^i are bounded by minimum c_{min} and maximum

$c_{\max}$ values. Note that especially the $c_{\min}$ has a great influence on constraints violation and convergence speed when only a few iterations are executed [21]. Therefore, $c_{\min}$ needs to be tuned carefully for the LLC.

$$c_g^{i+1} = \begin{cases} \beta_{\text{in}} c_g^i, & \text{if} \quad (|g^i| \geq \max\{\gamma_{\text{in}} |g^{i-1}|, \epsilon_g\}) \wedge \eta^i \leq \epsilon_{\text{rel,u}} \\ \beta_{\text{de}} c_g^i, & \text{else if} \quad |g^i| \leq \gamma_{\text{de}} \epsilon_g \\ c_g^i, & \text{else} \end{cases} \tag{2.23a}$$

$$c_h^{i+1} = \begin{cases} \beta_{\text{in}} c_h^i, & \text{if} \quad |h^i| \geq \max\{\gamma_{\text{in}} |h^{i-1}|, \epsilon_h\} \wedge \eta^i \leq \epsilon_{\text{rel,u}} \\ \beta_{\text{de}} c_h^i, & \text{else if} \quad |h^i| \leq \gamma_{\text{de}} \epsilon_h \\ c_h^i, & \text{else} \end{cases} \tag{2.23b}$$

2.2.4 Model Predictive Control

Model predictive control (MPC) is a high control approach that has been used extensively in the process engineering since the 1980s [6]. In recent years, increasing computational capabilities led to the possibility of applying MPC also to processes with a short sampling time. The basic idea is to iteratively solve the optimal control problem in every time step and applying the first input to the system. This principle is called "receding horizon". Consequently, the controller can react to disturbances and modeling errors. Due to the following reasons, MPC became the most popular high control approach [31].

- **Explicit compliance with constraints**: In nearly all processes some limitations which can either be on inputs, states or outputs of the system are present. In conventional control approaches, those limitations are considered by either a conservative tuning of control parameters or by anti-windup techniques. Note that those strategies can lead to instabilities. Therefore, the explicit consideration of constraints by the MPC is favorable.

- **Inherent decoupling**: If the process model is a multiple-input multiple-output (MIMO) system, the MPC leads to an inherent decoupling of the inputs and outputs. In classical control approaches, so called decoupling controllers need to be designed in order to transform the MIMO system into single-input single-output (SISO) systems.

- **Reference and disturbance prediction**: MPCs can consider predictions of reference and disturbance trajectories. Therefore, the controller can act upon changes rather then reacting on the control error.

- **Optimal behavior**: In comparison to classical control approaches where the control parameters are tuned until a desired behavior is achieved, the MPC behaves optimal with respect to a user chosen objective function which is more intuitive for a non-technical person. The objective function does not necessarily describe a reference tracking but it can also describe a cost minimization in terms of hydrogen consumption, profit maximization or others. This kind of MPCs are also called economic MPC [32].

In Figure 2.7, the moving horizon principle of an MPC is presented. In the illustration, the control objective is that the system output $\mathbf{y}_k(\cdot)$ follows the reference $\mathbf{r}_k(\cdot)$ by manipulating the input $\mathbf{u}_k(\cdot)$ minimizing the quadratic error. The more general problem formulation in (2.7) with an arbitrary cost function works the same way but it is less intuitive to illustrate. Compared to the last section, the nomenclature changed to discrete time. The index k refers to the current time step at which the MPC is executed. The prediction horizon N_P describes the length for which the cost function is optimized. The control horizon N_C gives the number of time steps until the MPC can influence the input. This gives the degree of freedom of the controller. In many applications, the control horizon N_C equals the prediction horizon N_P leading to the maximal degree of freedom for the controller.

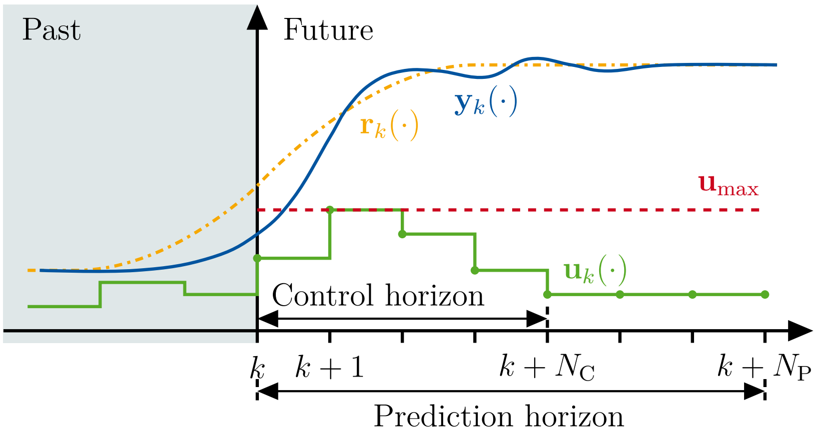

Fig. 2.7: Principle of model predictive control [31].

Because the sample time Δt might be short, it can be difficult to solve the optimization problem within the sampling time especially for nonlinear problems. However, one advantage of choosing a short sample time is that the solution of the optimization problems often do not differ much from one time step to the next. Therefore, the solution of the last time step is shifted by one time step in the next iteration and utilized as the initial guess for the next optimization. This is called a warm-start strategy and is commonly applied [22]. Additionally, the optimization problem is often not solved until full convergence but only for a fixed number of iterations. It is assumed that the optimization problem converges over time. This is called a real-time iteration scheme. A disadvantage is the difficult proof of stability [22].

The MPC needs full knowledge of all states $\mathbf{x}$ at time k. In practice however, not all states are measurable or it is economically not reasonable to do so. Therefore, state estimators need to be applied. For nonlinear systems, the extended Kalman filter and the unscented Kalman filter are popular approaches [6].

An internal controller model is used to predict the future behavior of the process. In practice this cannot be done arbitrarily accurate and modeling errors are always present. It can be shown that this inherently leads to offset errors in the reference tracking for an MPC [31]. In classical control approaches, integral behavior is utilized to prevent offset errors. In the MPC, so called disturbance observers are applied. A simple approach is the dynamic matrix control (DMC) where the disturbance is estimated by the offset of the measured and the estimated output.

$$\mathbf{d}(k) = \mathbf{y}_m(k) - \hat{\mathbf{y}}(k) \tag{2.24}$$

$\mathbf{y}_m(k)$ described the measurement of the outputs and $\hat{\mathbf{y}}(k)$ is the estimate of the prediction model calculated at time $k-1$. The offset is assumed to be constant for the prediction horizon and added to the reference trajectory $\mathbf{r}_k(\cdot)$. It can be shown that in many cases this leads to an offset-free tracking [6].

2.3 Literature Review on Methods for the Power Management

A hierarchical control structure for a fuel cell hybrid vehicle is presented in Figure 2.8. The driver requests a certain power demand P_{dem} at the DC bus. The high-level control (HLC) optimizes the power split between the battery and the fuel cell system and passes the corresponding reference values $P_{\text{bat,bus,ref}}$ and $P_{\text{fcs,bus,ref}}$ to the LLC. The LLC regulates the fuel cell system and the battery by the input variables $\mathbf{u}$. Based on the outputs $\mathbf{y}$ from the vehicle, the state estimator predicts the states $\hat{\mathbf{x}}^h$ for the HLC and the states $\hat{\mathbf{x}}^l$ for LLC . As the state estimator is not part of this thesis, perfect state knowledge is assumed. Instead, the focus lies on the control design of the LLC as well as of the HLC. Current approaches to design those controllers are introduced in this section. In Section 2.3.1, current approaches for the LLC control are presented, followed by Section 2.3.2, where HLC methods to find the optimal power split between the fuel cell system and the battery are shown.

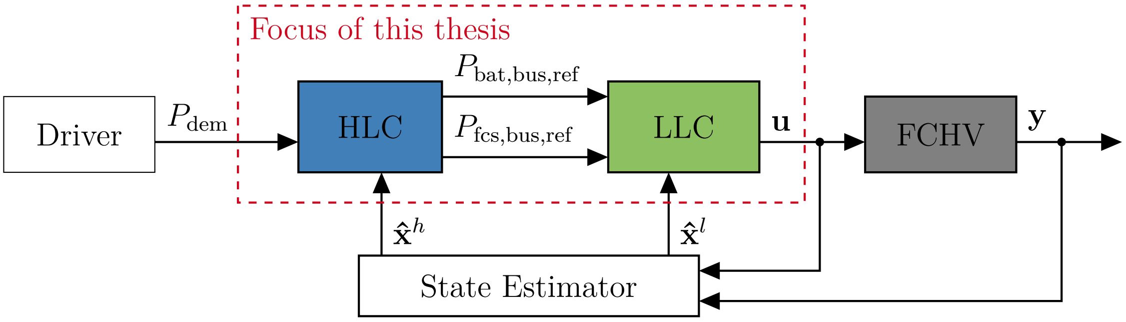

Fig. 2.8: Overview of the hierarchical control structure [33].

2.3.1 Review on Low-Level Control

The LLC is responsible for the control of the fuel cell system and the battery. Controlling the fuel cell system includes the peripheral components in Figure 2.3. While the heat management and hydrogen supply can be considered separately from the power management, the air supply has to be taken into account cohesively [34–36].

The compressor and back pressure valve are the actuators of the air supply system leading to two additional degrees of freedom that can be exploited to find an optimal operating point of the air supply. In [9, 37–39], the oxygen excess ratio λ_{O_2} is considered as a performance indicator for energy efficiency. However, this only exploits one degree of freedom. When compressor and back pressure valve are both considered, the air mass flow rate $\dot{m}_{\mathrm{cr}}$ and the pressure ratio Π can be regulated independently. In [40, 41], the optimal operating point of the air supply is chosen not only regarding energy efficiency but also regarding air humidification, transient operation and other performance indicators.

The air supply of the fuel cell system is a coupled MIMO system by itself when the $\dot{m}_{\mathrm{cr}}$ and Π are regulated. In order to quantify the coupling of the air supply, *Zhao et al.* [35] apply the relative gain array (RGA) as a coupling indicator for different operating points in the compressor map. The chosen system in this thesis is also analyzed with the RGA in Appendix A.3 indicating a strong coupling.

Subsequently, different control schemes that control the battery and fuel cell system power as well as the air supply are introduced. They are distinguished by their control objectives.

- **Air mass flow rate tracking**: When the air mass flow rate is tracked in terms of the oxygen excess ratio λ_{O_2}, the compressor is the only actuator of the air supply and the stack current is handled as a system disturbance [9, 38, 39, 42–44]. Approaching the strong nonlinearity of the compressor, a dynamic feedforward controller consisting of a feedforward map to handle the nonlinearity and of a dynamic feedback control to handle the model mismatches is proposed [9]. Apart from that, a sliding mode controller is used in [42]. Furthermore, nonlinear and explicit MPC methods are employed in order to take predictive information and explicit constraints compliance into account [38, 39, 43, 44].

- **Pressure and air mass flow rate tracking**: Control strategies to decouple air mass flow rate and pressure are employed in [35, 45]. Meshed PI-Controller have been used with an additional reference limiter for surge prevention[35]. In [45], an linear quadratic regulator (LQR) method is used to control air mass flow rate and pressure independently. The stack current is handled as a disturbance for both cases.

- **Fuel cell system power and air mass flow rate tracking**: In [9], an LQR control is proposed to handle the coupling of the power control and the air supply.

The performance indicator of the controller is again the oxygen excess ratio and no pressure regulation is applied.

- **Fuel cell system power, pressure and air mass flow tracking**: A hierarchical nonlinear MPC control is proposed for the fuel cell system power and air supply control [46]. While the high-level takes over the power control and determines the optimal operating point of the air supply, the low-level regulates the optimal operating point. The high-level must explicitly constrain the fuel cell dynamics because it cannot inherently comply with the air supply constraints due to the controller distribution.
- **Dynamic power split control**: In [47], an MPC is employed in order to dynamically relieve the load on the fuel cell system by utilizing the battery for transient operation. This way the dynamic power delivery can be increased. In [48], an LQR is proposed to optimally distributing the power demand at transient operation avoiding fuel cell starvation.

To the authors best knowledge, there is not yet a centralized control method that combines all of the above mentioned control objectives.

2.3.2 Review on High-Level Control

The static power split between the fuel cell system and the battery is a well studied problem in literature [36]. Most approaches rely on the assumption that the whole driving cycle is perfectly known a-priori. This is not valid for real-world applications. Nevertheless, these theoretical approaches give a lot of insights into the problem. In (2.25), the optimization problem for a driving cycle from t_0 until T is given. The goal is to minimize the hydrogen consumption of the fuel cell system $\dot{m}_{H_2}$ in (2.25a) and to achieve a final SOC of the battery that equals the initial SOC by (2.25c). For the whole driving cycle, the demanded power at the DC bus has to be delivered by the summation of the fuel cell system and the battery power by (2.25d). Additionally, the minimum and maximum power for $P_{\text{bat,bus}}$ and $P_{\text{fcs,bus}}$ have to be considered by (2.25f) and (2.25g).

$$\begin{aligned}
\min_{\mathbf{u}} \quad & J = \int_{t_0}^{T} \dot{m}_{H_2} dt && \text{(2.25a)}\\
s.t. \quad & \dot{\text{SOC}} = f(\text{SOC}, P_{\text{bat,bus}}) && \text{(2.25b)}\\
& \text{SOC}(t_0) = \text{SOC}(T) && \text{(2.25c)}\\
& P_{\text{dem}} = P_{\text{fcs,bus}} + P_{\text{bat,bus}} && \text{(2.25d)}\\
& \text{SOC}_{\text{min}} < \text{SOC} < \text{SOC}_{\text{max}} && \text{(2.25e)}\\
& P_{\text{fcs,bus,min}} < P_{\text{fcs,bus}} < P_{\text{fcs,bus,max}} && \text{(2.25f)}\\
& P_{\text{bat,bus,min}} < P_{\text{bat,bus}} < P_{\text{bat,bus,max}} && \text{(2.25g)}
\end{aligned}$$

With a-priori knowledge of the driving cycle, the power split can be calculated globally optimally using DP under the assumption that the grid discretization is chosen dense enough. This has been studied by *Odeim* [49], *Bertsekas* [23] and *Kim et al.* [5]. The solution of the dynamic programming can be used as a reference in order to validate real-world applicable methods.

Likewise, the optimization problem can also be solved by deriving the PMP for the given problem. The costate λ serves as a time dependent weighting factor between the battery power $P_{\text{bat,bus}}$ and $P_{\text{fcs,bus}}$. Even though the PMP only provides necessary conditions for optimality, it is shown by *Kim et al.* [5] that solving the PMP leads to similar results as the DP approach and that it can be calculated faster. It has also been shown that the costate λ does not vary a lot over a driving cycle and that a constant λ can also reach nearly optimal results. One disadvantage is that λ strongly depends on the driving cycle and that it is not continuous when the battery SOC threshold is reached [49].

Real-world applicable methods are found on rule-based approaches, equivalent consumption minimization strategy (ECMS) or model predictive control (MPC). Those approaches can only achieve almost optimal solutions but they do not need to know the whole driving cycle a-priori.

Rule-based approaches such as fuzzy logic control utilize "if-then rules" [50, 51]. The power split decision is based on the current battery SOC and on the demanded power P_{dem}. Rule-based approaches can reach nearly optimal results on trained driving cycles but they might perform worse on arbitrary driving cycles.

The equivalent consumption minimization strategy (ECMS) is an optimal control approach that weights the battery power $P_{\text{bat,bus}}$ and the hydrogen consumption $\dot{m}_{H_2}$ in the cost function given by (2.26) where s is the weighting factor [50–53]. The objective function can be interpreted similarly to the PMP approach whereby the weighting factor s mimics the costate λ. A robust adaption of the optimal costate λ by the weighting factor s is extensively studied in literature.

$$\min \dot{m}_{H_2} + s \cdot P_{\text{bat}} \tag{2.26}$$

Apart from that, the optimal power split can be calculated by MPC [11, 54, 55]. In this case, the goal is to solve the optimization problem in (2.25) over a finite prediction horizon T_{P} instead of the whole driving cycle. The final state constraint (2.25c) is reformulated as a final cost function. Otherwise, the solution might become infeasible for a short prediction horizon T_{P}. The constraint (2.25d) can also be handled as a quadratic reference cost function instead of an equality constraint.

3 Control-Oriented Modeling

In this chapter, the controller model is presented. There are many ways to derive the controller model. Black box modeling techniques such as Volterra Series Models or Neural Networks are predominantly used [35, 38, 56]. The controller model used in this thesis is based on a gray model that captures the main physical relationships but also utilizes parameter estimation (e.g. compressor map). In Section 3.1, the electrochemistry of the fuel cell is presented as a static model. In Section 3.2, the air supply of the fuel cell system is derived. Subsequently, the battery model is explained in Section 3.3 followed by the introduction of the DC/DC converter models in Section 3.4.

3.1 Fuel Cell Electrochemistry Model

The performance of an elementary fuel cell is described by the polarization curve in Figure 3.1. It is presented by the cell voltage U_{fc} (in blue) for a given current density i_{fc} which corresponds to the stack current I_{st} normalized by the electrolyte area A_{cell} as given in (3.1). This makes the performance of a fuel cell comparable with different fuel cell sizes.

$$i_{\mathrm{fc}} = \frac{I_{\mathrm{st}}}{A_{\mathrm{cell}}} \tag{3.1}$$

The produced fuel cell stack power P_{st} (in red) as given in (3.2) depends on the current density i_{FC}. The maximum power is reached for current densities i_{fc} between 1400 $\frac{\mathrm{mA}}{\mathrm{cm}^2}$ and 1600 $\frac{\mathrm{mA}}{\mathrm{cm}^2}$. The cell voltage U_{fc} and the stack power P_{st} depend on the cathode pressure which is displayed by the dotted lines. An increase in pressure leads to a higher stack power P_{st} for the same i_{fc}. Taking into account that the hydrogen consumption $\dot{m}_{H_2}$ is proportional to the current density i_{fc}, it may lead to the assumption that increasing the pressure leads to higher efficiency of the fuel cell system. This is correct for the stack power P_{st} but not for the overall fuel cell system power $P_{\mathrm{fcs,net}}$ which takes into account the power consumption of the peripheral components. The fuel cell system power $P_{\mathrm{fcs,net}}$ is defined by (3.3). It consists of the produced stack power P_{st} minus the electrical power consumption of the compressor motor P_{cm} minus a constant auxiliary power P_{aux} that summarizes the consumption of all other peripherals [9].

$$P_{\mathrm{st}} = n_{\mathrm{fc,cell}} U_{\mathrm{fc}} i_{\mathrm{den}} A_{\mathrm{cell}} \tag{3.2}$$

$$P_{\mathrm{fcs,net}} = P_{\mathrm{st}} - P_{\mathrm{cm}} - P_{\mathrm{aux}} \tag{3.3}$$

The cell voltage U_{fc} can be described as follows [4]:

$$U_{\mathrm{fc}} = E_{\mathrm{rev}} - \Delta U_{\mathrm{act}} - \Delta U_{\mathrm{ohm}} - \Delta U_{\mathrm{conc}} \tag{3.4}$$

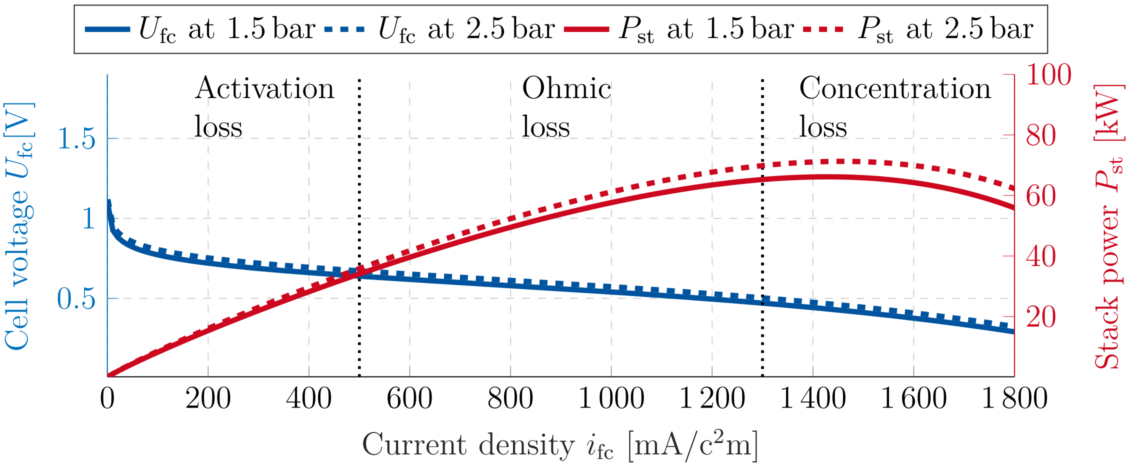

Fig. 3.1: Polarization curve of an elementary fuel cell and resulting stack power.

The reversible voltage E_{rev} stands for the voltage at which the process would be idea. In this case, the fuel cell would deliver a constant voltage, regardless of how much current I_{st} is drawn. However, there is a voltage drop caused by different phenomena. These losses are presented by the overvoltages ΔU_{act}, ΔU_{ohm} and ΔU_{conc} and correspond to the activation, ohmic as well as concentration losses in Figure 3.1. Subsequently, these losses will be presented in-depth.

The model of the elementary fuel cell is adopted from previous work and is fitted to the Heliocentris Hybrid Energy Lab-System located at the Institute of Automatic Control, RWTH Aachen University [7, 57]. The parameters for the electrochemical model and the fuel cell stack are given in Appendix A.1.

Reversible Voltage

The reversible voltage E_{rev} in (3.5) is a theoretical value that describes the voltage at which the process would be reversible.

$$E_{\text{rev}} = E^0_{\text{rev}} - k_{\text{t}} \left(T_{\text{st}} - T^0 \right) + \frac{R_{\text{u}} T_{\text{st}}}{2F} \cdot \ln \left(p_{H_2} \cdot \sqrt{p_{O_2}} \right) \tag{3.5}$$

E^0_{rev} describes the reversible voltage at nominal conditions (T^0, p^0), F depicts the Faraday constant, k_{t} expresses the temperature coefficient and T_{st} is the stack temperature. R_{u} describes the universal gas constant, p_{H_2} is the partial pressure of hydrogen at the anode and p_{O_2} is the partial pressure of oxygen at the cathode. The first term of (3.5) describes the reversible voltage under nominal conditions, the second term depicts the influence of deviation in the stack temperature T_{st} from the nominal conditions and the third term expresses the influence of deviation in partial oxygen p_{O_2} and hydrogen p_{H_2} pressure by the Nernst equation [4].

The control of the fuel cell system is designed in such a way that the partial pressure of hydrogen p_{H_2} at the anode is following the cathode pressure p_{cat} in order to minimize the pressure drop across the membrane. The partial pressure of oxygen p_{O_2} depends on the cathode pressure p_{cat} and on the oxygen excess ratio λ_{O_2}. Consequently, the reversible voltage E_{rev} and the stack power P_{st} can be influenced by regulating the cathode pressure p_{cat} and oxygen excess ratio λ_{O_2}.

$$E_{\mathrm{rev}} = E^0_{\mathrm{rev}} - k_{\mathrm{t}} \left(T_{\mathrm{st}} - T^0\right) + \frac{R_{\mathrm{u}} T_{\mathrm{st}}}{2F} \cdot \ln \left(p_{\mathrm{cat}} \cdot \sqrt{f(p_{\mathrm{cat}}, \lambda_{O_2})}\right) \tag{3.6}$$

Activation Loss due to Electrochemical Reaction

The activation loss ΔU_{act} is caused by the inertia of the reactions taking place on the surface of the electrodes. A part of the voltage is lost by the chemical reaction that transfers the electrons to or from the electrodes. The activation loss leads to a rapid decrease in the cell voltage U_{fc} for low current densities i_{fc} (compare Figure 3.1) [4].

Amphlett et al. [58] describe a function for the activation loss that depends on partial pressures of oxygen p_{O_2} and hydrogen p_{H_2} as well as the stack current I_{st} and stack temperature T_{st} in (3.7). The parameters ξ_i are based on physical characteristics.

$$\Delta U_{\mathrm{act}} = -\left[\xi_1 + \xi_{2,\mathrm{var}} T_{\mathrm{st}} + \xi_3 T_{\mathrm{st}} \left[\ln\left(c_{O_2}\right)\right] + \xi_4 T_{\mathrm{st}} \ln(I_{\mathrm{st}})\right] \tag{3.7}$$

The concentration of oxygen c_{O_2} and hydrogen c_{H_2} at the membrane can be found in (3.8) and (3.9) and the parameter $\xi_{2,var}$ in (3.10).

$$c_{O_2} = p_{O_2} \cdot 1.97 \cdot 10^{-7} \cdot \exp\left(\frac{498}{T_{\mathrm{st}}}\right) \tag{3.8}$$

$$c_{H_2} = p_{H_2} \cdot 9.174 \cdot 10^{-7} \cdot \exp\left(\frac{-77}{T_{\mathrm{st}}}\right) \tag{3.9}$$

$$\xi_{2,\mathrm{var}} = \xi_{2a} + \xi_{2b} \ln\left(A_{\mathrm{cell}}\right) + \xi_{2c} \ln\left(c_{H_2}\right) \tag{3.10}$$

As for the reversible voltage E_{rev}, the partial pressures of oxygen p_{O_2} and hydrogen p_{H_2} also have an influence on the activation loss ΔU_{act}. Therefore, increasing cathode pressure p_{cat} and oxygen excess ratio λ_{O_2} lead to a reduced activation loss ΔU_{act}.

Ohmic Loss due to Ionic and Electronic Conduction

The ohmic loss ΔU_{ohm} is nearly proportional to the stack current I_{st} and describes the resistance of the flow of electrons through the material of the electrodes, the electrolyte and various interconnections [4].

Dirkes describes the ohmic losses based on the empirical formula in (3.11) which is dependent on the stack temperature T_{st} and the stack current I_{st}. Additionally, the formula is determined by the water content in the membrane λ_M, the thickness of the membrane δ_M and the surface area of the electrolyte A_{cell}. The ohmic losses dominate the influence on the cell voltage U_{fc} for medial stack current I_{st} (compare Figure 3.1). λ_M is constant because an ideal humidification is assumed. [7]

$$\Delta U_{\text{ohm}} = \frac{181.6\left[1 + 0.03\left(\frac{I_{\text{st}}}{A_{\text{cell}}}\right) + 0.062\left(\frac{T_{\text{st}}}{303}\right)^2 \cdot \left(\frac{I_{\text{st}}}{A_{\text{cell}}}\right)^{2.5}\right] \cdot \delta_M}{\left(\lambda_M - 0.634 - 3\left(\frac{I_{\text{st}}}{A_{\text{cell}}}\right)\right) \cdot \exp\left(4.18\left(\frac{T_{\text{st}}-303}{T_{\text{st}}}\right)\right) \cdot A_{\text{cell}}} \cdot I_{\text{st}} \tag{3.11}$$

Concentration Loss due to Mass Transport

The concentration loss results from the changes in concentration of the reactants at the surface of the electrodes as the fuel is used. The loss is caused by a failure to transport sufficient reactant to the electrode surface and is therefore also called mass transport loss [4].

The concentration loss is given in (3.12) as an empirical description parameterized by the m and n. Despite the fact that the formula has no physical meaning, it gives a good fit to the results [4]. The concentration loss dominates the behavior of high current densities i_{fc} and it exponentially depends on the stack current I_{st}.

$$\Delta U_{\text{conc}} = m_{\text{con}} \cdot \exp\left(n_{\text{conc}} \cdot I_{\text{st}}\right) \tag{3.12}$$

3.2 Air Supply Model

In this section, the prediction model of the air supply is presented. Compared to the plant which is based on *Pukrushpan et al.* [9] several simplification are introduced. The following general assumptions are made for the prediction model:

- The cooler and humidifier are neglected (compare Figure 2.3).
- The inlet air of the compressor is at nominal conditions ($T_{\text{cp,in}} = T^0$ and $p_{\text{cp,in}} = p^0$).
- The relative air humidity is neglected.

An overview of the air supply model is shown in Figure 3.2. The blue arrows represent the air mass flow rates $\dot{m}$, the red labels define the states of the fuel cell system $\mathbf{x}_{\text{fcs}}$ and the green labels are input variables $\mathbf{u}$. The model comprises two actuators (compressor and back pressure valve). Additionally, three manifolds, which lump together volumes, pipes and other components, represent the fluid mechanics of the system. The parameters of the air supply model are listed in Table A.3. If not other stated, the derivation depends on *Larminie et al.* [4] and *Pukrushpan et al.* [9].

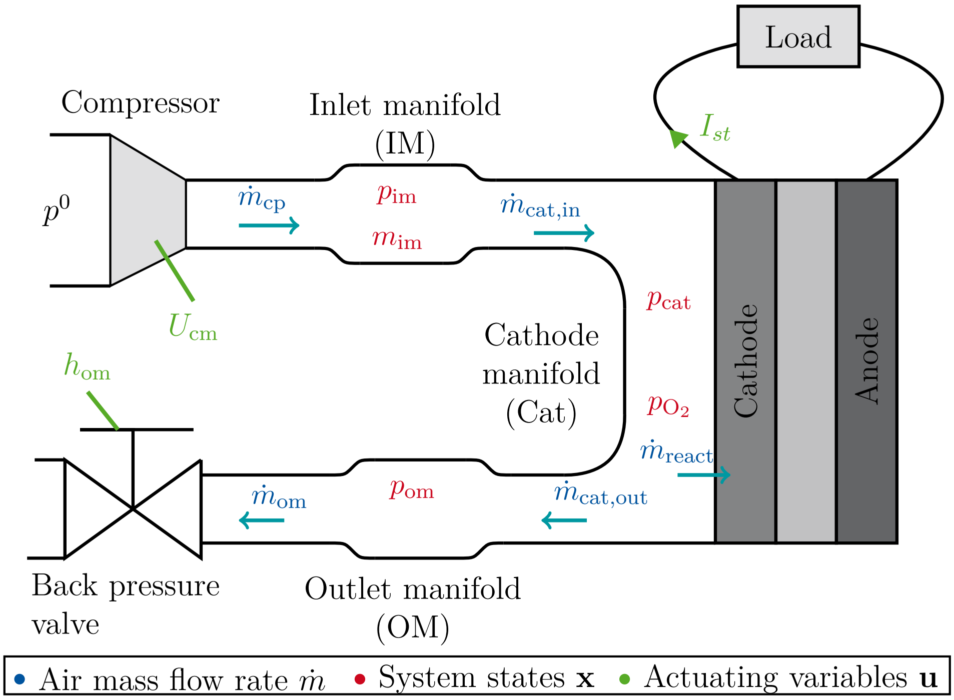

Fig. 3.2: Air supply model including manifolds, compressor and back pressure valve [59].

Compressor Model

In Figure 3.3, a dynamic model of the compressor is given. Inputs to the system are the motor voltage of the compressor U_{cm} and the pressure ratio across the compressor Π. Since the inlet pressure $p_{\mathrm{cp,in}}$ and temperature $T_{\mathrm{cp,in}}$ are at nominal conditions, the pressure ratio Π is proportional to the pressure of the inlet manifold p_{im}.

$$\Pi = \frac{p_{\mathrm{im}}}{p^0} \tag{3.13}$$

The motor U_{cm} is the input variable of the compressor motor and manipulates the rotational speed ω_{cp}. The equation for the change in rotational speed as given in (3.14) depends on the inertia of the motor J_{cm} and the difference between the produced motor torque τ_{cp} and the required mechanical torque τ_{cm}.

$$\frac{d\omega_{\mathrm{cp}}}{dt} = \frac{1}{J_{\mathrm{cm}}}\left(\tau_{\mathrm{cm}} - \tau_{\mathrm{cp}}\right) \tag{3.14}$$

The generated motor torque τ_{cm} is derived by a simplified model of an electrical motor [60]. It is proportional to the motor current I_{cm}. Dynamics of the electrical subsystem as well as brush losses and mechanical friction are neglected. Instead, the generated motor torque is multiplied by an overall motor efficiency η_{cm}. R_{cm} denotes the motor resistance and k_{T} the motor torque constant.

$$\tau_{\mathrm{cm}} = k_{\mathrm{T}}\eta_{\mathrm{cm}}I_{\mathrm{cm}} = k_{\mathrm{T}}\eta_{\mathrm{cm}}\frac{U_{\mathrm{cm}} - k_{\mathrm{T}}\omega_{\mathrm{cp}}}{R_{\mathrm{cm}}} \tag{3.15}$$

The compressor torque τ_{cp} and output temperature $T_{\mathrm{cp,out}}$ in Figure 3.3 are calculated from the compressor air mass flow rate $\dot{m}_{\mathrm{cp}}$ and the pressure ratio Π as given in (3.16) and (3.17). Derivations of the thermodynamic equations can be found in [4] whereat γ is the ratio of specific heats of air and c_{p} is the specific heat capacity of air.

$$T_{\mathrm{cp,out}} = T^0 \left(1 + \frac{\Pi^{\frac{\gamma-1}{\gamma}} - 1}{\eta_{\mathrm{cp}}\left(\Pi, \dot{m}_{\mathrm{cp}}\right)}\right) \tag{3.16}$$

$$\tau_{\mathrm{cp}} = \frac{c_p\left(\Pi^{\frac{\gamma-1}{\gamma}} - 1\right)}{\omega_{\mathrm{cp}}\eta_{\mathrm{cp}}\left(\Pi, \dot{m}_{\mathrm{cp}}\right)} \tag{3.17}$$

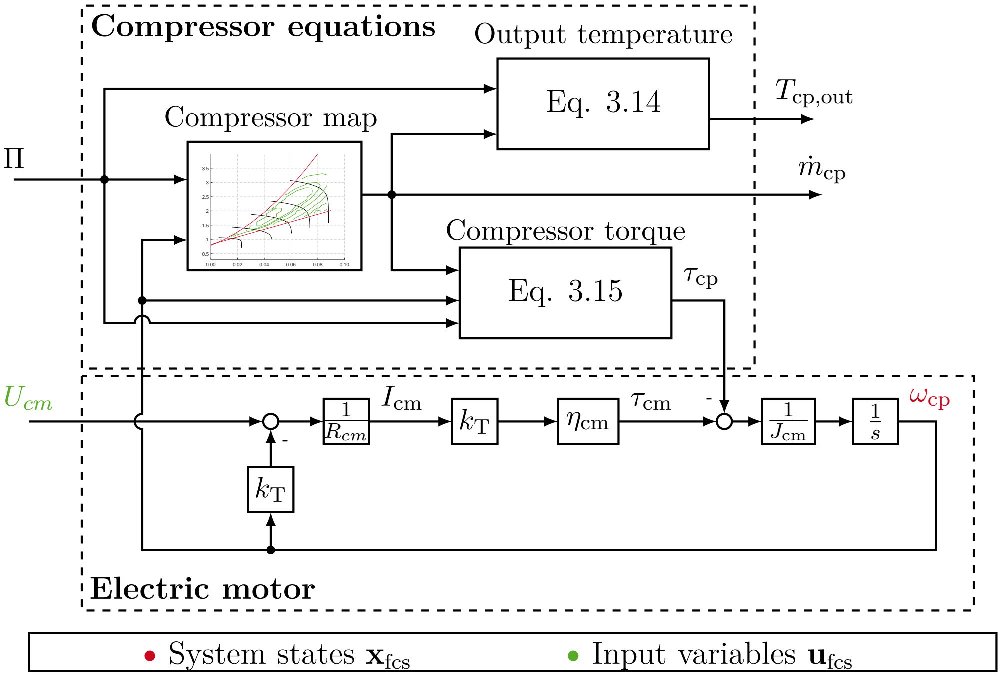

Fig. 3.3: Block diagram of compressor model.

The compressor map (introduced in Figure 2.4) is used to find the corrected air mass flow rate $\dot{m}_{\mathrm{cr}}$ based on the pressure ratio Π and the rotational speed ω_{cp}. Under nominal conditions, the corrected air mass flow rate $\dot{m}_{\mathrm{cr}}$ is proportional to the compressor air mass flow rate $\dot{m}_{\mathrm{cp}}$ as given in (2.5). In *Pukrushpan et al.* [9], the map is estimated on the basis of experimental data with the Jensen & Kristensen method [61]. Because the equations resulting from this method are complex, it increases the computational cost of the MPC. Thus, a polynomial approximation of second order in the pressure ratio Π and of third order in the rotational speed ω_{cp} is taken:

$$\dot{m}_{\mathrm{cr}} = f(\omega_{\mathrm{cp}}, \Pi) \approx \sum_{i=1}^{3}\sum_{j=1}^{2} a_{ij} \cdot \omega_{\mathrm{cp}}^{i} \cdot \Pi^{j} \tag{3.18}$$

The parameters a_{ij} are fitted by least square with the Curve Fitting Toolbox in MATLAB®. The estimation error of the corrected air mass flow rate $\dot{m}_{\mathrm{cp}}$ is presented in Figure 3.4a. In most cases, the estimation error lies below 0.5 %. Only at the choke boundary for high air mass flow rates $\dot{m}_{\mathrm{cr}}$ and at the surge boundary for medium high air mass flow rates $\dot{m}_{\mathrm{cr}}$, the estimation error is up to 1.5 %.

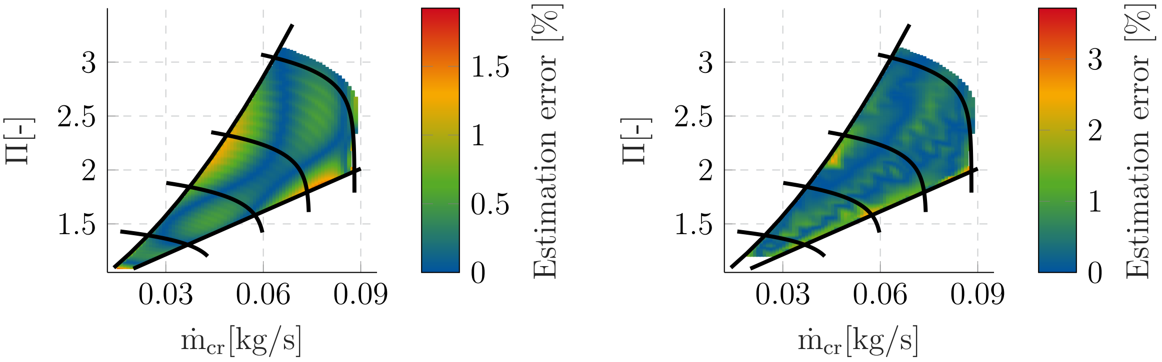

(a) Estimation error of the corrected air mass flow rate.

(b) Estimation error of the compressor efficiency.

Fig. 3.4

The compressor efficiency $\eta_{\mathrm{cp}}\left(\Pi, \dot{m}_{\mathrm{cp}}\right)$ is described by a lookup table, which is determined experimentally. For the controller design, the lookup table is approximated by a polynomial of order 2 in the pressure ratio Π and corrected air mass flow rate $\dot{m}_{\mathrm{cr}}$. Because the equations (3.16) and (3.17) have the compressor efficiency η_{cp} in the denominator, the inverse of η_{cp} is approximated:

$$\frac{1}{\eta_{\mathrm{cp}}} = f\left(\dot{m}_{\mathrm{cr}}, \Pi\right) \approx \sum_{i=1}^{2} \sum_{j=1}^{2} b_{ij} \cdot \dot{m}_{\mathrm{cr}}^{i} \cdot \Pi^{j} \tag{3.19}$$

The parameters b_{ij} are also fitted by least squares with the Curve Fitting Toolbox in MATLAB®. In Figure 3.4b, the estimation error between the lookup table containing 212 data points with linear interpolation and the polynomial approximation is given. In most cases, the error lies below 2 %. However, at the choke boundary for medium mass flow rates, the error has its peak above 3 %. It should be considered that the given look-up table is not dense and is based on experimental data. Therefore, the approximation gives reasonable results.

The surge and choke boundaries are approximated according to the estimated compressor map by *Pukrushpan* [9]. While the choke boundary can be approximated by a line equation as given in (3.20), the surge boundary gives a better fit if it is approximated by a quadratic polynomial as given in (3.21).

$$\Pi = 13.125\dot{m}_{\mathrm{cr}} + 0.82 \qquad \text{(choke boundary)} \tag{3.20}$$

$$\Pi = 278.69\dot{m}_{\mathrm{cr}}^{2} + 17.88\dot{m}_{\mathrm{cp}} + 0.79 \qquad \text{(surge boundary)} \tag{3.21}$$

The electrical compressor power consumption P_{cm} is defined by (3.22) and depends on the motor voltage U_{cm} and the rotational speed ω_{cp}.

$$P_{\mathrm{cm}} = U_{\mathrm{cm}} \cdot I_{\mathrm{cm}} = \frac{U_{\mathrm{cm}}}{R_{\mathrm{cm}}} \left(U_{\mathrm{cm}} - k_{\mathrm{T}} \omega_{\mathrm{cp}} \right) \tag{3.22}$$

Manifold Models

The air supply path can be divided into the inlet manifold, the cathode manifold and the outlet manifold (compare Figure 3.2). All the manifolds follow the same principles given by (3.23),(3.24) and (3.25). They are explained first using generalized variables and are subsequently applied to the three manifolds introducing different simplifications.

The mass conservation principle is given in (3.23). $\frac{dm}{dt}$ is the change of mass in the considered volume, while $\dot{m}_{\mathrm{in}}$ is the air mass flow rate into and $\dot{m}_{\mathrm{out}}$ the air mass flow rate out of the considered volume.

$$\frac{dm}{dt} = \dot{m}_{\mathrm{in}} - \dot{m}_{\mathrm{out}} \tag{3.23}$$

The pressure change $\frac{dp}{dt}$ can be derived from the ideal gas law, energy conservation and thermodynamic air properties (3.24). M_{a} is the molar mass of air, V is the manifold volume, T_{in} is the inlet air temperature and T is the temperature inside the manifold.

$$\frac{dp}{dt} = \frac{\gamma R_{\mathrm{u}}}{M_{\mathrm{a}} V} \left(\dot{m}_{\mathrm{in}} T_{\mathrm{in}} - \dot{m}_{\mathrm{out}} T \right) \tag{3.24}$$

The air mass flow rate $\dot{m}$ between two manifolds and at the outlet of the fuel cell is determined by the nonlinear nozzle equation (3.25) whereby (3.25a) gives the air mass flow rate $\dot{m}$ below and (3.25b) the choked air mass flow rate $\dot{m}_{\mathrm{choked}}$ above the critical pressure ratio [9]. A sketch of a nozzle with the corresponding parameters can be found in Figure 3.5a. C_{D} is the discharge coefficient, $A_{\mathrm{t,eff}}$ is the effective opening area, p_1 and T_1 are the upstream pressure and temperature whereas p_2 is the downstream pressure. The critical pressure ratio $\frac{p_2}{p_1}$ for air is at 0.528 and describes the point at which the air mass flow rate $\dot{m}$ reaches sonic speed. In Figure 3.5b, the resulting air mass flow rate $\dot{m}$ normalized by the choked flow rate $\dot{m}_{\mathrm{choked}}$ is presented. As the pressure ratio $\frac{p_2}{p_1}$ increases, the air mass flow rate $\dot{m}$ increases until the choked air mass flow rate $\dot{m}_{\mathrm{choked}}$ is reached.

$$\dot{m} = \frac{C_{\mathrm{d}} A_{\mathrm{t,eff}} p_1}{\sqrt{R_{\mathrm{u}} T_1}} \left(\frac{p_2}{p_1} \right)^{\frac{1}{\gamma}} \sqrt{\frac{2\gamma}{\gamma - 1} \left[1 - \left(\frac{p_2}{p_1} \right)^{\frac{\gamma - 1}{\gamma}} \right]} \quad \text{for} \quad \frac{p_2}{p_1} \geq \left(\frac{2}{\gamma + 1} \right)^{\frac{\gamma}{\gamma - 1}} \tag{3.25a}$$

$$\dot{m}_{\mathrm{choked}} = \frac{C_{\mathrm{D}} A_{\mathrm{t,eff}} p_1}{\sqrt{R_{\mathrm{u}} T_1}} \sqrt{\gamma} \left(\frac{2}{\gamma + 1} \right)^{\frac{\gamma + 1}{2(\gamma - 1)}} \quad \text{for} \quad \frac{p_2}{p_1} \leq \left(\frac{2}{\gamma + 1} \right)^{\frac{\gamma}{\gamma - 1}} \tag{3.25b}$$

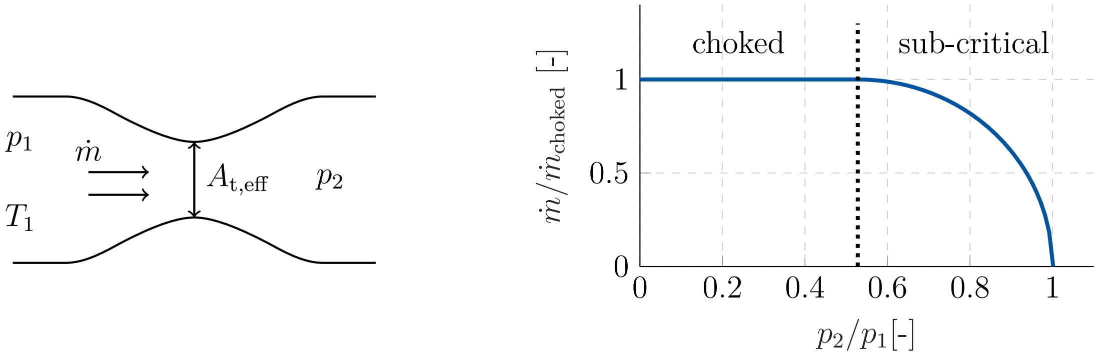

(a) Nozzle sketch. **(b)** Nozzle equation.

Fig. 3.5: Illustration of the nonlinear nozzle equation.

The **Inlet Manifold (IM)** represents the lumped volume of the pipes and components between the compressor and the fuel cell stack. The inlet air is coming from the compressor. Hence, the temperature $T_{\mathrm{cp,out}}$ differs considerably from the air temperature inside the manifold T_{im} which is given by (3.26).

$$T_{\mathrm{im}} = \frac{M_{\mathrm{a}} p_{\mathrm{im}} V_{\mathrm{im}}}{m_{\mathrm{im}} R_{\mathrm{u}}} \tag{3.26}$$

The differential equations of the two states m_{im} and p_{im} (compare Figure 3.2) can be described based on (3.23) and (3.24) by (3.27) and (3.28).

$$\frac{dm_{\mathrm{im}}}{dt} = \dot{m}_{\mathrm{cp}} - \dot{m}_{\mathrm{cat,in}} \tag{3.27}$$

$$\frac{dp_{\mathrm{im}}}{dt} = \frac{R_{\mathrm{u}}\gamma}{V_{\mathrm{im}} M_{\mathrm{a}}} \left(\dot{m}_{\mathrm{cp}} T_{\mathrm{cp}} - \dot{m}_{\mathrm{in}} T_{\mathrm{im}}\right) \tag{3.28}$$

The flow into the cathode $\dot{m}_{\mathrm{in}}$ is derived from the nozzle equation (3.25). Because the pressure drop from the inlet manifold to the cathode manifold is small, the nonlinear equation can be linearized by (3.29). $k_{\mathrm{cat,in}}$ is the linearized flow constant.

$$\dot{m}_{\mathrm{in}} = k_{\mathrm{cat,in}} \left(p_{\mathrm{im}} - p_{\mathrm{cat}}\right) \tag{3.29}$$

The **Cathode Manifold (Cat)** represents the lumped volume of the air path through the fuel cell stack. Before the air mass flow rate $\dot{m}_{\mathrm{cat,in}}$ enters the cathode manifold, it is cooled down to the stack temperature T_{st} by an isobaric air cooler (compare Figure 2.3) leading to an isothermic relation. Consequently, the differential equation of the cathode pressure p_{cat} is described by (3.30).

$$\frac{dp_{\mathrm{cat}}}{dt} = \frac{R_{\mathrm{u}} T_{\mathrm{st}}}{M_{\mathrm{a}} V_{\mathrm{cat}}} \left(\dot{m}_{\mathrm{cat,in}} - \dot{m}_{\mathrm{react}} - \dot{m}_{\mathrm{cat,out}}\right) \tag{3.30}$$

According to the electrochemical equations (3.5) and (3.7), the partial pressure of oxygen p_{O_2} needs to be known for the prediction model of the controller. Thus, p_{O_2} is introduced as an additional state. The differential equation as given in (3.31) can be derived from (3.24) whereby $\dot{n}$ describes the oxygen molar flow rate.

$$\frac{dp_{O_2}}{dt} = \frac{R_\mathrm{u} T_\mathrm{st}}{V_\mathrm{cat}} \left(\dot{n}_\mathrm{cat,in} - \dot{n}_\mathrm{react} - \dot{n}_\mathrm{cat,out}\right) \tag{3.31}$$

$\dot{n}_\mathrm{cat,in}$ is the oxygen molar flow rate into the cathode manifold and is described by (3.32). It is assumed that the mole fraction of oxygen in the inlet air $X_{O_2,\mathrm{in}}$ is 21 %.

$$\dot{n}_\mathrm{cat,in} = \frac{X_{O_2,\mathrm{in}} \dot{m}_\mathrm{cat,in}}{M_\mathrm{a}} \tag{3.32}$$

The oxygen molar flow rate $\dot{n}_\mathrm{react}$ reacts at the electrode in the reduction process to water and is described by (3.33). The amount is proportional to the stack current I_st by the motor torque constant k_T. M_O is the molar mass of oxygen. $n_\mathrm{fc,cell}$ is the number of cells of the fuel cell stack and F is the Faraday constant.

$$\dot{m}_\mathrm{react} = 2 M_O \dot{n}_\mathrm{react} = \frac{2 M_O n_\mathrm{fc,cell} I_\mathrm{st}}{4F} \tag{3.33}$$

$\dot{n}_\mathrm{cat,out}$ is the oxygen molar flow rate out of the cathode. Since part of the oxygen reacted, the partial fraction of oxygen at the outlet $X_{O_2,\mathrm{out}}$ is lower as given in (3.34). $\dot{n}_\mathrm{cat,out}$ is determined analog to the inlet oxygen molar flow rate $\dot{n}_\mathrm{cat,in}$ by (3.35).

$$X_{O_2,\mathrm{out}} = \frac{p_{O_2}}{p_\mathrm{cat}} \tag{3.34}$$

$$\dot{n}_\mathrm{cat,out} = \frac{X_{O_2,\mathrm{out}} \dot{m}_\mathrm{cat,out}}{M_\mathrm{a}} \tag{3.35}$$

$$\tag{3.36}$$

The outlet air mass flow rate of the cathode $\dot{m}_\mathrm{out}$ as given in (3.37) is derived from the linearized nozzle equation in (3.29). $k_\mathrm{cat,out}$ is the linearized flow constant at the cathode output.

$$\dot{m}_{cat,out} = k_\mathrm{cat,out} \left(p_\mathrm{cat} - p_\mathrm{om}\right) \tag{3.37}$$

The **Outlet Manifold (OM)** lumps together all volumes between the fuel cell stack and the back pressure valve. The temperature in the outlet manifold is similar to the stack temperature T_st. Therefore, the differential equation of the pressure in the outlet manifold p_om can be described as follows.

$$\frac{dp_\mathrm{om}}{dt} = \frac{R_\mathrm{a} T_\mathrm{st}}{V_\mathrm{om}} \left(\dot{m}_\mathrm{out} - \dot{m}_\mathrm{om}\right) \tag{3.38}$$

The outlet manifold pressure p_om can be much higher than the nominal pressure p^0 behind the outlet of the manifold. Thus, a linearization of the nozzle equation (3.25) is not sufficiently accurate. A back pressure valve is installed at the outlet. The valve can adjust the effective opening area $A_{\mathrm{t,eff}}$ of the outlet nozzle by (3.39) whereby A_{t} is the maximum opening area and h_{om} is the valve opening position.

$$A_{\mathrm{t,eff}} = A_{\mathrm{t}} h_{\mathrm{om}} \tag{3.39}$$

According to the nozzle equation in (3.25), the critical pressure in the outlet manifold p_{om} is at 1.92 bar. It is assumed that the pressure in the outlet manifold stays below or close to that pressure during operation. Thus, the air mass flow rate $\dot{m}_{\mathrm{om}}$ is described by (3.25a) and (3.39).

3.3 Battery Model

A battery can be modeled at different levels of complexity. *J. Badeda et al.* [62] gives an overview of possible modeling techniques. Within the scope of this thesis, it is adequate to describe the battery on the macro level which presents the voltage-current behavior and the change of the SOC. The model of choice for this thesis is the Shepherd model [62, 63]. The following assumptions are made:

- The battery model does not depend on the temperature.
- The battery has no memory effect or self-discharge.
- The only considered dynamic of the battery is the SOC.
- The discharge behavior equals the charge behavior.

The equivalent circuit diagram of an elementary cell is presented in Figure 3.6. It consists of an internal resistance R_{i} with the voltage drop U_{R} and a voltage source describing the open circuit voltage (OCV) U_{ocv}. The battery current I_{Bat} is the actuating variable of the battery $\mathbf{u}_{\mathrm{bat}}$ and SOC is the battery state $\mathbf{x}_{\mathrm{bat}}$.

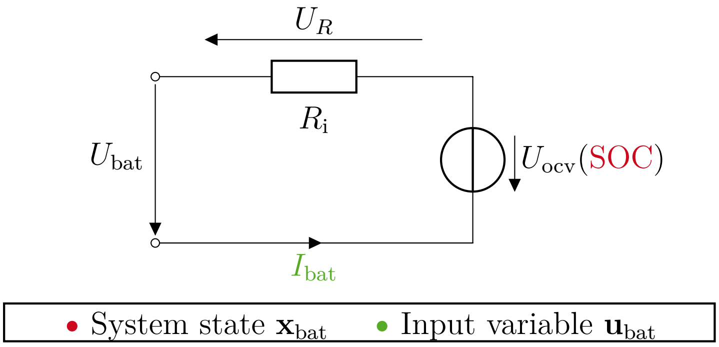

Fig. 3.6: Equivalent circuit diagram of the battery model [33].

The battery voltage U_{bat} is described by (3.40). The OCV U_{ocv} is separated into three parts by (3.41). E_0 is the constant potential, U_{pol} is the polarization voltage and U_{exp} is the exponential voltage. K is the polarization voltage constant, Q is the battery capacity, A is the exponential zone amplitude and B is the inverse of the exponential zone time constant.

$$U_{\text{bat}} = U_{\text{ocv}} - \underbrace{R_{\text{i}} I_{\text{Bat}}}_{U_{\text{R}}} \tag{3.40}$$

$$U_{\text{ocv}} = E_0 - \underbrace{\frac{K}{\text{SOC}}}_{U_{\text{pol}}} + \underbrace{A \cdot \exp\left(-Q \cdot \text{SOC} \cdot B\right)}_{U_{\text{exp}}} \tag{3.41}$$

The dependency of the OCV on the SOC is presented in Figure 3.7. For reasons of battery lifetime, the SOC range of a battery is usually limited to SOC_{min} and SOC_{max}. In this thesis, the valid battery SOC ranges between 40 % and 80 %.

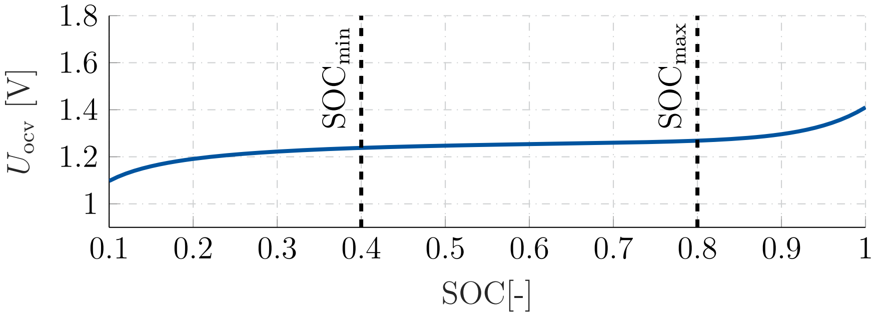

Fig. 3.7: Open circuit voltage of the battery in dependence of the battery SOC.

The chosen vehicle configuration utilizes a nickel metal hydride battery (NiMH) with a storage capacity of 6.5 A h. The parameters, which are determined experimentally, are taken from *O. Tremblay et al.* [62] and can be found in Table A.1.

The current I_{Bat} and battery power P_{bat} are defined as positive for discharging and negative for charging corresponding to Figure 3.6. The net power of the battery at the output terminal of the battery $P_{\text{bat,net}}$ is defined by (3.42). The elementary cells are connected in series of n_{packs} packs each consisting of $n_{\text{bat,cell}}$ cells.

$$P_{\text{bat,net}} = n_{\text{packs}} n_{\text{bat,cell}} U_{\text{Bat}} I_{\text{bat}} = n_{\text{packs}} n_{\text{bat,cell}} \left(U_{\text{ocv}} - U_{\text{R}}\right) I_{\text{bat}} \tag{3.42}$$

The battery power P_{bat} that is stored or drawn from the battery as given in (3.43) depends on the net power of the battery $P_{\text{bat,net}}$ and the internal power loss $P_{bat,loss}$ across the internal resistance R_{i}.

$$P_{\text{bat}} = n_{\text{packs}} n_{\text{bat,cell}} U_{\text{ocv}} I_{\text{bat}} = P_{\text{bat,net}} + \underbrace{U_{\text{R}} I_{\text{bat}}}_{P_{\text{bat,loss}}} \tag{3.43}$$

The differential equation of the SOC can either be described dependently on the battery current I_{bat} or on the net power $P_{\text{bat,net}}$ [55].

$$\frac{d\text{SOC}}{dt} = -\frac{I_{\text{Bat}}}{Q} = -\frac{1}{2R_{\text{i}}Q}\sqrt{U_{\text{ocv}}^2 - \frac{4R_{\text{i}}P_{\text{bat,net}}}{n_{\text{packs}}n_{\text{bat,cell}}}} \tag{3.44}$$

3.4 DC/DC Converter Model

The DC/DC converters are described by lookup tables on the power level in the plant model. The data is based on measurements from *Füting* [64]. The curve is approximated with a polynomial of second order as given in (3.45). The curve is described by relative power values which is the actual power divided by its expected maximum value. $P_{\text{rel,bus}}$ is the relative power at the output of the DC-DC converters. $P_{\text{rel,net}}$ is related to the battery output power $P_{\text{bat,net}}$ or fuel cell system output power P_{fcs} respectively. The resulting converter efficiency η_{DC} defined by (3.46) is presented in Figure 3.8. For lower power values, the approximation is not accurate. The reason is that the origin is included as an additional measured data point to decrease the offset for zero power. Since the power values are low for the inaccurate estimation part, the absolute estimation error is sufficiently low.

$$P_{\text{rel,bus}} = \sum_{i=1}^{2} a_i P_{\text{rel,net}}^i \tag{3.45}$$

$$\eta_{DC} = \frac{P_{\text{rel,bus}}}{P_{\text{rel,net}}} \tag{3.46}$$

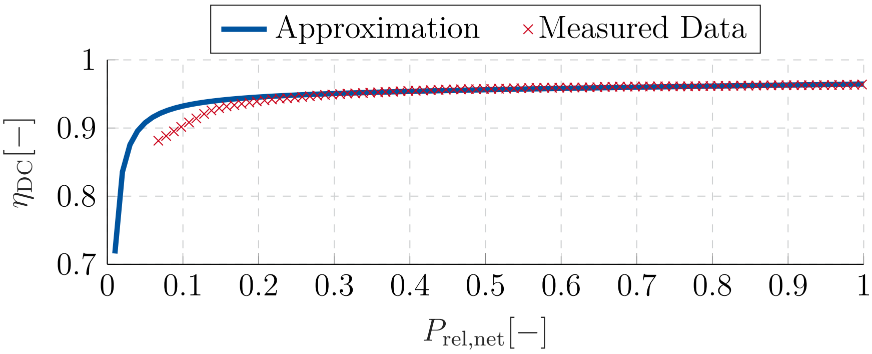

Fig. 3.8: Estimated efficiency curve of the DC/DC converter.

Since the battery has a bidirectional power flow, the DC-DC converter needs to be bidirectional as well. Therefore, the polynomial in (3.45) is utilized for both directions leading to a non-smooth transition in zero. The two polynomials are faded over by a sigmoid function in (3.47). The steepness factor s determines the duration of the fade-over. With increasing steepness, the approximation error $P_{\mathrm{rel,err}}$ decreases as illustrated by Figure 3.9. If the steepness factor s is too high, the optimization problem has large gradients around zero. Thus, a trade-off has to be made. Good results can be achieved for $s = 100$ which leads to a maximum error below 0.05 % compared to the polynomial approximation.

$$P_{\mathrm{rel,bus}} = \frac{P^{+}_{\mathrm{rel,bus}}}{1 + \exp\left(-sP_{\mathrm{rel,net}}\right)} - \frac{P^{-}_{\mathrm{rel,bus}}}{1 + \exp\left(sP_{\mathrm{rel,net}}\right)} \tag{3.47}$$

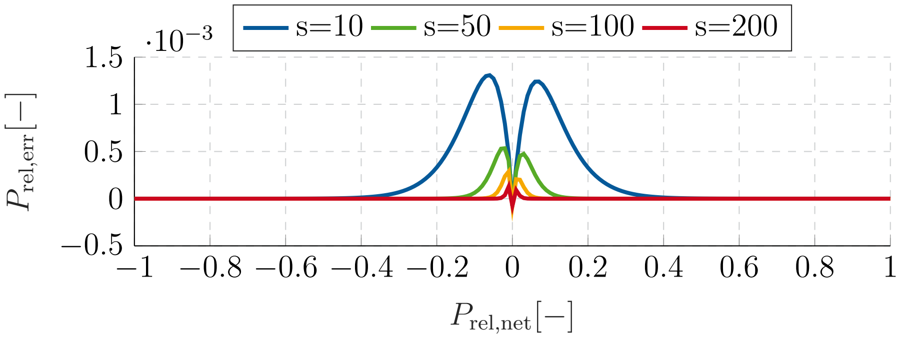

Fig. 3.9: Estimation error dependent on the steepness s of the battery DC/DC converter.

4 Hierarchical Control Design

In this chapter, the hierarchical control design for the power management of the FCHV is presented. In Section 4.1, an overview of the control structure is given summarizing the goals of each control level. In Section 4.2, the control design of the low-level control (LLC) is explained. In order to ensure an efficient operation of the fuel cell system, the optimal operating point is determined by an intermediate-level control (ILC) which is described in Section 4.3. Subsequently, the high-level control (HLC) determining the optimal power split between the fuel cell system and the battery is presented in Section 4.4.

4.1 Overview of Hierarchical Control Structure

The power management of the FCHV has to meet the following central objectives:

1. **Dynamic power delivery**: The delivered power P_{del} should follow the demanded power P_{dem} with minimal lag and delay.

2. **Hydrogen consumption minimization**: In automotive applications, hydrogen consumption minimization is equivalent to overall efficiency maximization. Therefore, the components should work in efficient operating ranges.

3. **Charge sustainability**: The battery SOC at the end of a driving cycle should be close to the middle of the valid SOC range.

4. **Compliance with system constraints**: All components of the system have to work within their operating ranges.

The central objectives of the hierarchical control will be referred to when the corresponding controllers are introduced.

The resulting control problem for the power management of the FCHV is predestinated for the use of an MPC. First of all, the dynamic model of the propulsion system is inherently nonlinear. Secondly, the problem is restricted by several constraints of the compressor and the battery SOC. Moreover, the FCHV is a coupled MIMO system which is illustrated by the RGA in Appendix A.3. All the properties can be handled by the MPC approach. The nonlinearity can be taken into account by choosing a nonlinear prediction model, constraints can explicitly be considered in the optimization problem and MIMO systems are inherently decoupled by the MPC. Furthermore, the control approach can utilize predictive information in order to act on upcoming events rather than reacting on control errors.

In Figure 4.1, the dominant time constants of the FCHV are presented [9]. They vary between $\mathcal{O}(10^2\,\mathrm{s})$ and $\mathcal{O}(10^{-19}\,\mathrm{s})$. The slowest time constant is caused by the stack temperature T_{st} which influences the efficiency of the fuel cell system. The time constant for the power demand prediction is of order $\mathcal{O}(10^1\,\mathrm{s})$ because it has been shown that a prediction of at least 10 s is recommended to achieve almost optimal control [65]. Additionally, the time constant of the battery SOC varies between $\mathcal{O}(1\,\mathrm{s})$ and $\mathcal{O}(10^1\,\mathrm{s})$ which means that the SOC can be changed considerably within that time. The time constant of the air supply which is dominated by the motor inertia J_{cm} is of order $\mathcal{O}(10^{-1}\,\mathrm{s})$. The hydrogen is supplied from a high pressure tank. Therefore, it has a time constant of order $\mathcal{O}(10^{-2}\,\mathrm{s})$. The fastest time constant of $\mathcal{O}(10^{-19}\,\mathrm{s})$ is caused by the electrochemistry of the battery and the fuel cell.

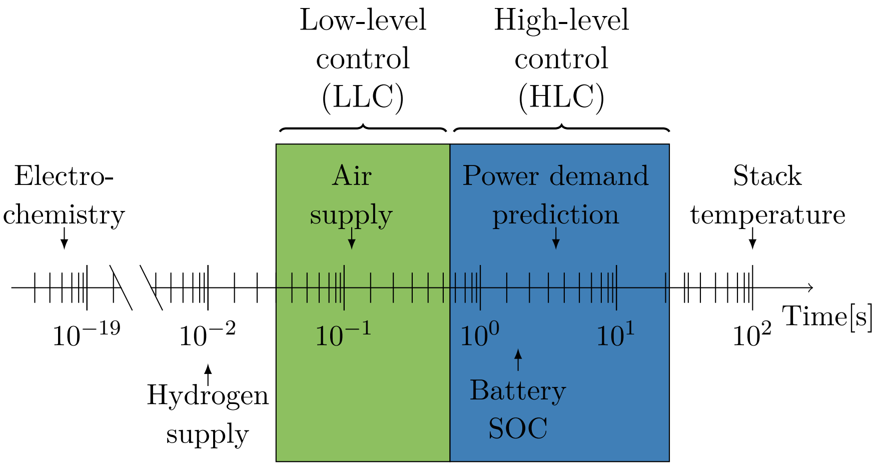

Fig. 4.1: Dominant time constants of the fuel cell hybrid vehicle [9].

In order to handle the varying time constants of an FCHV, hierarchical control approaches have been proposed by *Shiqi et al.* [39]. In this thesis, a hierarchical control structure is used and justified by the dominant time constants in Figure 4.1. The HLC (in blue) captures the time constants from $\mathcal{O}(1\,\mathrm{s})$ until $\mathcal{O}(10^1\,\mathrm{s})$. It considers the time constants of the battery SOC and the power demand prediction. The LLC (in green) captures the time constants around $\mathcal{O}(10^{-1}\,\mathrm{s})$. In order to prevent fuel cell starvation, the power delivery of the fuel cell system is dynamically limited by the air supply. Thus, power and air supply control are handled by the LLC.

The time constants of the hydrogen supply and the stack temperature T_{st} are not considered by the power management. The time constant of the stack temperature T_{st} is large. Furthermore, T_{st} is nearly constant at 80 °C after a start-up phase [9]. Therefore, a PI-controller is utilized for the temperature control. The dominant time constant of the hydrogen supply is smaller. Thus, the anode pressure p_{an} is regulated by a PI-controller. Thereby, p_{an} follows the cathode pressure p_{cat}.

Figure 4.2 presents an overview of the hierarchical control structure from the implementation point of view. It illustrates the different levels and the interconnections between them. The states of the fuel cell system $\mathbf{x}_{\mathrm{fcs}}$ and the battery $\mathbf{x}_{\mathrm{bat}}$ were presented in Chapter 3.

The parameter vector p_{fcs} consists of the stack temperature T_{st}.

The **Component Level** consists of the battery and the fuel cell system as well as the DC/DC converters. Actuating variables of the fuel cell system are the stack current I_{st}, the compressor motor voltage U_{cm} and the back pressure valve opening position h_{om}. Actuating variables of the battery is the current I_{bat}. The components are connected by DC/DC converters which include conversion losses. The output powers $P_{\mathrm{fcs,bus}}$ and $P_{\mathrm{bat,bus}}$ sum up to the delivered power P_{del}.

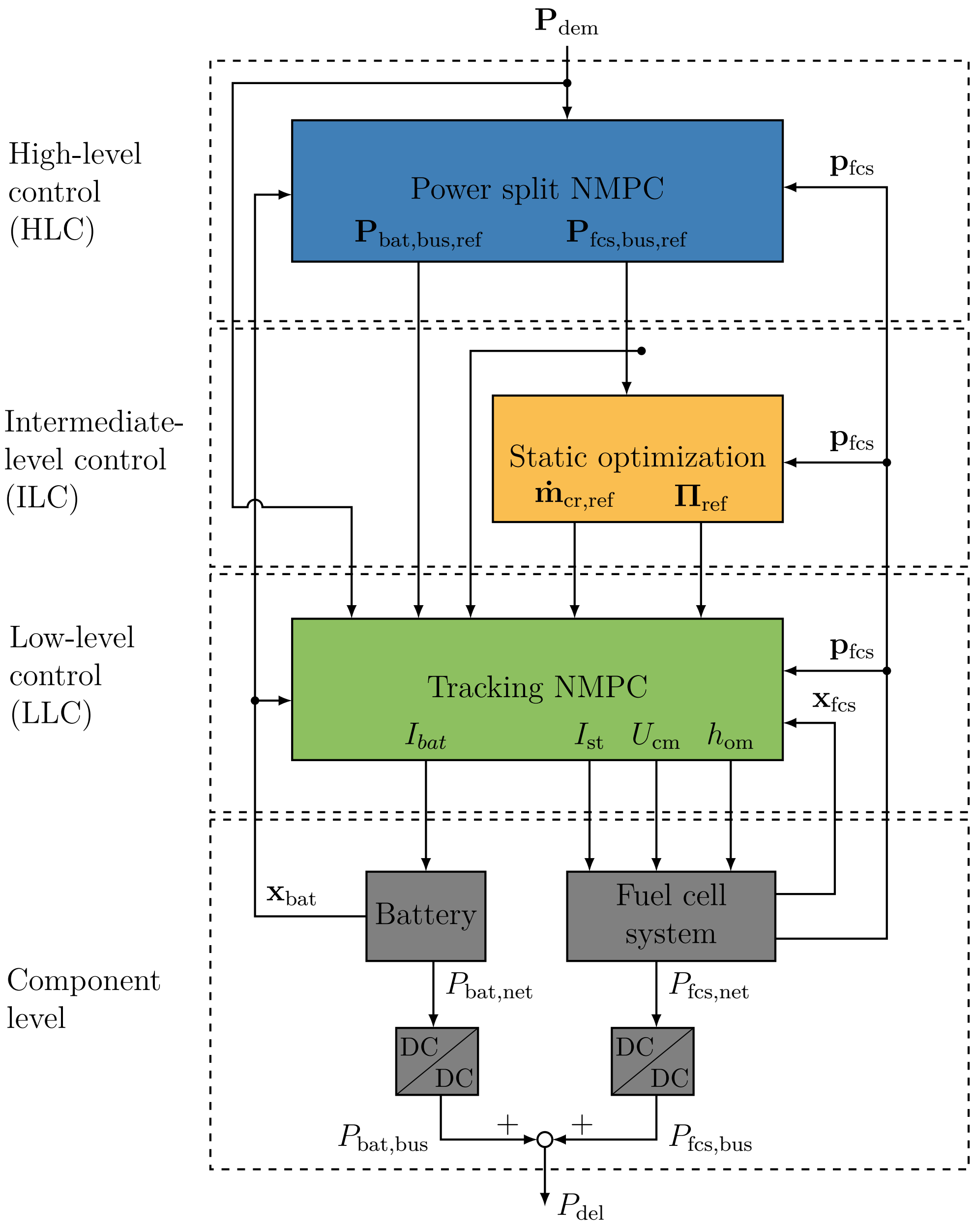

Fig. 4.2: Overview of the hierarchical control structure.

The **low-level control (LLC)** consists of an nonlinear model predictive control (NMPC) (in green). It is responsible for the dynamic power delivery (Objective 1) and compliance with system constraints (Objective 4). The NMPC tracks the references received from the higher levels. A major challenge for the power management of the FCHV is the dynamic power delivery of the fuel cell system. In literature, the limited dynamics are often considered by introducing explicit limitations on the fuel cell system dynamics in the HLC [66, 67]. However, with the use of predictive information in the LLC, the operating point of the compressor can be adjusted before the power step occurs and thus increasing the performance. Moreover, the controller can utilize the battery for a dynamic power split that deviates from the received references in case the power reference of the fuel cell system cannot be followed instantaneously. In Section 4.2 an in-depth view of the LLC design is presented. Parameters considering the LLC are labeled with the superscript l.

For the **intermediate-level control (ILC)**, a static optimization (in orange) is utilized which determines the optimal operating point of the air supply. Thereby, a trade-off between dynamic power delivery (Objective 1) and hydrogen consumption minimization (Objective 2) has to be made. Moreover, operating constraints of the compressor have to be considered (Objective 4). Further investigation on the ILC design is presented in Section 4.3. All parameters related to the ILC are labeled with the superscript i.

The objectives of the **high-level control (HLC)** is the hydrogen consumption minimization (Objective 1) and the charge sustainability of the battery SOC (Objective 3) considering constraints of the components (Objective 4). Since the time constants handled by the controller are large, a static model of the fuel cell system is derived. The only dynamic state considered is the battery SOC. The controller determines the optimal static power split between the battery power $\mathbf{P}_{\mathrm{bat,bus,ref}}$ and the fuel cell system power $\mathbf{P}_{\mathrm{fcs,bus,ref}}$. Further details are presented in Section 4.4. Parameters considering the HLC are labeled with the superscript h.

4.2 Low-Level Control Design

In this section, the control design of the LLC is presented. The controller specific objectives of the LLC are:

1. **Dynamic power split**: The demanded power P_{dem} should be tracked by the delivered power P_{del} with minimal lag and delay. If constraints of the fuel cell system limit the response time of the fuel cell system power $P_{\mathrm{fcs,bus}}$, the controller should utilize a dynamic power split that deviates from the static power split by the HLC.

2. **Track hydrogen optimized reference points**: In order to have a similar hydrogen consumption than estimated by the HLC, the reference points for the power split ($\mathbf{P}_{\mathrm{fcs,bus,ref}}$ and $\mathbf{P}_{\mathrm{bat,bus,ref}}$) and the air supply ($\dot{\mathbf{m}}_{\mathrm{cr,ref}}$ and $\mathbf{\Pi}_{\mathrm{ref}}$) should be tracked.

3. **Compliance with constraints on a short time scale**: The short time scale constraints comprise the oxygen excess ratio λ_{O_2} and the compressor surge and choke boundaries.

4. **Avoid excessive actuator changes**: In order to achieve a smooth operation, excessive actuator changes need to be avoided.

This section is organized as follows. Section 4.2.1 explains the interaction of the LLC with the HLC. In Section 4.2.2, the prediction model is summarized based on the physical relations from Chapter 3. The cost function and its corresponding objectives are presented in Section 4.2.3. Subsequently, the system constraints are given in Section 4.2.4. Finally, the resulting optimal control problem and implementation details of the utilized toolbox GRAMPC are presented in Section 4.2.5.

4.2.1 Interaction with Intermediate- and High-Levels

The LLC receives the reference trajectories $\mathbf{y}^h_{\text{ref}}$ from the higher control levels consisting of the demanded power $\mathbf{P}_{\text{dem}}$, the fuel cell bus power $\mathbf{P}_{\text{fcs,bus,ref}}$, the battery power $\mathbf{P}_{\text{bat,bus,ref}}$, the compressor flow $\dot{\mathbf{m}}_{\text{cr,ref}}$ and the pressure ratio across the compressor $\mathbf{\Pi}_{\text{ref}}$.

$$\mathbf{y}^h_{\text{ref}} = \begin{bmatrix}\mathbf{P}_{\text{dem}} & \mathbf{P}_{\text{fcs,bus,ref}} & \mathbf{P}_{\text{bat,bus,ref}} & \dot{\mathbf{m}}_{\text{cr,ref}} & \mathbf{\Pi}_{\text{ref}}\end{bmatrix} \tag{4.1}$$

In this thesis, a reference interpolation based on sigmoid functions is proposed. The higher control levels have a sampling time T^h_{S}. The LLC executes with a shorter sampling time T^l_{S}. Therefore, the trajectories need to be interpolated. Two possibilities proposed by *Josevski* [55] are zero-order hold and linear interpolation. Sigmoid interpolation is similar to the zero-order hold approach but it increases the mathematical conditioning of the optimal control problem during a operating point change.

In Figure 4.3, a graphical representation of the sigmoid interpolation is presented for a single reference trajectory $\mathbf{y}^l_{\text{ref},j}(\cdot)$ denoted by j. The black dashed line is the zero-order hold reference $\mathbf{y}^h_{\text{ref},j}(\cdot)$ with a sampling time T^h_{S} while the blue solid line is the sigmoid interpolated reference $\mathbf{y}^l_{\text{ref},j}(\cdot)$ with a sampling time T^l_{S}. Δt represents the steepness of the sigmoid interpolation and is set to 50 ms which means that the step is completed by 66.7 % at that time. For $\Delta t \to 0$, the sigmoid interpolation converges to the zero-order hold interpolation.

The interpolation can be formulated as a multiplication with an offline calculated constant matrix $\mathbf{M}$ as given in (4.2). The complete derivation can be found in Appendix A.4.

$$\mathbf{y}^l_{\text{ref},j}(\cdot) = \mathbf{M}\mathbf{y}^h_{\text{ref},j}(\cdot) \tag{4.2}$$

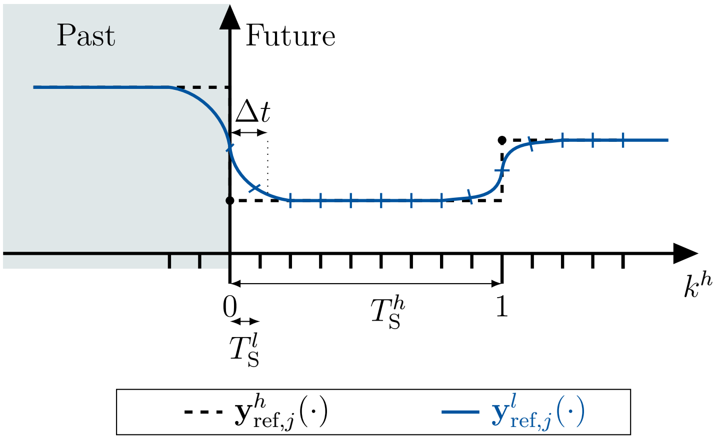

Fig. 4.3: Reference trajectory interpolation from the HLC to the LLC.

4.2.2 Low-Level Prediction Model

The prediction model is derived from the control-oriented modeling in Chapter 3. The nonlinear state-space model is presented in (4.3).

$$\dot{\mathbf{x}}^l(t) = \mathbf{f}(\mathbf{x}^l(t), \mathbf{u}^l(t), \mathbf{p}^l(t)) \tag{4.3a}$$

$$\mathbf{y}^l(t) = \mathbf{g}(\mathbf{x}^l(t), \mathbf{u}^l(t), \mathbf{p}^l(t)) \tag{4.3b}$$

Whereby, $\mathbf{u}^l$, $\mathbf{x}^l$, $\mathbf{p}^l$ and $\mathbf{y}^l$ denote the input, state, parameter and output vector respectively. $\mathbf{u}^l$ consists of the stack current I_{st}, the motor voltage U_{cm}, the back pressure valve position h_{om} and the battery current I_{bat}.

$$\mathbf{u}^l = \begin{bmatrix} I_{\text{st}} & U_{\text{cm}} & h_{\text{om}} & I_{\text{bat}} \end{bmatrix}^T \tag{4.4}$$

$\mathbf{y}^l$ comprises the delivered power P_{del}, the fuel cell power $P_{\text{fcs,bus}}$, the battery power $P_{\text{bat,bus}}$, the corrected air mass flow rate $\dot{m}_{\text{cr}}$ and the pressure ratio Π.

$$\mathbf{y}^l = \begin{bmatrix} P_{\text{del}} & P_{\text{fcs,bus}} & P_{\text{bat,bus}} & \dot{m}_{\text{cr}} & \Pi \end{bmatrix}^T \tag{4.5}$$

$\mathbf{x}^l$ consists of the cathode pressure p_{cat}, the pressure of the inlet manifold p_{im}, the pressure in the outlet manifold p_{om}, the partial oxygen pressure in the cathode p_{O_2}, the air mass in the inlet manifold m_{im} and the rotational speed of the compressor ω_{cp}.

$$\mathbf{x}^l = \mathbf{x}_{\text{fcs}} = \begin{bmatrix} p_{\text{cat}} & p_{\text{im}} & p_{\text{om}} & p_{O_2} & m_{\text{im}} & \omega_{\text{cp}} \end{bmatrix}^T \tag{4.6}$$

$\mathbf{p}^l$ comprises the stack temperature T_{st} and the battery SOC. These correspond to the states that have a large time constant (compare Figure 4.1) and can therefore be set constant for the prediction horizon N_{P}^l.

$$\mathbf{p}^l = \begin{bmatrix} \mathbf{p}_{\text{fcs}}^T & \mathbf{x}_{\text{bat}}^T \end{bmatrix}^T = \begin{bmatrix} T_{\text{st}} & \text{SOC} \end{bmatrix}^T \tag{4.7}$$

Note that full state knowledge is assumed within this thesis. Some of the above mentioned states are difficult to measure, particularly the battery SOC, the partial oxygen pressure in the cathode p_{O_2} and the air mass in the inlet manifold m_{im}. Possible technique to estimate those states are an extended Kalman filter, an unscented Kalman filter or a sequential Monte Carlo filter [68–70].

4.2.3 Low-Level Cost Function

The LLC tracks the reference points from the higher levels $\mathbf{y}^l_{\mathrm{ref}}$. Moreover excessive actuator changes are avoided. The corresponding cost function is quadratic.

$$J = \int_0^{T^l_{\mathrm{P}}} \| \left(\mathbf{y}^l - \mathbf{y}^l_{\mathrm{ref}} \right) \|^2_{\mathbf{Q}^l} + \|\dot{\mathbf{u}}^l\|^2_{\mathbf{R}^l} \mathrm{d}t \tag{4.8}$$

The weighting matrices $\mathbf{Q}^l$ and $\mathbf{R}^l$ in (4.9) are diagonal matrices and are selected constantly.

$$\mathbf{Q}^l = \begin{bmatrix} q_{P_{\mathrm{del}}} & 0 & 0 & 0 & 0 \\ 0 & q_{P_{\mathrm{fcs,bus}}} & 0 & 0 & 0 \\ 0 & 0 & q_{P_{\mathrm{bat,bus}}} & 0 & 0 \\ 0 & 0 & 0 & q_{\dot{m}_{\mathrm{cr}}} & 0 \\ 0 & 0 & 0 & 0 & q_{\Pi} \end{bmatrix}, \qquad \mathbf{R}^l = \begin{bmatrix} r_{I_{\mathrm{st}}} & 0 & 0 & 0 \\ 0 & r_{U_{\mathrm{cm}}} & 0 & 0 \\ 0 & 0 & r_{h_{\mathrm{om}}} & 0 \\ 0 & 0 & 0 & r_{I_{\mathrm{bat}}} \end{bmatrix} \tag{4.9}$$

In order to penalize the derivatives $\dot{\mathbf{u}}^l$, the prediction model has to be extended with augmented states $\tilde{\mathbf{x}}^l$ as given in (4.10) [6]. Therefore, the vector $\mathbf{u}^l$ is adjoined to the state vector $\mathbf{x}^l$ and the augmented vector $\tilde{\mathbf{u}}^l$ is the derivate vector of the input vector $\dot{\mathbf{u}}^l$.

$$\tilde{\mathbf{x}}^l = \begin{bmatrix} \mathbf{x}^l \\ \mathbf{u}^l \end{bmatrix}, \qquad \tilde{\mathbf{u}}^l = \dot{\mathbf{u}}^l, \qquad \mathbf{u}^l = \int \dot{\mathbf{u}}^l \mathrm{d}t \tag{4.10}$$

The prediction model of an MPC is affected by modeling errors. In order to achieve an offset-free control, a disturbance observer is applied (compare Section 2.2.4) which can diminish the influence of model errors caused by simplifications presented in Chapter 3. The disturbance state $\mathbf{d}$ is estimated for each output of the system $\mathbf{y}^l$ as stated by (2.24). Because it is constant over the prediction horizon, the disturbance vector is augmented to the parameter vector $\mathbf{p}^l$.

$$\tilde{\mathbf{p}}^l = \begin{bmatrix} \mathbf{p}^T_{\mathrm{fcs}} & \mathbf{x}^T_{\mathrm{bat}} & \mathbf{d}^T \end{bmatrix}^T \tag{4.11}$$

The above mentioned modifications change the nonlinear state-space model of (4.3) to (4.12). Note that in this formulation, the output $\mathbf{y}^l$ is not depended on the input $\tilde{\mathbf{u}}^l$ anymore. Thus, the direct feed through of the system is eliminated.

$$\dot{\tilde{\mathbf{x}}}^l(t) = f(\tilde{\mathbf{x}}^l(t), \tilde{\mathbf{u}}^l(t), \tilde{\mathbf{p}}^l(t)) \tag{4.12a}$$

$$\mathbf{y}^l(t) = g(\tilde{\mathbf{x}}^l(t), \tilde{\mathbf{p}}^l(t)) \tag{4.12b}$$

4.2.4 Low-Level System Constraints

Another objective of the LLC is to meet the system constraints. The input constraints are summarized in (4.13). They limit the derivatives of the system inputs. Within this thesis the input constraints are large such that they always stay within their boundaries. For further investigation, especially the maximum rate of change of the valve opening position Δh_{om} can be taken into account [46].

$$\tilde{\mathbf{u}}^l \in \mathcal{U} \widehat{=} \left\{ \begin{bmatrix} \Delta I_{\mathrm{st}} \\ \Delta U_{\mathrm{cm}} \\ \Delta h_{\mathrm{om}} \\ \Delta I_{\mathrm{bat}} \end{bmatrix} \in \mathbb{R}^4 \;\middle|\; \begin{matrix} \Delta I_{\mathrm{st,min}} \leq \Delta I_{\mathrm{st}} \leq \Delta I_{\mathrm{st,max}} \\ \Delta U_{\mathrm{cp,min}} \leq \Delta U_{\mathrm{cm}} \leq \Delta U_{\mathrm{cp,max}} \\ \Delta h_{\mathrm{om,min}} \leq \Delta h_{\mathrm{om}} \leq \Delta h_{\mathrm{OM,max}} \\ \Delta I_{\mathrm{bat,min}} \leq \Delta I_{\mathrm{bat}} \leq \Delta I_{\mathrm{bat,max}} \end{matrix} \right\} \tag{4.13}$$

The state constraints $\mathbf{h}^l$ of the MPC are presented in (4.14). A minimum oxygen excess ratio $\lambda^l_{O_2,\mathrm{min}}$ has to be satisfied in order to prevent the fuel cell from starvation. Moreover, the LLC has to comply with the choke and surge boundaries of the compressor.

It is also recommended to constrain the absolute inputs $\mathbf{u}^l$ of the prediction model. However, compared to the input constraints in (4.13), state constraints $\mathbf{h}^l$ are computationally expensive to evaluate and should only include necessary constraints. Most input constraints are already met by the higher levels. Nonetheless, a minimal stack current $I_{\mathrm{st,min}}$ has to be assured and is included in the state constraints.

$$0 \geq \mathbf{h}^l(\tilde{\mathbf{x}}(t)) = \begin{bmatrix} \lambda^l_{O_2,\mathrm{min}} - \lambda_{O_2} \\ 13.13\dot{m}_{cr} + 0.82 - \Pi \\ \Pi - 278.69\dot{m}_{cr}^2 + 17.88\dot{m}_{cr} + 0.79 \\ I_{\mathrm{st,min}} - I_{\mathrm{st}} \end{bmatrix} \quad \begin{matrix} \text{(Oxygen excess ratio (2.3))} \\ \text{(Choke boundary (3.20))} \\ \text{(Surge boundary(3.21))} \\ \text{(Minimal stack current)} \end{matrix} \tag{4.14}$$

4.2.5 Low-Level Optimal Control Problem

In (4.15), the resulting nonlinear optimal control problem for the LLC is given. It corresponds to the optimal control problem formulation as stated in (2.7).

$$\begin{aligned} \min_{\tilde{\mathbf{u}}^l} \quad & \text{Cost function (4.8)} && \text{(4.15a)} \\ \text{s.t.} \quad & \text{System dynamics (4.3)} && \text{(4.15b)} \\ & \text{Input constraints (4.13)} && \text{(4.15c)} \\ & \text{state constraints (4.14)} && \text{(4.15d)} \end{aligned}$$

The optimal control problem is solved with the toolbox GRAMPC [21]. It indicates a time and memory efficient implementation on embedded hardware and achieves comparable results to other nonlinear MPC toolkits such as ACADO [21]. Subsequently, a few implementation specifics are presented.

Integration scheme: A careful choice for the solution of the optimal control problem is the integration scheme. As indicated in Appendix A.3, the system has eigenvalues over a wide range indicating a stiff system. In general, integration schemes with a large stability region perform better on those kind of problems [29]. Therefore, the integration schemes Rodas and Ruku45 seem suitable choices within the toolbox GRAMPC. They have higher computational costs but they can handle a larger step size for the given problem. Despite the intuitive choice, simulation results showed best performance for the Heun's integration method [29]. It can handle the best combination of step size and computational cost. Therefore, Heun's integration method is chosen for the LLC.

Computation of derivatives: In order to solve the optimization problem, GRAMPC solves the PMP conditions as given in (2.15). Therefore, the derivatives of the state-space model $\mathbf{f}$, the state constraints $\mathbf{h}^l$ and the cost function J with regards to the states $\tilde{\mathbf{x}}^l$ and inputs $\tilde{\mathbf{u}}^l$ need to be provided. This can either be done symbolically or by algorithmic differentiation [71]. Symbolic differentiation is more intuitive but it scales badly for large systems. Consequently, algorithmic differentiation is applied utilizing the toolbox CasADI to deliver the corresponding functions [72]. The output function of CasADI is compiled as C-Code and integrated into GRAMPC.

Scaling: The states of the system have different orders of magnitude. The pressure values are of order $\mathcal{O}(10^5)$, while the magnitude of the inlet manifold mass is of order $\mathcal{O}(10^{-1})$. Because the augmented Lagrangian method is scale variant, the system needs to be scaled. The states and inputs to the system are rated by their maximum expectable values such that all variables vary between -1 and 1. The scaling is done offline and not by the built-in functionality of GRAMPC in order to decrease the computational cost [21, p.43]. The scaling variables of the controller states $\tilde{\mathbf{x}}^l$ can be found in Table 4.1. Furthermore, the controller inputs $\tilde{\mathbf{u}}^l$ need to be scaled. The corresponding scaling values are given in Table 4.2.

Tab. 4.1: Scaling parameters of the states.

	p_{cat}	p_{im}	p_{om}	p_{O_2}	m_{im}	ω_{cp}	I_{st}	U_{cm}	h_{om}	I_{bat}
$f_{\text{sca},i}$	$3 \cdot 10^5$	$3 \cdot 10^5$	$3 \cdot 10^5$	$1 \cdot 10^5$	0.05	$1 \cdot 10^3$	450	230	1	400

Tab. 4.2: Scaling parameters of the inputs.

	ΔI_{st}	ΔU_{cm}	Δh_{om}	ΔI_{bat}
$f_{\text{sca},i}$	450	230	5	400

State clipping: Augmented Lagrangian is a penalty method which may violate the inequality constraints $\mathbf{h}^l$ and may not always search for solutions in the feasible regions. This has the advantage that the problem is not as sensitive to infeasible initial solutions as other approaches are (e.g. barrier methods). A disadvantage occurs when the problem formulation is not mathematically well-defined outside the feasible region. This is the case for the activation loss of the fuel cell (3.7). In this case the logarithm of the stack current I_{st} is calculated and leads to a discontinuous solution at zero. Because GRAMPC has no functionality to catch these cases, a workaround is implemented. The stack current I_{st} is clipped to a small threshold by (4.16) in the optimal control problem formulation in GRAMPC.

$$I_{\mathrm{st}} = \begin{cases} I_{\mathrm{st}}, & \text{if} \quad I_{\mathrm{st}} > \epsilon_{I_{\mathrm{st}}} \\ \epsilon_{I_{\mathrm{st}}}, & \text{else} \end{cases} \tag{4.16}$$

Penalty parameter choice: The penalty method also leads to the necessity of carefully tuning the penalty parameters. For MPC applications where only a few iterations are utilized, the minimum penalty c_{min} needs to be carefully tuned in order to find a good trade-off between compliance with constraints and convergence speed.

The parameters for the LLC including weights, constraints and MPC settings are given in Table A.7. The control horizon N_{C}^{l} of 80 steps and 4 control inputs $\tilde{\mathbf{u}}^{l}$ lead to an optimization problem with 320 optimization variables. The weights are chosen such that the delivered power P_{del} gets the highest priority in order to ensure a dynamic power delivery.

4.3 Intermediate-Level Control Design

In this section, the control design of the ILC is explained which optimizes the operating point of air supply. Other than the HLC and LLC, the ILC is a static optimization. The control specific objectives can be summarized as follows:

1. **Hydrogen consumption minimization**: The operating point of the air supply should be determined such that the fuel cell system efficiency is maximized and the hydrogen consumption minimized.

2. **Robustness towards uncertain power demand**: The operating point of the air supply influences the robustness towards uncertain power demands. This is essential to ensure a dynamic power delivery. It will be shown that there is a trade-off between robustness and hydrogen consumption minimization.

3. **Compliance with steady-state constraints**: The optimization should comply with constraints of the air supply in terms of the surge and choke boundaries of the compressor. Moreover, fuel cell starvation must be avoided in terms of a minimum oxygen excess ratio λ_{O_2}.

4.3.1 Steady-State Fuel Cell System

The steady-state model of the fuel cell system can be described by setting the state-space model to zero as stated by (4.17). The model is parameterized by the states $\mathbf{x}^i$, by the actuating variables $\mathbf{u}^i$ and by the parameters $\mathbf{p}^i$.

$$\dot{\mathbf{x}}^i = f(\mathbf{x}^i, \mathbf{u}^i, \mathbf{p}^i) = 0 \tag{4.17}$$

$$\mathbf{x}^i = \mathbf{x}_{\text{fcs}} = \begin{bmatrix} p_{\text{cat}} & p_{\text{im}} & p_{\text{om}} & p_{O_2} & m_{\text{im}} & \omega_{\text{cp}} \end{bmatrix}^T \tag{4.18}$$

$$\mathbf{u}^i = \begin{bmatrix} I_{\text{st}} & U_{\text{cm}} & h_{\text{om}} \end{bmatrix}^T \tag{4.19}$$

$$\mathbf{p}^i = \mathbf{p}_{\text{fcs}} = \begin{bmatrix} T_{\text{st}} \end{bmatrix}^T \tag{4.20}$$

The resulting set of equations has 9 free variables (6 states $\mathbf{x}^i$ and 3 actuating variables $\mathbf{u}^i$) but only 6 equality constraints stated by the steady-state assumption in (4.17). An additional equality constraint is enforced by the reference power $P_{\text{fcs,bus,ref}}$ which should be met perfectly for steady-state.

$$P_{\text{fcs,bus}} = P_{\text{fcs,bus,ref}} \tag{4.21}$$

The resulting two additional degrees of freedom can be exploited by the ILC to optimize the operating point of the air supply. When the operating point consisting of the corrected air mass flow rate $\dot{m}_{\text{cr}}$ in (4.22) and the pressure ratio across the compressor Π in (4.23) is fixed, the resulting set of equations has a unique solution. The goal of the ILC is to find the optimal combination of $\dot{m}_{\text{cr}}$ and Π in terms of the above mentioned objectives.

$$\dot{m}_{\text{cr,ref}} = \dot{m}_{\text{cr}} \tag{4.22}$$

$$\Pi_{\text{ref}} = \Pi \tag{4.23}$$

In order to validate the influence of the operating point, the fuel cell system efficiency at the DC bus $\eta_{\text{fcs,bus}}$ is defined by (4.24). P_{lhv} is the lower heating power of the fuel cell stack and commonly used to calculate the efficiency of fuel cell systems [4]. It is defined by (4.25) whereby H_{H_2} defines the lower heating value of hydrogen. P_{lhv} is proportional to the stack current I_{st} and is thus also proportional to the hydrogen consumption $\dot{m}_{H_2}$.

$$\eta_{\text{fcs,bus}} = \frac{P_{\text{fcs,bus}}}{P_{\text{lhv}}} \tag{4.24}$$

$$P_{\text{lhv}} = \frac{n_{\text{cell}} H_{H_2}}{2F} I_{\text{st}} = \frac{H_{H_2}}{2M_H} I_{\text{st}} \dot{m}_{H_2} \tag{4.25}$$

In Appendix A.5, a qualitative analysis of the influences of the operating point on the efficiency $\eta_{\text{fcs,bus}}$ is conducted. The analysis reveals that an increase in the pressure ratio Π increases the stack power P_{st} but it also increases the electrical power consumption of the compressor motor P_{cm}. A numerical solution is required to get the dominant influence of these two and is conducted in the following.

In order to quantify the influence of the fuel cell system operating point on the efficiency $\eta_{\mathrm{fcs,bus}}$, the set of equations in (4.17, 4.21, 4.22 and 4.23) is solved numerically using the function fsolve in MATLAB®. Figure 4.4 presents the results of 4 examples of $P_{\mathrm{fcs,bus}}$ (2 kW, 10 kW, 20 kW, 40 kW). The gray area illustrates operating points where the oxygen excess ratio λ_{O_2} is below $\lambda_{O_2,\mathrm{min}}$ corresponding to the minimum oxygen excess ratio of the ILC. The colored surface represents the overall fuel cell system efficiency $\eta_{\mathrm{fcs,bus}}$. For all power ranges the efficiency $\eta_{\mathrm{fcs,bus}}$ is the highest for low pressure ratio Π and low corrected air mass flow rate $\dot{m}_{\mathrm{cr}}$. This supports the analysis done by *Larminies et al.* [4, Chapter 4]. Their conclusion was that from the pure efficiency point of view, it is often not beneficial to operate the system at higher pressure ratio Π. In the next section, it will be argued why it is still advantageous to operate at different operating points of the compressor map.

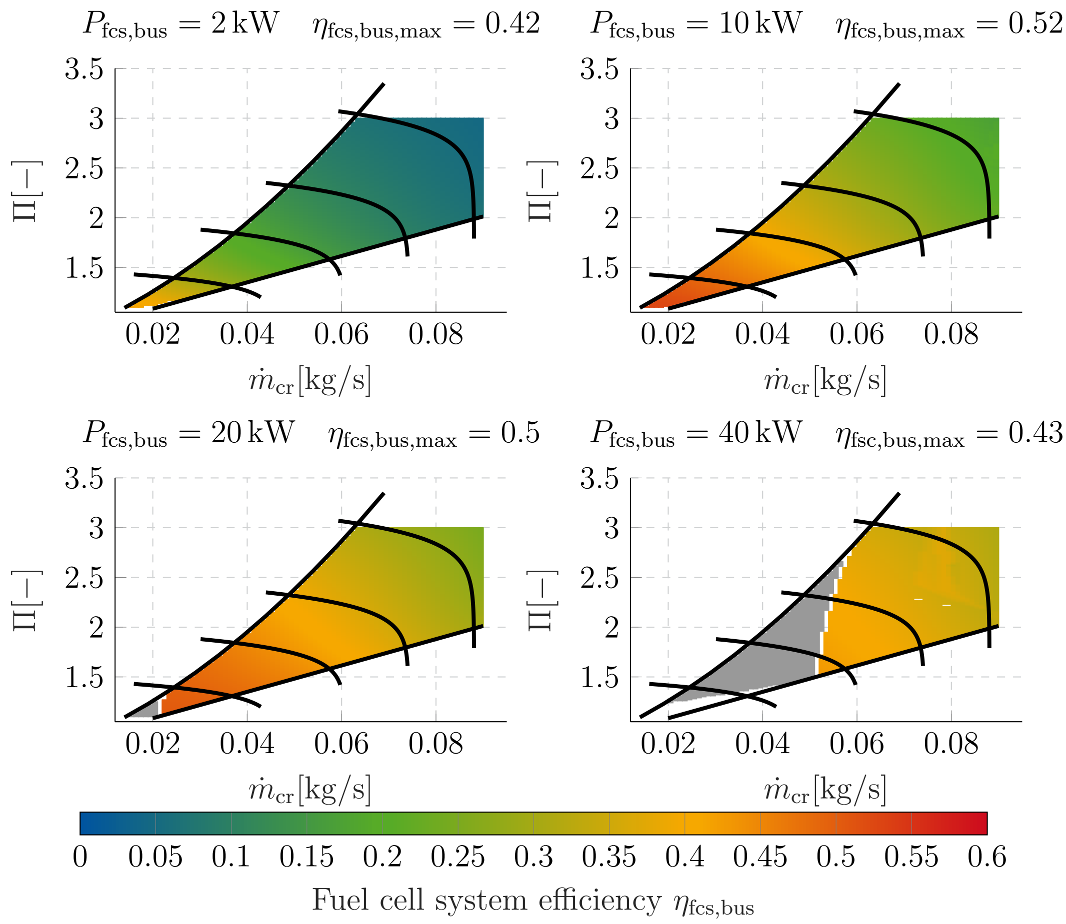

Fig. 4.4: Energy efficiency of different compressor operating points for a stack temperature of 80 °C and fixed fuel cell system power.

4.3.2 Operating Point Robustification towards Uncertain Power Demands

From the pure efficiency point of view, the optimal operating point is on the choke boundary at the lowest possible corrected air mass flow rate $\dot{m}_{\mathrm{cr}}$ as elaborated in the last section. However, another goal of the ILC is to assure a certain robustness to uncertain power demands on the fuel cell system power $P_{\mathrm{fcs,bus,ref}}$.

When an unpredicted increase in the power demand for the fuel cell system power $P_{\mathrm{fcs,bus,ref}}$ is applied, the constraint of the minimum oxygen excess ratio of the LLC $\lambda^{l}_{O_2,\mathrm{min}}$ has to be met. The stack current I_{st} and the oxygen mole flow rate into the cathode $\dot{n}_{\mathrm{cat,in}}$ are coupled by λ_{O_2} as stated in (2.3). Because $\dot{n}_{\mathrm{cat,in}}$ depends on $\dot{m}_{\mathrm{cr}}$, the control has to increase $\dot{m}_{\mathrm{cr}}$. This is only possible rapidly if the compressor does not operate at the choke boundary. The reason is that increasing the pressure ratio Π in this case is slow.

Two ways to increase the robustness to unpredicted increases in $P_{\mathrm{fcs,bus,ref}}$ exist. Firstly, the oxygen excess ratio λ_{O_2} can be set to values above the minimum $\lambda^{l}_{O_2,min}$. In this case, the LLC can decrease the oxygen excess ratio λ_{O_2} instead of increasing $\dot{m}_{\mathrm{cr}}$. Secondly, a horizontal distance to the choke boundary can be kept in order to be able to increase $\dot{m}_{\mathrm{cr}}$ rapidly. Both ways can be expressed as a single additional constraint.

In Figure 4.5, an illustration of the additional constraint is presented. The mathematical description of the constraint is given in (4.26). $\dot{m}_{\mathrm{cr,min}}$ (in blue) corresponds to the minimum air mass flow rate that has to be provided in order to comply with $\lambda^{i}_{O_2,\mathrm{min}}$. $\dot{m}_{\mathrm{cr,min}}$ plus a robustness term $\dot{m}_{\mathrm{rob}}$ has to be above the choke boundary of the compressor. This way, the actual operating point $\dot{m}_{\mathrm{op}}$ can either move along the orange line by increasing the oxygen excess ratio λ_{O_2} or by increasing the pressure ratio Π_{op} leading to a larger distance to the choke boundary. The robustifying parameter $\dot{m}_{\mathrm{rob}}$ is a design parameter of the ILC.

$$\Pi_{\mathrm{op}} > 0.82 + 13.13 \left(\dot{m}_{\mathrm{rob}} + \underbrace{\frac{\lambda_{O_2,\mathrm{min}}}{\lambda_{O_2}} \dot{m}_{\mathrm{cr,op}}}_{\dot{m}_{\mathrm{cr,min}}} \right) \tag{4.26}$$

The distance to the surge boundary is less critical because the oxygen excess ratio λ_{O_2} is not limited to a maximum value. The distance becomes relevant, when the power demand of the fuel cell system $P_{\mathrm{fcs,bus}}$ is decreasing and thus a lower $\dot{m}_{\mathrm{cr}}$ is demanded. In this case, however, the LLC can always react by temporarily increasing the oxygen excess ratio λ_{O_2} while slowly decreasing the pressure ratio Π.

Since it is not advised to operate at system constraints in steady-state, a small distance to the surge boundary is enforced by an additional constraint as given in (4.27). Similarly,

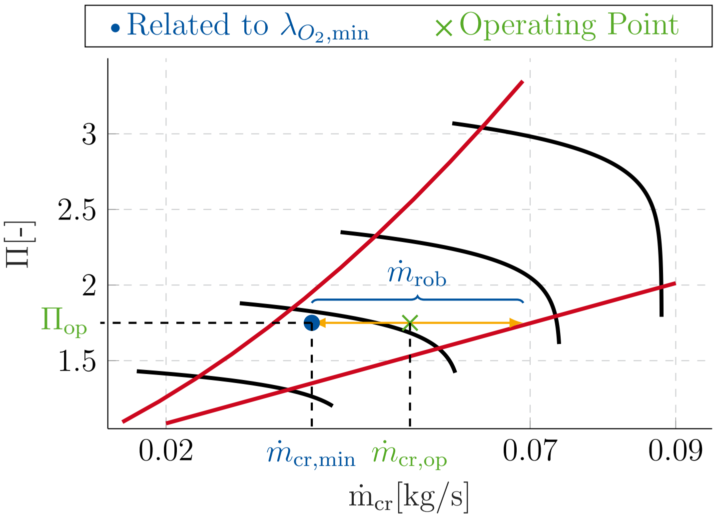

Fig. 4.5: Illustration of the robustification factor of the ILC.

a constraint for the minimum oxygen excess ratio $\lambda^{i}_{O_2,\mathrm{min}}$ is introduced in (4.28) that is larger than $\lambda^{l}_{O_2,\mathrm{min}}$.

$$\Pi < -278.69\dot{m}_{\mathrm{cr}}^2 + 17.88\dot{m}_{\mathrm{cr}} + 0.79 - \Pi^{i}_{\mathrm{rob}} \tag{4.27}$$

$$\lambda_{O_2} > \lambda^{i}_{O_2,\mathrm{min}} > \lambda^{l}_{O_2,\mathrm{min}} \tag{4.28}$$

4.3.3 Intermediate-Level Optimization Problem

The resulting optimization problem is presented in (4.29). It is a nonlinear static optimization with equality and inequality constraints. The problem is solved by using the nonlinear interior-point solver IPOPT [26].

$$\min_{\mathbf{u^i},\mathbf{x}^i} \quad J = \dot{m}_{H_2} \tag{4.29a}$$

$$s.t. \quad \text{Steady-state system (4.17)} \tag{4.29b}$$

$$\text{Power demand (4.21)} \tag{4.29c}$$

$$\text{Robustification(4.26, 4.27, 4.28)} \tag{4.29d}$$

In Figure 4.6, the results for two different factors $\dot{m}_{\mathrm{rob}}$ are presented. The stack temperature of T_{st} is set to 80 °C. The dotted lines correspond to $\dot{m}_{\mathrm{rob}} = 4\,\mathrm{g/s}$ and the solid line to $\dot{m}_{\mathrm{rob}} = 32\,\mathrm{g/s}$. In Figure 4.6a, the resulting operating line in the compressor map for $P_{\mathrm{fcs,bus}}$ ranging from 2 kW to 46 kW is presented. In Figure 4.6b, the fuel cell system power $P_{\mathrm{fcs,bus}}$ (in green) and the oxygen excess ratio λ_{O_2} (in red) are given. It can be seen that the results are mainly dominated by the constraint as given in (4.26) and additionally by the constraint stated by (4.27) as soon as λ_{O_2} reaches $\lambda^{i}_{O_2,\mathrm{min}}$. This result is expected due to the efficiency map introduced in Figure 4.4.

For $\dot{m}_{\mathrm{rob}} = 4\,\mathrm{g/s}$ at low $\dot{m}_{\mathrm{cr}}$, the operating point behaves unexpectedly. It can be explained by the fact that the back pressure valve is fully open. When the fuel cell system power $P_{\mathrm{fcs,bus}}$ increases, the reacted air mass flow rate $\dot{m}_{\mathrm{react}}$ also increases. This leads to a lower pressure ratio Π such that the operating point can shift along the constraint (4.27) to a lower $\dot{m}_{\mathrm{cr}}$.

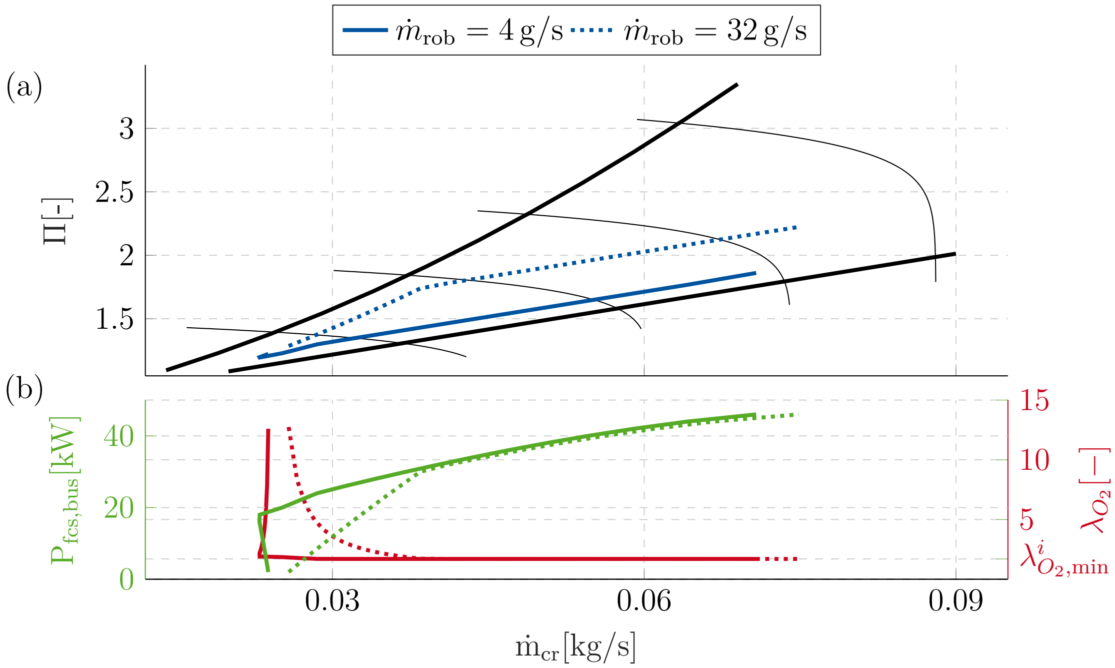

Fig. 4.6: Optimal operating points of the air supply for a stack temperature of 80 °C.

The solution of the optimization problem only depends on a limited number of possible variables T_{st}, $\dot{m}_{\mathrm{rob}}$ and $P_{\mathrm{fcs,bus}}$. Therefore, the solutions are calculated offline and stored in lookup tables with linear interpolation. These are used online to find the optimal operating point of the air supply.

Summing up, the ILC finds the optimal operating point of the air supply in terms maximum efficiency and complies with the given constraints. The resulting parameters of the ILC are presented in Table A.6 including the lookup table parameter ranges.

4.4 High-Level Control Design

In this section, the design of the HLC is presented. As for the LLC, the problem is solved with an NMPC. In Section 4.4.1 It receives the predicted power demand P_{dem} and returns the optimal split between the fuel cell system power $P_{\mathrm{fcs,bus,ref}}$ and the battery power $P_{\mathrm{bat,bus,ref}}$. The controller specific objectives can be summarized as follows:

1. **Hydrogen consumption minimization**: The hydrogen consumption $\dot{m}_{H_2}$ should be minimized over the prediction horizon of the MPC.
2. **Charge sustainability**: The battery SOC should be close to a given SOC reference at the end of the prediction horizon $\mathrm{SOC}(N_\mathrm{P}^h)$.
3. **Compliance with constraints on a long time scale**: System constraints comprising the power limitations of the components and battery SOC range must be considered.

The prediction model of the NMPC is presented. The cost function is introduced in Section 4.4.2. Subsequently, the system constraints are given in Section 4.4.3. Finally, the resulting optimal control problem is presented in Section 4.4.4.

4.4.1 High-Level Prediction Model

The prediction model is based on the nonlinear state-space system in (4.30). The models of the battery and the DC/DC converters are taken from Chapter 3. The dynamics of the fuel cell system are neglected according to Figure 4.2. Therefore, a steady-state model of the fuel cell system is derived.

$$\dot{\mathbf{x}}^h(t) = f(\mathbf{x}^h(t), \mathbf{u}^h(t), \mathbf{z}^h(t)) \tag{4.30a}$$

$$\mathbf{y}^h(t) = g(\mathbf{x}^h(t), \mathbf{u}^h(t), \mathbf{z}^h(t), \mathbf{p}^h(t)) \tag{4.30b}$$

Whereby, $\mathbf{x}^h$, $\mathbf{u}^h$, $\mathbf{z}^h$, $\mathbf{p}^h$ and $\mathbf{y}^h$ denote the state, input, disturbance, parameter and output vector respectively. The only considered state is the battery SOC. All the other states from the LLC are assumed to be at steady-state.

$$\mathbf{x}^h = \mathbf{x}_\mathrm{bat} = \begin{bmatrix} \mathrm{SOC} \end{bmatrix}^T \tag{4.31}$$

$\mathbf{u}^h$ consists of the power reference values $P_\mathrm{fcs,bus,ref}$ and $P_\mathrm{bat,bus,ref}$.

$$\mathbf{u}^h = \begin{bmatrix} P_\mathrm{fcs,bus,ref} & P_\mathrm{bat,bus,ref} \end{bmatrix}^T \tag{4.32}$$

The disturbance vector $\mathbf{z}^h$ to the system consists of the demanded power P_dem. It is expressed as a disturbance because it has to be fulfilled perfectly at every time step.

$$\mathbf{z}^h = \begin{bmatrix} P_\mathrm{dem} \end{bmatrix}^T \tag{4.33}$$

The outputs of the system $\mathbf{y}^h$ are the lower heating power of the fuel cell system P_lhv and the battery SOC. Note that P_lhv is proportional to the hydrogen consumption $\dot{m}_{H_2}$ as stated in (4.25). Thus, minimizing P_lhv corresponds to minimizing $\dot{m}_{H_2}$.

$$\mathbf{y}^h = \begin{bmatrix} P_\mathrm{lhv} & \mathrm{SOC} \end{bmatrix}^T \tag{4.34}$$

The parameter vector consist of the stack temperature T_{st}. As demonstrated in Figure 4.1, the time constants of the stack temperature are larger than the prediction horizon of the MPC.

$$\mathbf{p}^h = \mathbf{p}_{\mathrm{fcs}} = \left[\ T_{\mathrm{st}}\ \right]^T \tag{4.35}$$

The lower heating power of the fuel cell system P_{lhv} is expressed as a function of the fuel cell system power $P_{\mathrm{fcs,bus,ref}}$, the stack temperature T_{st} and the robustification factor $\dot{m}_{\mathrm{rob}}$ as given in (4.36). The function is given as a 3-dimensional look up table that is deduced from the steady-state model of the fuel cell system. Therefore, the nonlinear set of equations is solved by the function fsolve in MATLAB®.

$$P_{\mathrm{lhv}} = f(P_{\mathrm{fcs,bus,ref}}, T_{\mathrm{st}}, \dot{m}_{\mathrm{rob}}) \tag{4.36}$$

In Figure 4.7, the resulting efficiency $\eta_{\mathrm{fcs,bus}}$ is presented instead of P_{lhv} for a better illustration. $\eta_{\mathrm{fcs,bus}}$ can be calculated from P_{lhv} by (4.24). In Figure 4.7a the dependency on the stack temperature T_{st} is shown. With increasing T_{st}, the efficiency of the fuel cell system also increases. In Figure 4.7b the dependency on the robustification factor $\dot{m}_{\mathrm{rob}}$ is illustrated. With increasing $\dot{m}_{\mathrm{rob}}$, the efficiency $\eta_{\mathrm{fcs,bus}}$ decreases.

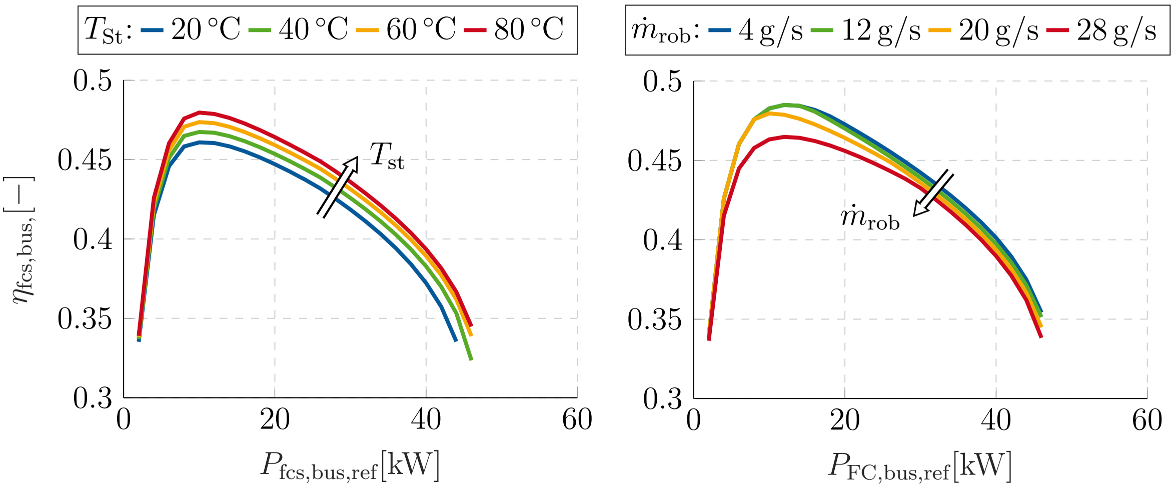

(a) Dependend on T_{st} for $\dot{m}_{\mathrm{rob}} = 2\,\mathrm{g/s}$.

(b) Dependend on $\dot{m}_{\mathrm{rob}}$ for $T_{\mathrm{st}} = 80\,°\mathrm{C}$

Fig. 4.7: Efficiency curves of the fuel cell system including the DC/DC converter.

In order to penalize the derivatives of the input vector $\mathbf{u}^h$, the augmented states $\tilde{\mathbf{x}}^h$ are introduced in (4.37). The derivatives $\dot{\mathbf{u}}^h$ need to be penalized in order to prevent the controller from putting high gradients on the power values $P_{\mathrm{fcs,bus,ref}}$ and $P_{\mathrm{bat,bus,ref}}$ even if it is not required by the demanded power P_{dem}.

$$\tilde{\mathbf{x}}^h = \begin{bmatrix} \mathbf{x}^h \\ \mathbf{u}^h \end{bmatrix}, \qquad \tilde{\mathbf{u}}^h = \dot{\mathbf{u}}^h, \qquad \mathbf{u}^h = \int \dot{\mathbf{u}}^h \mathrm{d}t \tag{4.37}$$

4.4.2 High-Level Cost Function

The cost function in (4.38) corresponds to the objectives listed at the beginning of this Section. The hydrogen consumption over the prediction horizon N_P^h is penalized in (4.38a). The input derivatives $\dot{\mathbf{u}}^h$ are penalized in (4.38b). In (4.38c), the deviation of $\mathrm{SOC}(N_\mathrm{P}^h)$ to the reference $\mathrm{SOC}_\mathrm{ref}(N_\mathrm{P}^h)$ at the end of the prediction horizon is penalized. The slack variables of the soft constraints in (4.40) are penalized in (4.38d).

In (4.38e), a decision inertia on the first solution of the HLC is introduced in order to corporately work with the LLC. Therefore, the deviation of the first value of the current optimization $P_\mathrm{fcs,bus,ref,0}$ to the second value of the prior optimization $P_\mathrm{fcs,bus,ref,1,last}$ is penalized. The effect is that the HLC does not change the predicted values which have already been appeared in the prediction horizon of the LLC. The consequences when the decision inertia is not applied are demonstrated in Section 5.3.3

$$\begin{aligned} J = \int_0^{T_\mathrm{P}^h} & q_{P_\mathrm{lhv}} P_\mathrm{lhv} && \text{(Hydrogen consumption)} && (4.38\mathrm{a}) \\ & + \|\dot{\mathbf{u}}^h\|^2_{\mathbf{R}^h} dt && \text{(Control input derivatives)} && (4.38\mathrm{b}) \\ & + \|(\mathrm{SOC}(N_\mathrm{P}^h) - \mathrm{SOC}_\mathrm{ref}(N_\mathrm{P}^h))\|^2_{q_\mathrm{SOC}} && \text{(Final SOC)} && (4.38\mathrm{c}) \\ & + \|\boldsymbol{\epsilon}_i\|^2_{\mathbf{Q}_\mathrm{S}^h} && \text{(Slack variables SOC)} && (4.38\mathrm{d}) \\ & + \|P_\mathrm{fcs,bus,ref,0} - P_\mathrm{fcs,bus,ref,1,last}\|^2_{\mathbf{q}_{P_\mathrm{fcs,0}}} && \text{(Inertia on first } P_\mathrm{fcs,bus,ref}\text{)} && (4.38\mathrm{e}) \end{aligned}$$

The weighting matrices of the slack variables $\mathbf{Q}_S^h$ and the control inputs $\mathbf{R}^h$ are given in (4.39). The weights on $\mathbf{Q}_S^h$ are large in order to prevent the controller from violating the constraints extensively. The weights on $\mathbf{R}^h$ are small because they only prevent the controller from changing the control inputs $\mathbf{u}^h$ extensively.

$$\mathbf{Q}_\mathrm{S}^h = \begin{bmatrix} q_{\mathrm{S},P_\mathrm{fcs}} & 0 \\ 0 & q_\mathrm{S,SOC} \end{bmatrix}, \qquad \mathbf{R}^h = \begin{bmatrix} r_{P_\mathrm{fcs}} & 0 \\ 0 & r_{P_\mathrm{bat}} \end{bmatrix} \tag{4.39}$$

The weights q_{P_lhv} and $q_\mathrm{S,SOC}$ assess the cost terms (4.38a) and (4.38c). Increasing q_{P_lhv} leads to a stronger deviation of the battery SOC while increasing $q_\mathrm{S,SOC}$ leads to a weaker deviation of the battery SOC. A careful tuning of these weights is necessary to achieve good results.

The reference SOC at the end of the prediction horizon $\mathrm{SOC}_\mathrm{ref}(N_\mathrm{P}^h)$ is often set to a constant value [11, 55]. The HLC with constant $\mathrm{SOC}_\mathrm{ref}(N_\mathrm{P}^h)$ is further denoted by $\mathrm{HLC}_\mathrm{const}$ and is further investigated with regards to the optimal choice of N_P^h and $q_\mathrm{S,SOC}$ in Section 5.2.2.

When information about the power demand is available beyond the prediction horizon N_P^h, it might be beneficial to incorporate this information in the SOC reference. Since trips are usually assisted by navigation systems nowadays, it can be assumed that an approximate power demand prediction for the whole driving cycle is available [73]. Therefore, an offline optimization can be conducted leading to an approximate optimal $\mathrm{SOC}_{\mathrm{ref}}(N_{\mathrm{P}}^h)$ trajectory. The HLC with variable $\mathrm{SOC}_{\mathrm{ref}}(N_{\mathrm{P}}^h)$ is further denoted by $\mathrm{HLC}_{\mathrm{var}}$. The modification is evaluated in Section 5.2.3.

4.4.3 High-Level System Constraints

The HLC is not subject to any input constraints because the input derivatives $\dot{\mathbf{u}}^h$ are not limited. Consequently power reference values $P_{\mathrm{bat,bus,ref}}$ and $P_{\mathrm{fcs,bus,ref}}$ can possibly vary from the minimum to the maximum value within one time step.

The optimal control problem has constraints on the fuel cell system power $P_{\mathrm{fcs,bus,ref}}$, the battery power $P_{\mathrm{bat,bus,ref}}$, the battery SOC and the slack variables as stated in (4.40). The maximum power $P_{\mathrm{fcs,bus,ref,max}}$ depends on the stack temperature T_{st} as illustrated in Figure 4.7a. The fuel cell system power $P_{\mathrm{fcs,bus,ref}}$ and the battery SOC limitations are implemented as soft constraints. The soft constraint on the fuel cell system power is required because, otherwise, the optimal control problem can become infeasible if P_{dem} is too large. The SOC soft constraint is necessary because the underlying control does not consider those constraints and might drift the SOC outside the feasible region. The soft constraints are applied by employing the slack variables ϵ_{S} and $\epsilon_{P_{\mathrm{bat}}}$. In order to reduce the dimensionality of the optimization problem, the slack variables are implemented in the ∞-norm leading to only one additional optimization variable per soft constraint [6].

$$0 \geq \mathbf{h}^h(\mathbf{x}^h(t)) = \begin{bmatrix} P_{\mathrm{bat,bus,ref,min}} - P_{\mathrm{bat,bus,ref}} \\ P_{\mathrm{bat,bus,ref}} - P_{\mathrm{bat,bus,ref,max}} \\ P_{\mathrm{fcs,bus,ref,min}} - P_{\mathrm{fcs,bus,ref}} - \epsilon_{P_{\mathrm{fcs}}} \\ P_{\mathrm{fcs,bus,ref}} - P_{\mathrm{fcs,bus,ref,max}}(T_{\mathrm{st}}) - \epsilon_{P_{\mathrm{fcs}}} \\ \mathrm{SOC}_{\mathrm{min}} - \epsilon_{\mathrm{S}} - \mathrm{SOC} \\ \mathrm{SOC} - \mathrm{SOC}_{\mathrm{max}} - \epsilon_{\mathrm{S}} \\ -\epsilon_{\mathrm{S,SOC}} \\ -\epsilon_{P_{\mathrm{fcs}}} \end{bmatrix} \begin{matrix} \text{(min battery power)} \\ \text{(max battery power)} \\ \text{(min FCS power)} \\ \text{(max FCS power)} \\ \text{(min SOC)} \\ \text{(max SOC} \\ \text{(slack on SOC)} \\ \text{(slack on FCS power)} \end{matrix} \tag{4.40}$$

4.4.4 High-Level Optimal Control Problem

The resulting optimal control problem (OCP) can be found in (4.41) and corresponds to the optimal control problem formulation as stated by (2.7).

$$\begin{aligned} \min_{\mathbf{u}^h} \quad & \text{Cost function (4.38)} && \text{(4.41a)} \\ \text{s.t.} \quad & \text{System dynamics (4.30)} && \text{(4.41b)} \\ & \text{State constraints (4.40)} && \text{(4.41c)} \end{aligned}$$

The parameters of the HLC are given in Table A.5. The parameter q_S, $\mathrm{SOC}_\mathrm{ref}$ and N_P^h are left open for further studies in Chapter 5. The sampling time T_S^h is 1 s. It is solved with a direct method utilizing multiple shooting (compare Section 2.2.2). The prediction model as given in (4.30) is discretized with a Runge-Kutta 4th-order method [29]. The toolbox CasADI is used to formulate the discretized nonlinear optimization problem [72]. The resulting nonlinear optimization problem is solved using the toolbox IPOPT [26].

5 Results

In this chapter, the hierarchical control is evaluated based on a predefined driving cycle. For this purpose, the WLTC is chosen and introduced in Section 5.1. The evaluation criterion are the objectives listed in Section 4.1 which comprise dynamic power delivery, hydrogen consumption minimization, charge sustainability of the battery and compliance with operating constraints. Consequently, the evaluation is divided into three steps. At first, only the HLC is compared to the global optimal solution that is achieved by a DP method in Section 5.2. Additionally, the modification of the HLC which utilizes information beyond the prediction horizon is proposed. In Section 5.3, the entire hierarchical control is validated in terms of deviation from the HLC predicted solution. In Section 5.3, the results of the LLC are presented.

5.1 Driving Cycle for the Validation

In autumn 2007 the United Nations Organization (UNO) started developing a roadmap for the worldwide harmonized light vehicle test procedure (WLTP). The goal was to standardize the measurements of exhaust emissions worldwide. In the EU, WLTP became obligatory in September 2018 and replaced the controversial NEDC. WLTP is not only the driving cycle itself but specifies the testing procedure and conditions for measuring the exhaust emissions [74].

The driving cycle corresponding to the WLTP is the worldwide harmonized light vehicles test cycle (WLTC). It is grouped into subclasses depending on the power to mass ratio. The driving cycle for the medium sized car chosen in this thesis is the WLTC3. In Figure 5.1a, the velocity profile of the driving cycle is presented. It consists of four phases: the low-, middle-, high-, and extra-high-speed phase. Overall, a distance of 23.62 km is covered in 1800 s. The driving cycle achieves a peak speed of up to 131 km/h and an average speed of 46.6 km/h.

Figure 5.1b shows the demanded power at the DC bus P_{dem}. It is calculated from the vehicle model as described by *Dirkes* [7]. The propulsive power P_{dem}^{+} illustrated in blue has its peak power at 67.3 kW and an average power of 10.46 kW. The regenerative power P_{dem}^{-} illustrated in green has its maximum power at 39.8 kW whereby only 33 kW can be regenerated by the battery due to the minimum power $P_{\mathrm{bat,bus,min}}$. The remaining energy has to be absorbed by the breaks.

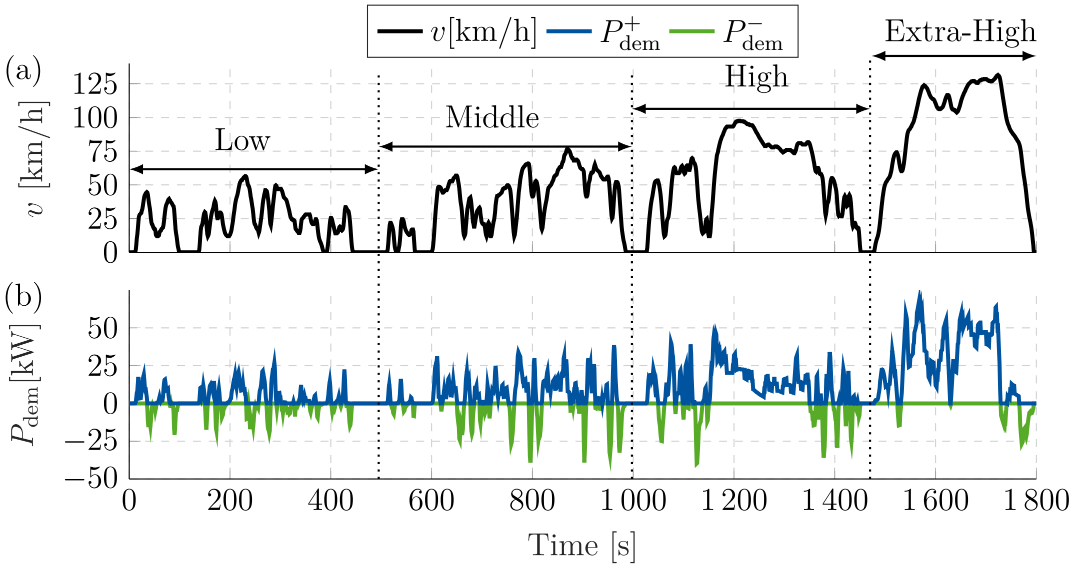

Fig. 5.1: Speed profile and power demand of the WLTC3 driving cycle.

5.2 High-Level Control Evaluation

In this section, the HLC is evaluated separately from the LLC. Thus, the controller is examined on the static model of the fuel cell system (compare Figure 4.7). For the evaluation, the stack temperature T_{st} is set to 80 °C and the robustification factor $\dot{m}_{\text{rob}}$ is set to 20 g/s. The HLC is compared to the DP method introduced in Section 5.2.1. Subsequently, the influences of the final battery SOC weight q_{SOC} and the prediction horizon N^h_{P} on the HLC with constant $\text{SOC}_{\text{ref}}(N^h_{\text{P}})$ denoted by $\text{HLC}_{\text{const}}$ is validated. In Section 5.2.3, the HLC with variable $\text{SOC}_{\text{ref}}(N^h_{\text{P}})$ denoted by HLC_{var} is evaluated. Finally, in Section 5.2.4, DP, $\text{HLC}_{\text{const}}$ and HLC_{var} are compared with each other in terms of hydrogen consumption, charge sustainability and compliance with operating constrains.

5.2.1 Global Optimal Solution of the High-Level Control

The global optimal solution is determined using dynamic programming (DP). An introduction to the general idea of DP is given in Section 2.2.2. The generic dynamic programming MATLAB® function developed by *Sundstrom et al.* [75] is used to solve the optimal control problem given in (2.25). The dynamic programming optimization minimizes the hydrogen consumption $\dot{m}_{H_2}$ for a given driving cycle and ensures a certain final battery SOC at the end of the driving cycle SOC(T). The state discretization of the DP method is chosen so dense (300 steps for each input and state) that it is assumed to be the optimal solution.

In Figure 5.2a, the optimal power split between the battery and the fuel cell system is presented. The propulsive power P^+_{del} (blue) consists of the fuel cell system power $P_{\text{fcs,bus,ref}}$

(dark blue) and the battery discharge power $P_{\text{bat,D,bus,ref}}$ (light blue). The regenerative power P^{-}_{del} (green) consists of the regenerative battery power $P_{\text{bat,R,bus,ref}}$ (light green) and the battery charging power $P_{\text{bat,C,bus,ref}}$ (dark green) provided by the fuel cell system. In Figure 5.2b, the SOC trajectory is presented including the minimum and maximum limitations $\text{SOC}_{\text{min,max}}$. The initial $\text{SOC}(t_0)$ and final $\text{SOC}(T)$ of the driving cycle are set to 0.6.

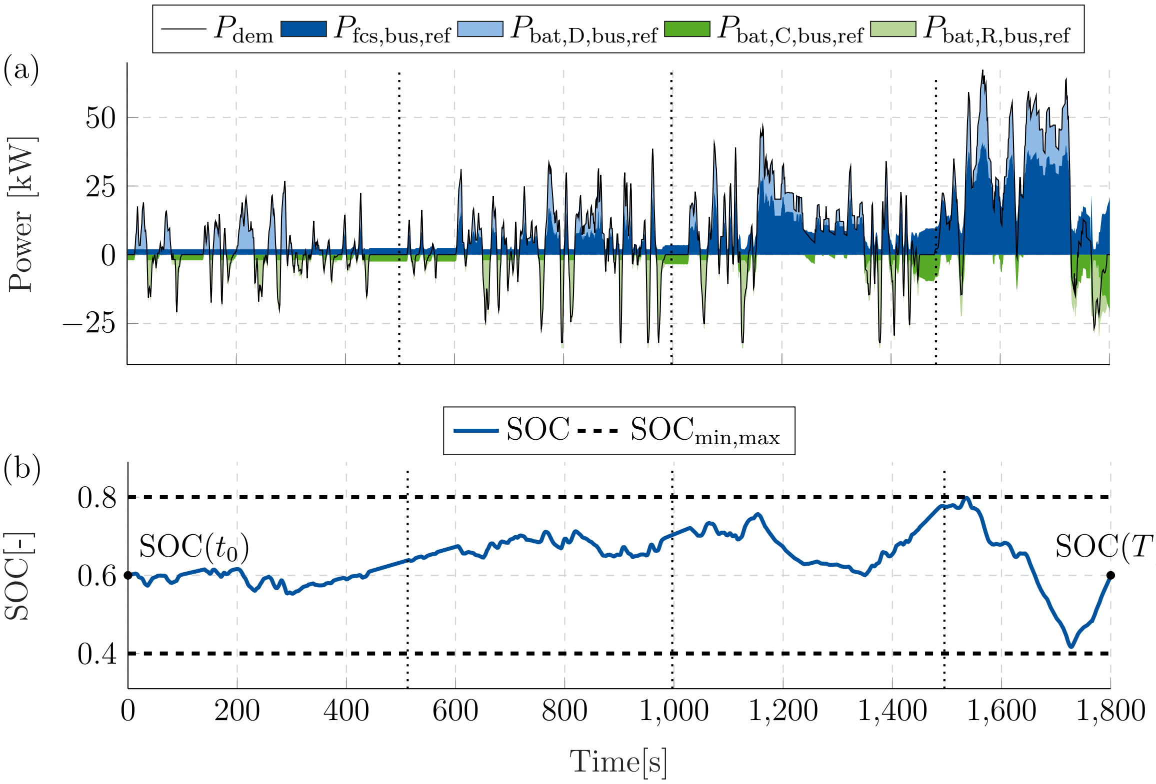

Fig. 5.2: Power split and SOC trajectory of the DP method.

The DP method utilizes global predictive information and thus exploits the full SOC range from 0.4 to 0.8. For the sake of illustration, the optimal solution is analyzed phase-wise. In the low-speed phase from 0 s to 500 s, the battery is mostly used for propulsion. The average demanded power $\bar{P}_{\text{dem}}$ in this phase is only 1.45 kW while the minimum fuel cell system bus power $P_{\text{fcs,bus,ref,min}}$ is 2 kW.

In the middle-speed phase, the fuel cell system primarily operates within its high efficiency region from 5 kW to 20 kW when propulsion power P^{+}_{dem} is required, and at minimum power $P_{\text{fcs,bus,ref,min}}$ when less power is required. The average power demand $\bar{P}_{\text{dem}}$ in this phase is 3.65 kW.

In the high-speed phase, the fuel cell system still mostly operates within its high efficiency region. The battery SOC nearly reaches its maximum of 0.8 at 1200 s before it strongly supports the fuel cell system for acceleration. From 1400 s to 1500 s, the fuel cell system actively charges the battery with around 10 kW in order to increase the SOC close to its maximum value before the upcoming extra-high-speed phase. The average power demand $\bar{P}_{\mathrm{dem}}$ in this phase is 8.5 kW. Consequently, the optimization is less dominated by the minimum power of the fuel cell system $P_{\mathrm{fcs,bus,ref,min}}$.

In the extra-high-speed phase, the average power demand $\bar{P}_{\mathrm{dem}}$ is 15.87 kW with its peak value of 67.31 kW at 1550 s. This is above the maximum power of the fuel cell system power $P_{\mathrm{fcs,bus,ref,max}}$ of 46 kW. Therefore, the fuel cell system requires strong support from the battery which is only possible because the DP method has global knowledge of the power demand P_{dem} and has increased the battery SOC at the end of the high-speed phase. The last few seconds of this phase are utilized to recharge the battery to its final SOC of 0.6.

5.2.2 Influence of Weights and Prediction Horizon

In this section, the weight q_{SOC} and the prediction horizon N_{P}^{h} of the $\mathrm{HLC}_{\mathrm{const}}$ as described in (4.38) are examined. $\mathrm{SOC}_{\mathrm{ref}}(N_{\mathrm{P}}^{h})$ is set to 0.6 plus an offset $\Delta\mathrm{SOC}$ of 0.1 as given by (5.1) because the HLC tends to reach a lower SOC than specified. This behavior can be explained by the economical cost of the lower heating power P_{lhv} given in (4.38a) which pushes $\mathrm{SOC}(N_{\mathrm{P}}^{h})$ down.

$$\mathrm{SOC}_{\mathrm{ref}}(N_{\mathrm{P}}^{h}) = 0.6 + \Delta\mathrm{SOC} \tag{5.1}$$

For different parameter settings of the HLC, the driving cycle finishes with different $\mathrm{SOC}(T)$. In order to make the hydrogen consumption comparable between the methods, an equivalent hydrogen consumption $m_{H_2,eq}$ is introduced that accounts for the deviation of $\mathrm{SOC}(T)$ [76].

The deviation of energy stored in the battery ΔE_{bat} is given in (5.2) whereat Q is the storage capacity of the battery. The open circuit voltage $U_{\mathrm{OCV,const}}$ is assumed to be constant at 1.27 V(compare Figure 3.8).

$$\Delta E_{\mathrm{bat}} = (\mathrm{SOC}(T) - \mathrm{SOC}_{\mathrm{ref}}(T)) \cdot Q \cdot U_{\mathrm{OCV,const}} \tag{5.2}$$

Depending on ΔE_{bat}, the equivalent fuel cell system energy $\Delta E_{\mathrm{fcs,eq}}$ can be calculated by a case-distinction as given in (5.3). If the remaining energy in the battery ΔE_{bat} is greater than zero, $\Delta E_{\mathrm{fcs,eq}}$ describes the surplus energy in the battery in terms of the lower heating energy of hydrogen in the fuel cell system. If ΔE_{bat} is smaller than zero, $\Delta E_{\mathrm{fcs,eq}}$ describes the lower heating energy of hydrogen that is required to recharge the battery to $\mathrm{SOC}(T) = 0.6$. The corresponding efficiencies $\bar{\eta}_{\mathrm{fcs,bus}}$, $\bar{\eta}_{\mathrm{bat,D,bus}}$ and $\bar{\eta}_{\mathrm{bat,C,bus}}$ are averaged efficiencies of the components over the whole driving cycle. Despite the fact that averaged efficiencies are a valid assumption, they can greatly influence the result especially in the case of short driving cycles.

$$\Delta E_{\text{fcs,eq}} = \Delta E_{\text{bat}} \cdot \begin{cases} \frac{\bar{\eta}_{\text{bat,D,bus}}}{\bar{\eta}_{\text{fcs,bus}}}, & \text{if} \quad \Delta E_{\text{bat}} > 0 \\ \frac{1}{\bar{\eta}_{\text{bat,C,bus}}\bar{\eta}_{\text{fcs,bus}}}, & \text{else} \end{cases} \tag{5.3}$$

The equivalent hydrogen consumption can be obtained by (5.4), whereby $m_{\text{fcs,eq}}$ is proportional to the equivalent fuel cell energy $\Delta E_{\text{fcs,eq}}$ and M_H denotes the molar mass of hydrogen. $m_{\text{fcs,eq}}$ is subtracted from the total hydrogen consumption $m_{H_2,\text{tot}}$ in order to obtain $m_{H_2,\text{eq}}$. Even though the duration of the WLTC3 driving cycle is long with 1800 s, it should be noticed that $m_{H_2,\text{eq}}$ is just an estimate that includes assumptions about the upcoming driving behavior to make the results comparable.

$$m_{H_2,\text{eq}} = m_{H_2,\text{tot}} - m_{\text{fcs,eq}} = m_{H_2,\text{tot}} - \Delta E_{FC,eq}\frac{2M_H}{H_{H_2}} \tag{5.4}$$

In Figure 5.3, the equivalent hydrogen consumption $m_{H_2,\text{eq}}$ is illustrated for different combinations of the prediction horizon N_P^h and the final SOC weight q_SOC. N_P^h varies between 5 and 35 while the q_SOC varies between 5 and 105.

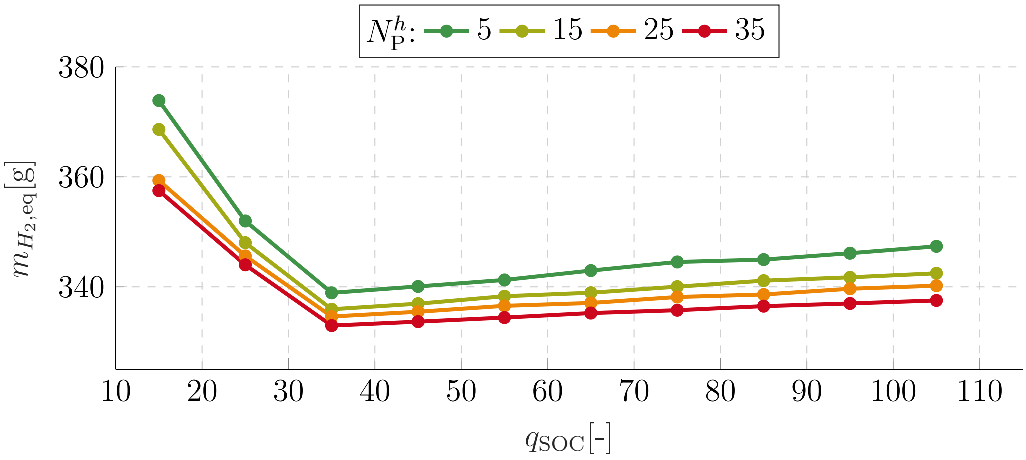

Fig. 5.3: Influence of the HLC parameters on the equivalent hydrogen consumption.

If the final SOC weight q_SOC is chosen too low, the equivalent hydrogen consumption $m_{H_2,\text{eq}}$ is large because the battery reaches the lower SOC limit of 0.4 in the extra-high speed phase. Consequently, the fuel cell system has to operate at its maximum power $P_{\text{fcs,bus,ref,max}}$ which leads to a poor efficiency $\eta_{\text{fcs,bus}}$. With increasing q_SOC, the hydrogen consumption decreases until it reaches a minimum at 35. From this weight onwards, the battery operates within its operating limits even for the extra-high-speed phase. Further increasing the weight leads to the disadvantage that the SOC range of the battery is not fully exploited. However, the increase in equivalent hydrogen consumption $m_{H_2,\text{eq}}$ is low. For further investigations, q_SOC is chosen to be 35.

With increasing prediction horizon N_P^h, the equivalent hydrogen consumption $m_{H_2,\text{eq}}$ decreases. However, the computational cost of the optimization increases. Table 5.1 lists the average and maximum computation time of the HLC. Important to note are not the absolute values of the computation time but the trend which is approximately linearly increasing with N_P^h. For further investigation, a prediction horizon N_P^h of 15 (equals 15 s for $T_\mathrm{S}^h = 1\,\mathrm{s}$) is chosen as it gives a good trade-off between hydrogen consumption and computation time.

Tab. 5.1: Computation time of the HLC depending on the prediction horizon.

N_P^h	5	15	25	35
Average computation time [s]	0.08	0.22	0.37	0.54
Maximum computation time [s]	0.14	0.36	0.56	0.78

Summing up, it is possible to find an optimized combination of parameters for the given WLTC3 driving cycle. It should be mentioned that the optimal weight on the final SOC q_SOC is expected to vary depending on the driving cycle (compare Appendix A.8). In order to achieve a low hydrogen consumption, it is important that the battery does not reach the SOC limitations because this forces the controller to use the fuel cell system individually. The $\mathrm{HLC}_\mathrm{const}$ can only handled the SOC variation by adjusting q_SOC to a value that is large enough. However, if q_SOC is chosen too large, the controller does not utilize the battery for shifting the operating point of the fuel cell system into high efficiency ranges but is only concerned about reaching the final SOC reference $\mathrm{SOC}_\mathrm{ref}(N_\mathrm{P}^h)$.

5.2.3 High-Level Control with Variable SOC Reference

The $\mathrm{HLC}_\mathrm{const}$ suffers from the fact that only information during the prediction horizon N_P^h is utilized. In this section, the $\mathrm{HLC}_\mathrm{var}$ is proposed that can take global information via $\mathrm{SOC}_\mathrm{ref}(N_\mathrm{P}^h)$ into account. It is expected that this method leads to a lower equivalent hydrogen consumption $m_{H_2,\mathrm{eq}}$.

In order to take global information into account, the offline solution from the DP method is utilized. The SOC reference trajectory SOC_DP calculated by the DP method is used to determine $\mathrm{SOC}_\mathrm{ref}(N_\mathrm{P}^h)$ as given in (5.5). At time step k, $\mathrm{SOC}_{k,\mathrm{ref}}(N_\mathrm{P}^h)$ is determined by the SOC of the DP method $\mathrm{SOC}_\mathrm{DP}(k+N_\mathrm{P}^h)$ plus an offset $\Delta\mathrm{SOC}$ of 0.1.

$$\mathrm{SOC}_{k,\mathrm{ref}}(N_\mathrm{P}^h) = \mathrm{SOC}_\mathrm{DP}(k+N_\mathrm{P}^h) + \Delta\mathrm{SOC} \tag{5.5}$$

In Figure 5.4, the resulting power split is presented. The result is similar to the one obtained by the DP method in Figure 5.2. In the low-speed phase, $P_\mathrm{fcs,ref,bus}$ is utilized more because $\mathrm{SOC}_\mathrm{ref}(N_\mathrm{P}^h)$ is $\Delta\mathrm{SOC}$ larger than for the DP method. In return, the HLC uses the fuel cell system less in the high-speed phase because the economical cost of the lower heating power P_lhv raises when the power demand P_dem increases. Consequently, $\mathrm{SOC}(N_\mathrm{P}^h)$ is pushed below $\mathrm{SOC}_\mathrm{ref}(N_\mathrm{P}^h)$ more strongly. As for the DP method, $\mathrm{HLC}_\mathrm{var}$ does not operate the fuel cell system at its maximum power $P_{\text{fcs,bus,ref,max}}$ in the extra-high speed phase.

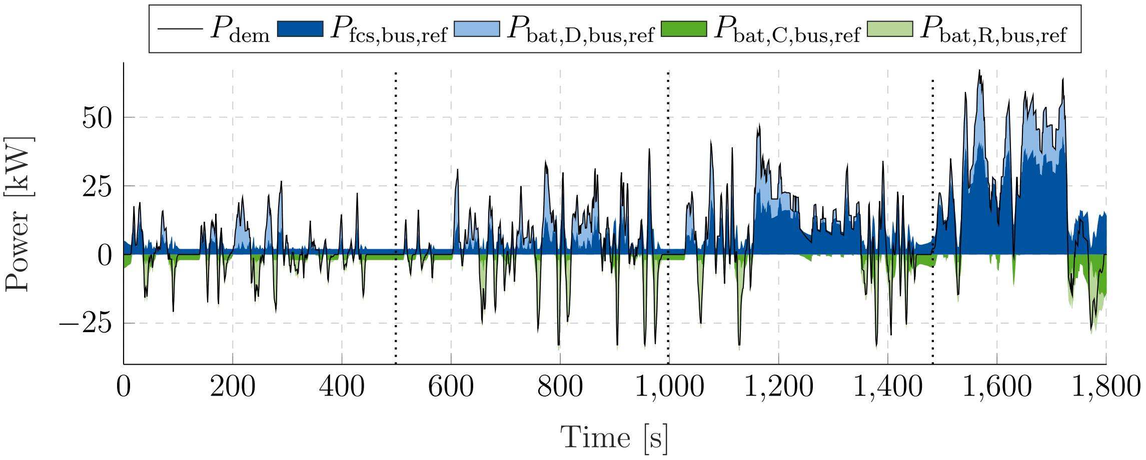

Fig. 5.4: Power split of HLC_{var}.

5.2.4 Methods Comparison

In Figure 5.5, the SOC trajectories of the three introduced methods are compared. The SOC trajectory resulting from DP was already introduced in Figure 5.2. The SOC trajectory of $\text{HLC}_{\text{Const}}$ is always varying between 0.45 and 0.7. Especially the low battery use in the extra-high speed phase leads to a poor efficiency of the fuel cell system $\eta_{\text{fcs,bus}}$ because it has to operate at its maximum power $P_{\text{fcs,bus,ref,max}}$. The SOC trajectory of HLC_{var} follows approximately the trajectory of the DP method. Only in the low-speed phase the MPC utilizes the battery less and in return more in the high-speed phase.

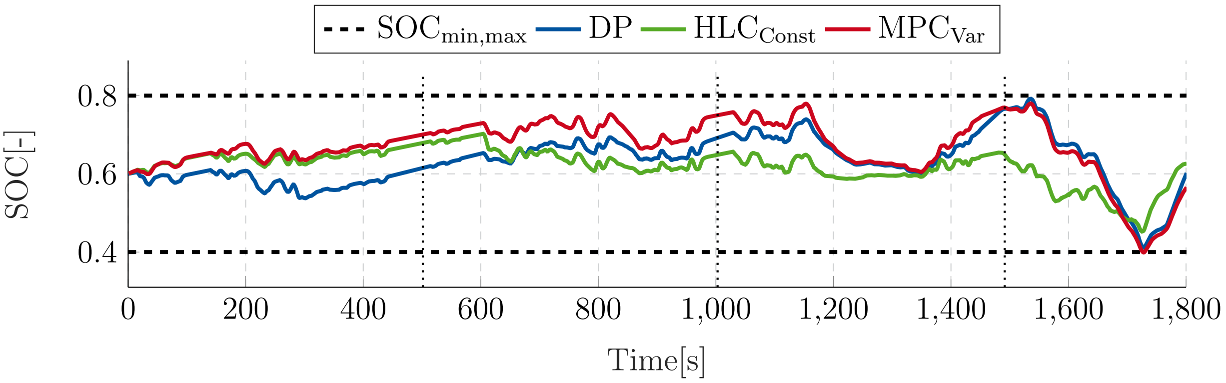

Fig. 5.5: Comparison of SOC trajectories for DP, HLC_{var} and $\text{HLC}_{\text{const}}$.

In Figure 5.6, a power histogram of the fuel cell system is illustrated in order to compare the approaches in terms of fuel cell system efficiency $\eta_{\text{fcs,bus}}$. The left y-axis depicts the fuel cell system efficiency $\eta_{\text{fcs,bus}}$ corresponding to the black line. The right y-axis presents the relative frequency of fuel cell system power use h_n referring to the colored lines. Note that the right y-axis has an interruption because of the large relative frequency for low $P_{\text{fcs,bus,ref}}$. All approaches mostly utilize the fuel cell system at minimum power $P_{\text{fcs,bus,min}}$ because the average power demand $\bar{P}_{\text{dem}}$ of 6.42 kW is low compared to $P_{\text{fcs,bus,ref,min}}$. Nevertheless, the DP and HLC$_{\text{var}}$ methods utilize the fuel cell system less frequent at $P_{\text{fcs,bus,ref,min}}$. In return, they have a larger relative frequency h_n between 4 kW and 16 kW where the efficiency $\eta_{\text{fcs,bus}}$ is higher. Additionally, only the HLC$_{\text{const}}$ method utilizes the fuel cell system extensively at high power between 42 kW and 46 kW.

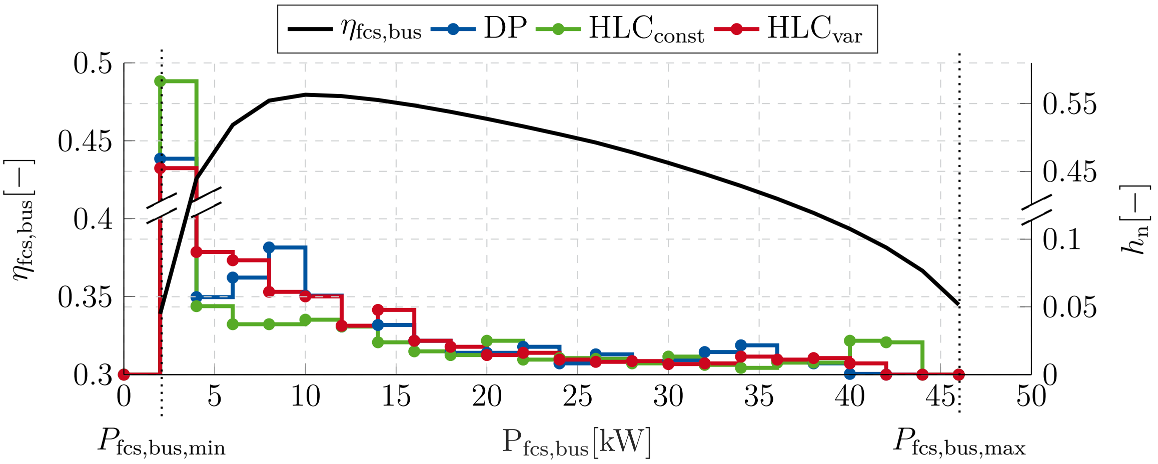

Fig. 5.6: Relative frequency of fuel cell system power compared with related fuel cell system efficiency.

In Table 5.2, the three methods are compared with each other in terms of total hydrogen consumption $m_{H_2,\text{tot}}$, equivalent hydrogen consumption $m_{H_2,\text{eq}}$ and final SOC reference SOC(T). The DP method achieves the best results in terms of $m_{H_2,\text{eq}}$ with 319.71 g. HLC$_{\text{const}}$ consumes 335.63 g which is nearly 5 % more than the DP method. HLC$_{\text{var}}$ consumes 320.33 g which is only 0.2 % worse than the global optimal solution. The calculation of $m_{H_2,\text{eq}}$ depends on the averaged component efficiencies as given in (5.3).

Tab. 5.2: Hydrogen consumption and final SOC of the three introduced methods.

	$m_{H_2,\text{tot}}$[g]	$m_{H_2,\text{tot}}[\frac{\text{kg}}{100\text{km}}]$	$m_{H_2,\text{eq}}$[g]	$m_{H_2,\text{eq}}[\frac{\text{kg}}{100\text{km}}]$	SOC(T)[−]
DP	319.71	1.35	319.71	1.35	0.6
HLC$_{\text{const}}$	338.71	1.43	335.63	1.43	0.63
HLC$_{\text{var}}$	316.84	1.34	320.33	1.36	0.57

Summing up, the objectives of the HLC mentioned in Section 4.4 are met by the HLC methods. While both HLC methods achieve good results regarding charge sustainability for the evaluated WLTC3 driving cycle, the HLC$_{\text{var}}$ method shows almost optimal results regarding the hydrogen consumption. Thus, $\mathrm{HLC_{var}}$ is a promising approach if information about the demanded power P_{dem} is available beyond the prediction horizon N_{P}^{h}. Since perfect prediction is assumed in this thesis, the method should be validated with uncertainty on the power demand prediction. It is expected that the benefit of the $\mathrm{HLC_{var}}$ compared to the $\mathrm{HLC_{const}}$ decreases but is still significant. Further investigation should be conducted on how well the method generalizes to other driving cycles.

5.3 Performance of Hierarchical Control

In this section, the hierarchical control including all levels is validated with the plant model of the FCHV on the WLTC3 scenario. In Section 5.3.1, the deviation of the hydrogen consumption m_{H_2} is compared to the results of Section 5.2. In Section 5.3.2, the tracking error of the power references are evaluated. When the HLC and the LLC work corporately, a decision inertia on the first solution as described in Section 4.4.2 is required. The necessity is demonstrated in Section 5.3.3 by presenting the results when it is not utilized.

5.3.1 Deviation of Predicted Trajectory

In this section, the deviation of the hierarchical control from the trajectory that is predicted, when only $\mathrm{HLC_{var}}$ is utilized, is validated. The deviation is caused by modeling mismatches between the prediction model of the control and the plant model. As introduced in Chapter 3, model mismatches are caused, e.g., by negligence of the air humidity and estimation of the compressor map.

Table 5.3 presents the deviation between the hydrogen consumption of the complete hierarchical control compared and the results of the $\mathrm{HLC_{var}}$. The total hydrogen consumption $m_{H_2,\mathrm{tot}}$ and the equivalent hydrogen consumption $m_{H_2,\mathrm{eq}}$ raise by about $1\,\%$ caused by the modeling errors. Furthermore, the $\mathrm{HLC_{var}}$ only considers a static model of the fuel cell system even though the power consumption of the compressor deviates during transient operation. Consequently, the SOC also deviates from the results of the $\mathrm{HLC_{var}}$. While $\mathrm{HLC_{var}}$ ends with a final $\mathrm{SOC}(T)$ of 0.57, the hierarchical control ends with a final $\mathrm{SOC}(T)$ of 0.56.

In Figure 5.7a, the SOC trajectories of the HLC and the hierarchical control are compared. Both controllers follow a similar trajectory for the whole driving cycle. In order to illustrate it, the error $\mathrm{SOC_{err}}$ is presented in Figure 5.7b. The absolute error always stays below 0.01.

The operating points of the compressor in the plant model are illustrated in Figure 5.8. Since the controllers are tested with a constant stack temperature T_{st} and robustification

Tab. 5.3: Hydrogen consumption and final SOC reference for $\mathrm{HLC_{var}}$ and entire hierarchical control.

	$m_{H_2,\mathrm{tot}}$[g]	$m_{H_2,\mathrm{eq}}$[g]	SOC(T)[−]
$\mathrm{HLC_{var}}$ only	318.04	321.40	0.57
$\mathrm{HLC_{var}}$+ILC+LLC	320.73	324.72	0.56
Deviation	+0.84 %	+1.03 %	−0.73 %

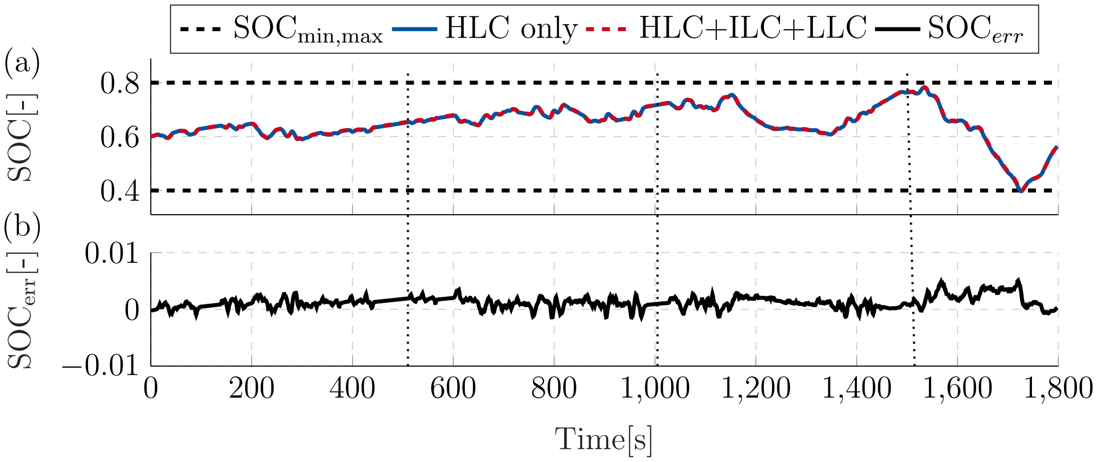

Fig. 5.7: SOC trajectory of $\mathrm{HLC_{var}}$ compared with entire hierarchical control.

factor $\dot{m}_{\mathrm{rob}}$, the optimal operating line calculated by the ILC is illustrated by the blue line. The operating points of the compressor are marked with a sampling time of 100 ms by the green crosses. The deviation from the optimal line is small especially for high corrected air mass flow rate $\dot{m}_{\mathrm{cr}}$ because the WLTC3 driving cycle does not require strong acceleration or deceleration. Therefore, the compressor has no large operating point changes. The operating points of the compressor stay within the given surge and choke boundary.

5.3.2 Tracking Error

Another objective of the hierarchical control is to ensure a dynamic power delivery. When model mismatches are included, the MPC inherently leads to an undesired offset. Therefore, the LLC includes a disturbance observer that is supposed to compensate for those model mismatches.

Figure 5.9 illustrates the tracking errors over the whole driving cycle. In Figure 5.9a, the power demand P_{dem} is given to illustrate the speed phases of the WLTC3. Subsequently, the tracking error of the delivered power $P_{\mathrm{del,err}}$, the fuel cell system power $P_{\mathrm{fcs,bus,err}}$ and the battery power $P_{\mathrm{bat,bus,err}}$ are given in Figures 5.9(b-d) respectively. The LLC including the disturbance observer is given in blue and the LLC without disturbance observer is

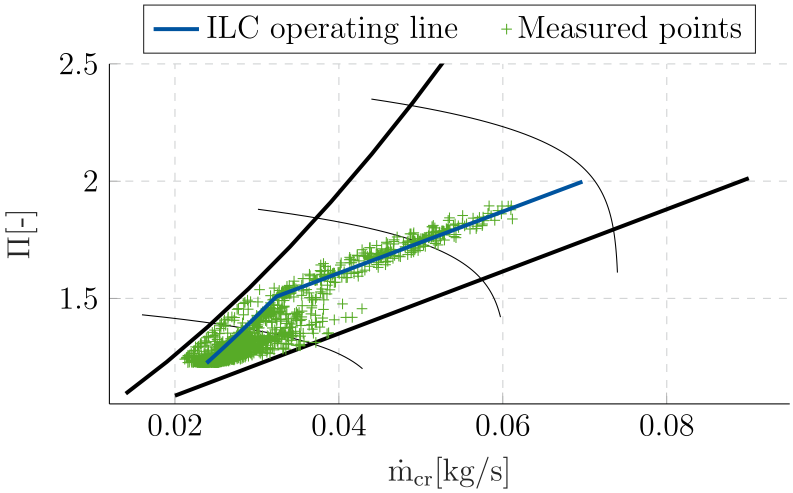

Fig. 5.8: ILC operating line and measured operating points in compressor map.

presented in red.

The disturbance observer improves the tracking error for all power trajectories. The peaks are due to steps of P_{dem} and always stay below 1 kW. The root mean square error (RMSE) of the delivered power P_{del} is reduced from 0.26 kW to 0.24 kW by the disturbance observer. There are two reasons for the low improvement of the RMSE. Firstly, the disturbance observer can only diminish the offset but not the transient error. Thus, the peaks are still present and might even increase due to the deadbeat behavior of the chosen disturbance observer.

Moreover, an undesirable offset error of $P_{\mathrm{fcs,bus,err}}$ can be observed in Figure 5.9c. While the LLC without disturbance observer has an expected offset error, even the LLC with disturbance observer shows an offset error. A possible explanation for this behavior is a wrong prediction of the HLC caused by modeling errors. This is further examined in Section 5.4.3. Nonetheless, the RMSE of the fuel cell system is decreased from 0.22 kW without disturbance observer to 0.20 kW.

The RMSE of $P_{\mathrm{bat,bus,err}}$ is decreased from 0.11 kW to 0.07 kW by the disturbance observer. The reason that the RMSE is not even lower is that the battery compensates for the offset error of $P_{\mathrm{fcs,bus,err}}$ based on the weightings of $q_{P_{\mathrm{del}}}$ and $q_{P_{\mathrm{bat,bus}}}$ in the LLC. This can be validated by setting $q_{P_{\mathrm{del}}}$ to zero such that $P_{\mathrm{FC,bus}}$ and $P_{\mathrm{bat,bus}}$ are not coupled. In this case, the offset error of $P_{\mathrm{bat,bus}}$ diminishes.

Overall, the tracking error of the hierarchical control is below 1 kW at any time and it has no large influence on the overall system behavior.

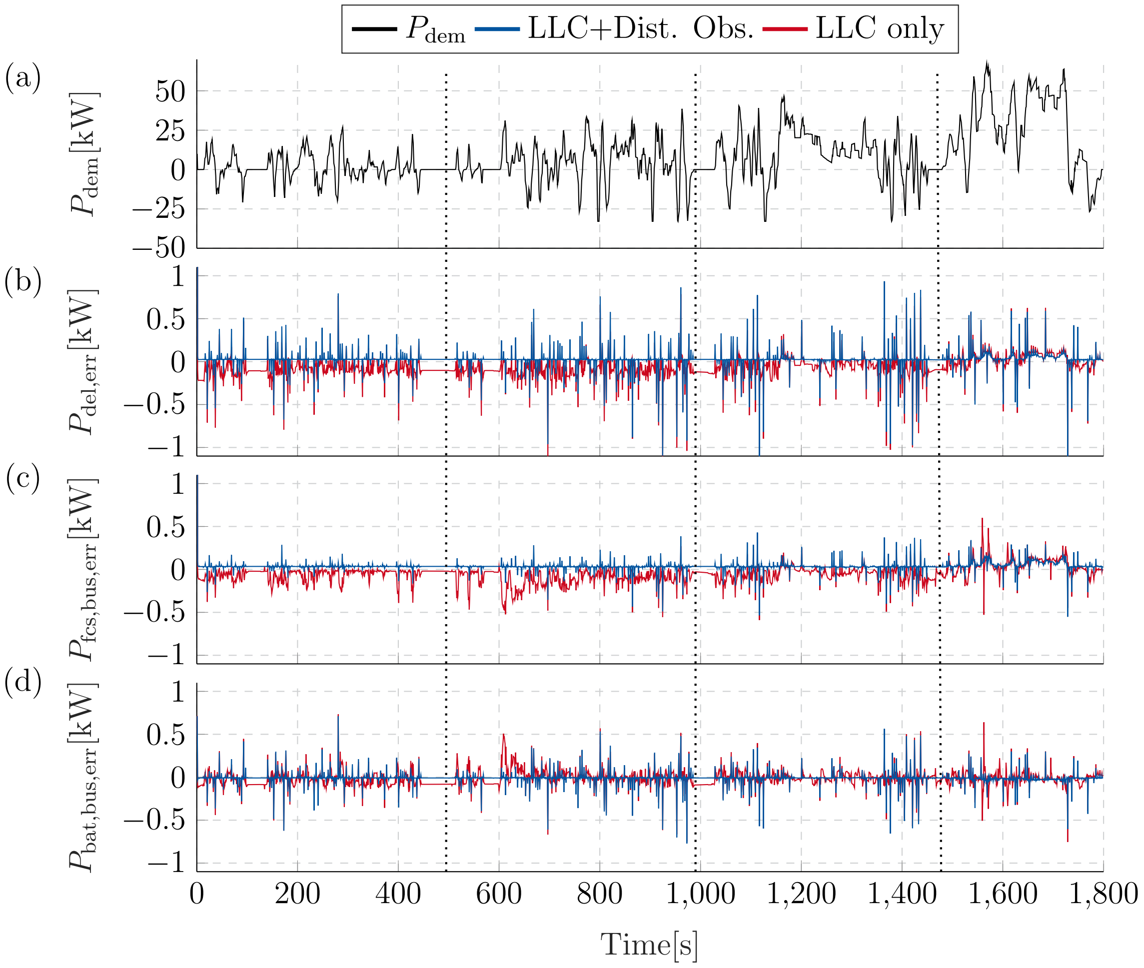

Fig. 5.9: Tracking error of power values with and without disturbance observer.

5.3.3 Decision Inertia on First Solution of High-Level Control

The NMPC of the HLC penalizes the inertia of the first solution of $P_{\text{fcs,bus,ref,0}}$ at time step k to the second solution of $P_{\text{fcs,bus,ref,1,last}}$ at time step $k-1$. This is necessary in corporation with the LLC because the LLC might otherwise prepare for a power step that finally does not occur. In this section, the implementation of the decision inertia is motivated by illustrating the impacts of not using it.

In Figure 5.10, the reason for the decision inertia is illustrated at the WLTC3 driving cycle from 18 s to 22 s. For demonstration purposes, the penalization weight $q_{\text{PfC,0}}$ of the HLC as described in (4.38) is set to 0. In Figure 5.10a, the delivered power P_{del} is illustrated and follows the reference power P_{dem} with minimal lag and delay. In Figures 5.10b and 5.10c, the power split between $P_{\text{fcs,bus,ref}}$ and $P_{\text{bat,bus,ref}}$ is presented. The red, green and orange dotted lines illustrate the reference values from the HLC for the subsequent 2 s starting at 18 s, 19 s and 20 s respectively. The black dashed lines depict the resulting reference values for the LLC that are interpolated by a sigmoid function (compare Section 4.2.1).

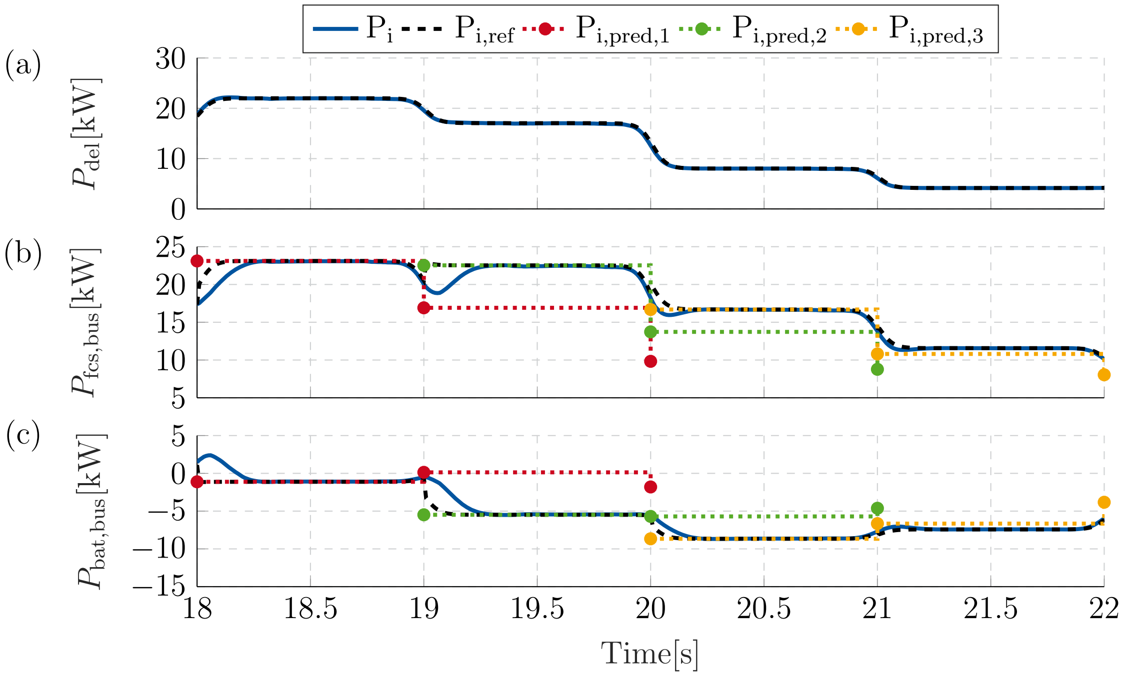

Fig. 5.10: Illustration of impact when HLC runs without decision inertia.

The HLC without decision inertia leads to an unwanted behavior of the power steps. The problems appear most strongly at 19 s. The prediction of the HLC executed at 18 s $\mathrm{P}_{\mathrm{i,pred,1}}$ predicts a power step from 23 kW to 17 kW at 19 s. As soon as the power step occurs in the prediction horizon of the LLC, the controller starts preparing for the power step. However, the new prediction of the HLC $\mathrm{P}_{\mathrm{i,pred,2}}$ is passed to the LLC at 19 s and puts out a reference power of 23 kW. This leads to the unwanted behavior in the power split. The delivered power P_{del} is not affected because only the power split between the fuel cell system and the battery changes. This problem is approached by the decision inertia on the first solution of $P_{\mathrm{fcs,bus,ref,0}}$. Thus, the problem does not occur in the remaining of this thesis.

Summing up the performance evaluation of the hierarchical control, it can be stated that the hierarchical control levels can work corporately. The predicted equivalent hydrogen consumption of the HLC is followed with only 1.03 % deviation. Furthermore, the final SOC(T) only deviates by 0.73 %. Those results can be achieved because the LLC is capable of following the references of the higher level with high accuracy. Finally, it has been shown that in order to work corporately, a decision inertia in the HLC is required to prevent undesired power switching between the battery and the fuel cell system.

5.4 Low-Level Control Evaluation

As mentioned in Section 4.2, the objectives of the LLC include the dynamic power split, tracking the hydrogen optimized reference points, complying with system constraints and avoiding excessive actuator changes. In this section, the LLC and the ILC are evaluated without considering the HLC. Since the dynamics of the WLTC3 driving cycle are too slow to illustrate the capabilities of the LLC, the short time scale scenario illustrated in Figure 5.11 is chosen. At 2 s, the driver demands a power step from 2 kW to 50 kW before doing the reverse power step at 5 s. In Section 5.4.1, the control is validated with and without predictive information of the power demand P_{dem}. In Section 5.4.2, the influence of the robustification factor $\dot{m}_{\mathrm{rob}}$ is investigated. The evaluation indicates open points of the LLC under the influence of modeling errors. In Section 5.4.3 these open points are illustrated utilizing the LLC predictions. Furthermore, possible solutions are proposed.

5.4.1 Performance under Uncertain Power Demands

In order to illustrate the performance of the LLC, several figures are presented including the resulting power trajectories of each component, the oxygen excess ratio, the control inputs and the trajectories in the compressor map. In all cases, the LLC is evaluated with prediction (in blue) and without prediction (in red).

In Figure 5.11, the power split of the components is illustrated. The delivered power P_{del} is presented in Figure 5.11a, the fuel cell system power $P_{\mathrm{fcs,bus}}$ in Figure 5.11b and the battery power $P_{\mathrm{bat,bus}}$ in Figure 5.11c. When the prediction is known, P_{del} as well as $P_{\mathrm{fcs,bus}}$ and $P_{\mathrm{bat,bus}}$ follow the reference values precisely. Without prediction, the controller only knows about the power steps as soon as they occur (marked by the black dotted lines). This leads to an expected delay of the delivered power P_{del}. Furthermore, it can be observed that $P_{\mathrm{fcs,bus}}$ cannot follow as fast as desired. The reason is that the compressor operates at the choke and surge boundaries in those cases. Therefore, $P_{\mathrm{bat,bus}}$ has an overshoot during transient operation in order to compensate for the delay of $P_{\mathrm{fcs,bus}}$.

In Figure 5.12a, the oxygen excess ratio λ_{O_2} is illustrated. The dashed black lines represent the minimum oxygen excess ratio of the ILC $\lambda^{i}_{O_2,\mathrm{min}}$ and the minimum oxygen excess ratio of the LLC $\lambda^{l}_{O_2,\mathrm{min}}$. For low $P_{\mathrm{fcs,bus}}$, λ_{O_2} is above 10. The reason is that the corrected air mass flow rate $\dot{m}_{\mathrm{cr}}$ cannot be further decreased due to the surge boundary. The high values for λ_{O_2} are not a problem in this thesis but should be further examined when it comes to controlling the relative air humidity [40].

Between 2 s and 5 s, the oxygen excess ratio λ_{O_2} is close to its minimum value $\lambda^{l}_{O_2,\mathrm{min}}$. Thus, a zoom-in graph is illustrated in Figure 5.12b. When the first power step at 2 s occurs, the controller operates at the minimal oxygen excess ratio $\lambda^{l}_{O_2,\mathrm{min}}$ with and without prediction. Nonetheless, the controller with predictive information only operates for a few milliseconds

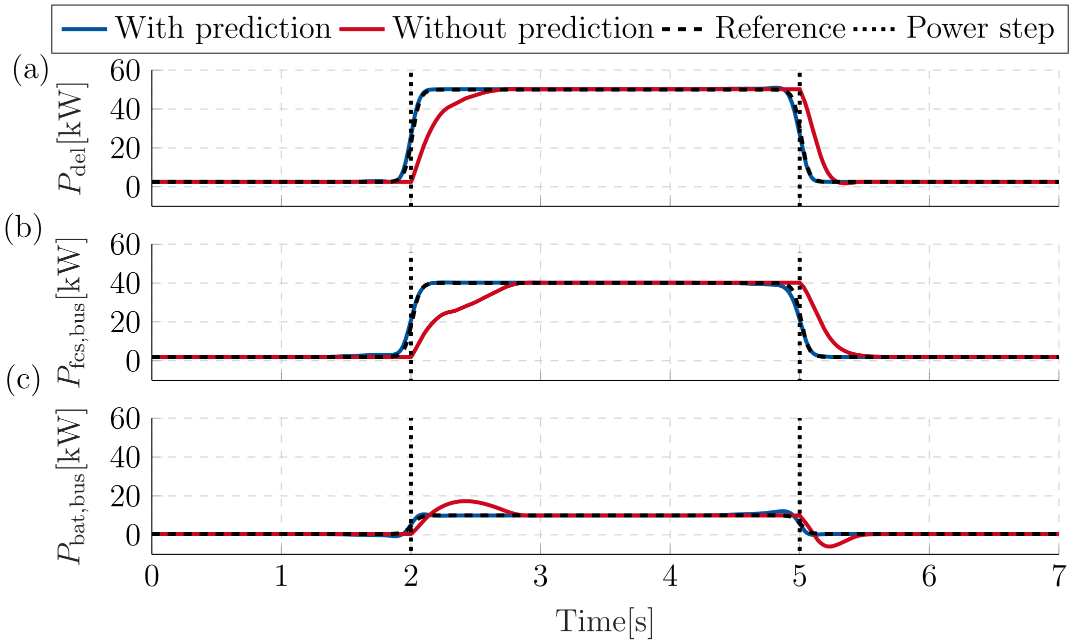

Fig. 5.11: Power split between battery and fuel cell system with and without LLC prediction.

at the boundary, while the controller without predictive information operates half a second at the boundary. In steady-state both controllers converge to an oxygen excess ratio above $\lambda^i_{O_2,\text{min}}$. When the second power step at 5 s occurs, λ_{O_2} shows an overshoot in both cases because the compressor operates at the surge boundary and cannot decrease $\dot{m}_{\text{cr}}$ rapidly. The overshoot is expected because λ_{O_2} is not restricted to a maximum value.

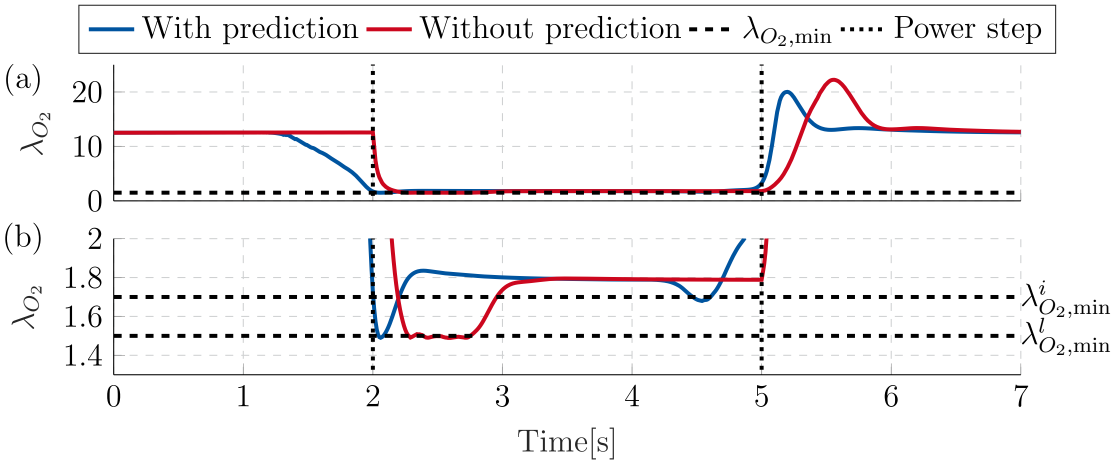

Fig. 5.12: Oxygen excess ratio including zoom-in graph with and without LLC prediction.

In Figure 5.13, the control inputs $\mathbf{u}^l$ of the LLC are presented. The stack current I_{st}, the compressor motor voltage U_{cm}, the back pressure valve opening position h_{om} and the battery current I_{bat} in Figures 5.13(a-d) respectively. The controller including predictive information prepares for the power steps. For the first power step at 2 s, U_{cm} is predictively increased to its final set point in order to overcome the motor inertia J_{cm}. h_{om} is lowered in order to raise the pressure ratio Π without violating the choke boundary. Since U_{cm} is increased predictively, I_{st} has to be increased as well in order compensate for the raising electrical power consumption of the motor P_{cm}.

The controller including prediction also prepares for the second power step at 5 s. In order to release pressure from the system, h_{om} is increased to its maximum and U_{cm} is decreased. Thus, I_{st} is decreased as well. One ought to observe that h_{om} is oscillating when it is operated at the maximum opening position. In this case, the compressor additionally operates at the choke boundary. Due to the large penalization term c_{min} of the LLC, the mathematical conditioning of the augmented Lagrangian method is low which causes the oscillating behavior.

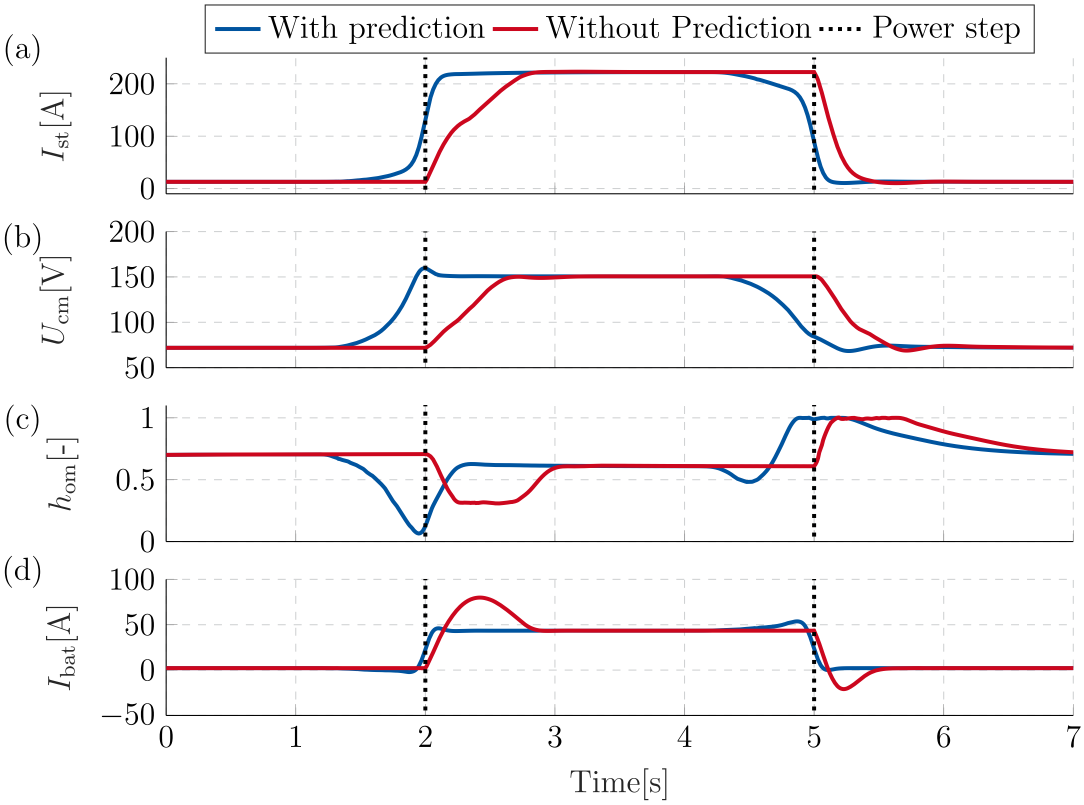

Fig. 5.13: Control inputs of battery and fuel cell system with and without LLC prediction.

The controller without predictive information reacts differently to the power steps. Firstly, it cannot prepare for the steps and thus starts manipulating the control inputs $\mathbf{u}^l$ after the power steps occur. As soon as the controller senses the first power step, it decreases h_{om} and increases U_{cm}. However, the compressor is restricted to the choke boundary and thus cannot increase pressure ratio Π and air mass flow rate m_{cr} rapidly. Due to the limitation of the oxygen excess ratio λ_{O_2}, I_{st} cannot increase rapidly as well. Caused by the dynamic power split objective of the LLC, I_{bat} shows a strong overshoot at 2.5 s which improves the dynamic power delivery of P_{del}.

When the second power step is sensed, h_{om} is increased to its maximum value rapidly and U_{cm} is decreased. Nonetheless, the dynamic is constrained by the surge boundary in this case. Therefore, I_{bat} shows an undershoot.

In Figure 5.14, the trajectory in the compressor map is illustrated with and without predictive information. Both trajectories cover a wide range of the compressor map because the power steps of the chosen scenario are large. Therefore, the compressor needs to operate at the surge and choke boundary during both power steps. Indicated by the time stamps, it is illustrated that the trajectory with prediction is always ahead of the trajectory without prediction. Both trajectories violate the surge boundary for the second power step. This is caused by modeling errors and is further investigated in Section 5.4.3.

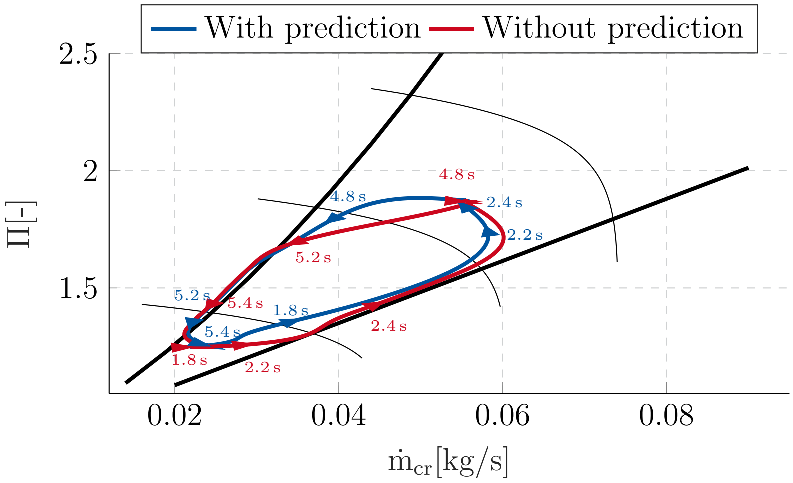

Fig. 5.14: Trajectory in compressor map during power steps with and without LLC prediction.

5.4.2 Influence of Robustification Factor

In this section, the influence of the robustification factor $\dot{m}_{\mathrm{rob}}$ on the dynamic power delivery and the hydrogen consumption minimization is examined. The LLC scenario is simulated without predictive information for robustification factors of 20 g/s (in blue) and 40 g/s (in red). The delivered power P_{del} is presented in Figure 5.15a, the fuel cell system power $P_{\mathrm{fcs,bus}}$ in Figure 5.15b and the battery power $P_{\mathrm{bat,bus}}$ in Figure 5.15c.

For both robustification factors $\dot{m}_{\mathrm{rob}}$, the delivered power P_{del} is almost identical. However, the power split between the fuel cell system and the battery differs. If the robustification factor $\dot{m}_{\mathrm{rob}}$ is larger, the unpredicted first power step can be followed with less delay. Due to the constraint of the minimum oxygen excess ratio $\lambda^{l}_{O_2,\mathrm{min}}$, the corrected air mass flow rate $\dot{m}_{\mathrm{cr}}$ has to increase rapidly but it cannot be achieved if the compressor operates at the choke boundary. With increasing robustification factor $\dot{m}_{\mathrm{rob}}$, the compressor does not operate at the choke boundary as fast because the steady-state distance to the choke boundary is larger. Consequently, the controller with the smaller robustification factor $\dot{m}_{\mathrm{cr}}$ has to utilize the battery more during transient operation. The second power step is almost identical for both cases. The reason is that the controller is not restricted by a maximum oxygen excess ratio and thus shows an overshoot (compare Figure 5.12).

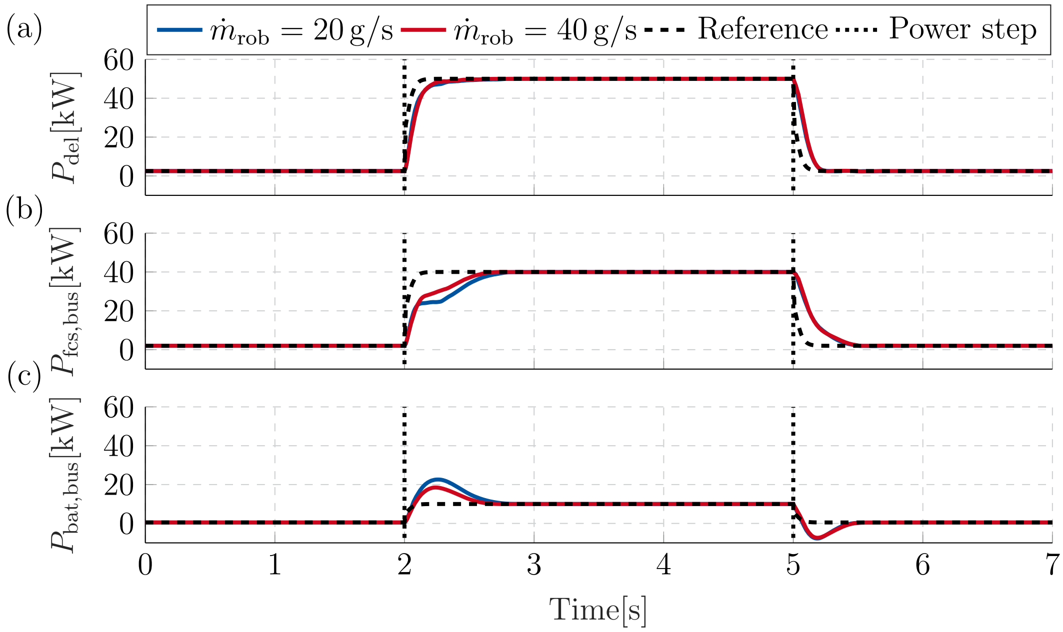

Fig. 5.15: Influence of robustification factor on power split.

In Figure 5.16, the resulting trajectories in the compressor map are illustrated. When the robustification factor $\dot{m}_{\mathrm{rob}}$ is increased, the controller operates at higher pressure ratio Π and corrected air mass flow rate $\dot{m}_{\mathrm{cr}}$. This leads to the advantage that the distance to the choke boundary is larger. The controller with smaller robustification factor $\dot{m}_{\mathrm{rob}}$ reaches the choke boundary faster while the controller with larger $\dot{m}_{\mathrm{rob}}$ prolongs the curve. For the second power step, both controllers behave similarly. However, in both cases the surge boundary is violated. An explanation for this behavior is given in Section 5.4.3.

Overall, the impression arises that an increased robustification factor $\dot{m}_{\mathrm{rob}}$ comes with a low benefit. The only advantage is that the battery is utilized less during transient operation of a large increasing power step and the compressor operates shorter at the choke boundary. However, also the hydrogen consumption raises only by 5 % from 3.86 g to 4.03 g for the LLC scenario due to the increased electrical power consumption of the compressor. Therefore, it might be beneficial to increase $\dot{m}_{\mathrm{rob}}$, when the power demand prediction is uncertain (e.g. urban environment) and to decrease it when the prediction is certain.

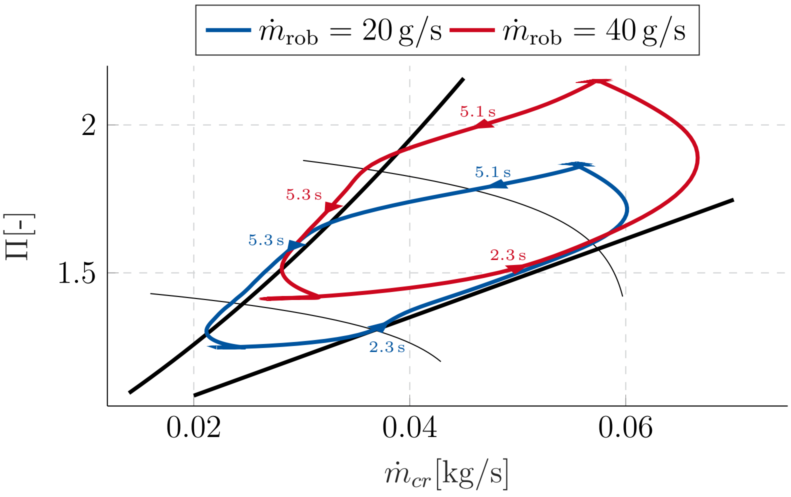

Fig. 5.16: Influence of robustification factor on compressor trajectory.

5.4.3 Influence of Modeling Errors

Analyzing the control performance of the LLC, two open points were pointed out. Firstly, despite the use of a disturbance observer, an offset in the fuel cell system power $P_{\mathrm{fcs,bus}}$ can be observed and secondly the surge boundary is violated for large increasing power steps. When the controller is tested on the prediction model of the LLC, both problems do not occur meaning that they are caused by the influence of modeling errors. In this section, possible explanations for both open points are illustrated based on the controller prediction and possible solutions are discussed.

For the prediction model of LLC, relative air humidity is neglected in Chapter 3. This results in an underestimate of the pressure values. In Figure 5.17, the compressor trajectories (in blue) with (a) and without (b) relative air humidity in the plant model are demonstrated. When the relative air humidity is set to 0 % in the plant model, the compressor does not violate the choke boundary. Furthermore, the controller prediction (in green) is accurate. When the air humidity is set to a desired value of 80 % in the plant model, the prediction quality decreases noticeably. During the violation of the choke boundary, the controller gives a high penalization and the prediction illustrates that the controller tries to stay within the feasible region. Nonetheless, due to the imprecise prediction model, the controller does not achieve it.

In order to approach this problem, two concepts are recommended. Firstly, relative air humidity can be considered in the prediction model [70]. Secondly, the boundary can be robustified by reducing the feasible region of the compressor map. This will lead to a loss of performance but ensures compliance with the constraints.

The second open point occurs for the offset-free tracking of the fuel cell system power $P_{\mathrm{fcs,bus}}$. Despite the use of a disturbance observer, an offset in the power tracking remains.

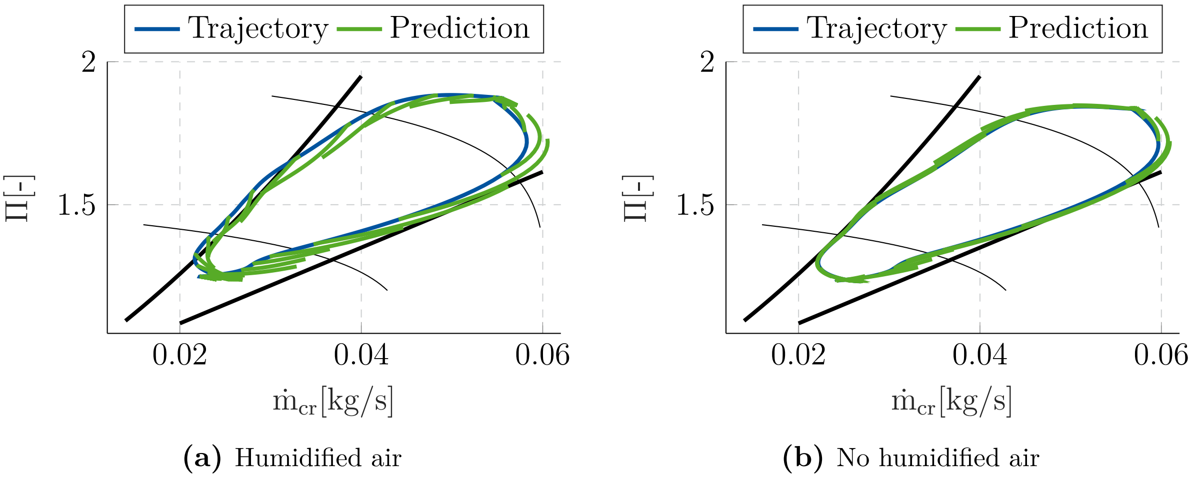

(a) Humidified air

(b) No humidified air

Fig. 5.17: Trajectory and LLC prediction in the compressor map with and without humidified air.

Figure 5.18 illustrates the problem for the LLC scenario between 3 s and 4 s where the system is supposed to be at steady-state. $P_{\mathrm{fcs,bus}}$ stays below the reference power $P_{\mathrm{fcs,bus,ref}}$ with an offset of 0.022 kW. The controller prediction, however, is similar for each time step and the controller assumes that it will reach the reference. The same behavior occurs for the other tracking values of the fuel cell system Π and $\dot{m}_{\mathrm{cr}}$. However, it gives the wrong inputs to the model due to modeling errors.

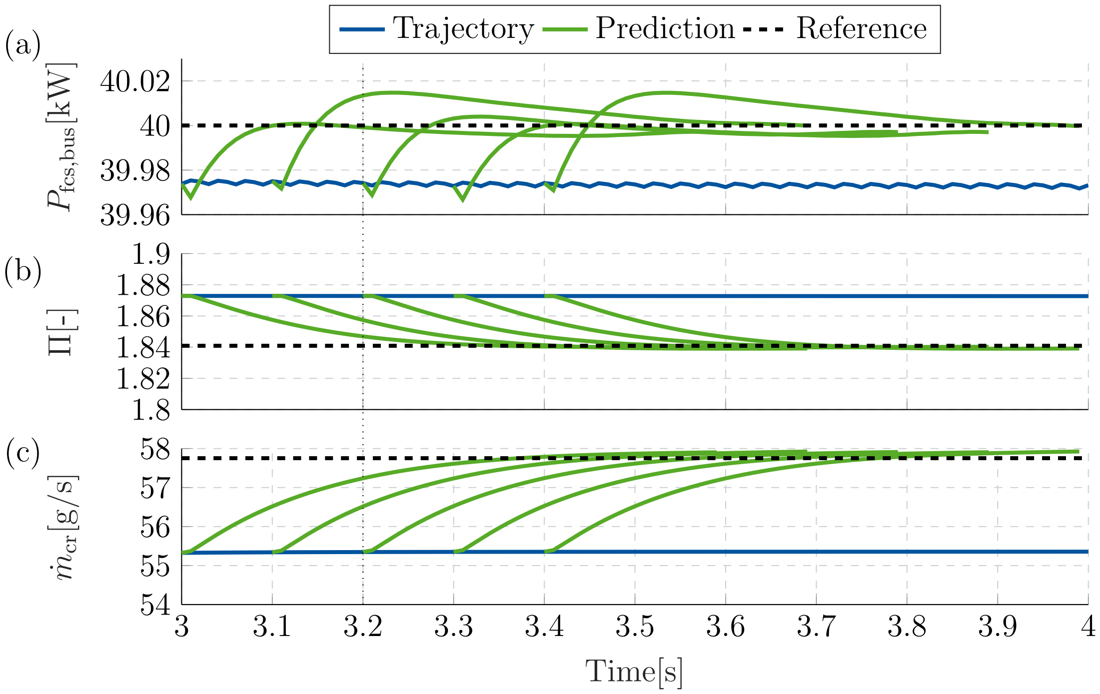

Fig. 5.18: Zoom-in graph of trajectory and LLC prediction for tracked references of the fuel cell system.

In Figure 5.19, the scaled control inputs $\Delta\mathbf{u}$ are presented for the prediction at 3.2 s (indicated by the dotted black line in Figure 5.18). $\Delta\mathbf{u}$ is nearly zero for the first control input $\Delta\mathbf{u}_0$ so that it has reached steady-state. However, it does not stay at zero during the control horizon because it has not yet reached the reference values. This phenomena only occurs under the influence of modeling errors.

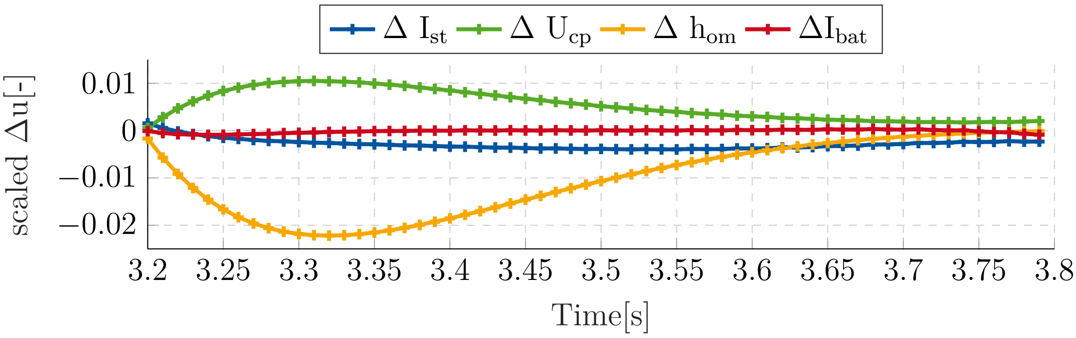

Fig. 5.19: Prediction of input derivatives at 3.2 s.

Even though, the offset is small for all tracked variables, it should be further investigated why this offset may occur. Eventually, the optimization is stuck in a local optimum of the optimization. This can be approached by varying weighting matrix R^l over the prediction horizon.

Summing up the results of the LLC, the objectives related to the LLC are fulfilled. The reference points which are received from the higher levels are tracked precisely. Even though the offset is not reduced to zero, the remaining steady-state error is negligible for automotive applications. It has been shown that the LLC can deal with uncertain power demands utilizing a dynamic power split. In this case, the battery is used to compensate for the limited dynamics of the fuel cell system. In case that the power demand prediction is available to the LLC, it can predictively prepare the fuel cell system for the upcoming power step and follows the reference trajectories with minimal lag and delay. Despite large decreasing power steps, the controller complies with almost all constraints. In order to prevent violating the surge boundary, two solution have been proposed. Either the constraints can be robustified or the accuracy the prediction model can be enhanced. Finally, the controller avoids excessive actuator changes due to the penalization of the control input derivatives. The LLC and the ILC have also successfully been tested on the dSPACE MicroAutoBox II.

6 Conclusion and Outlook

Conclusion

The work presented in this thesis is motivated by the attempt to develop a power management for an FCHV. This involves the objectives of dynamic power delivery, charge sustainability of the battery, hydrogen consumption minimization as well as compliance with system constraints. For these purposes, a hierarchical MPC was proposed which comprises three levels in order to deal with the objectives on different time scales. The entire hierarchical control was validated on a detailed model of the FCHV using the WLTC driving cycle.

The high-level control (HLC) was designed to find the optimal power split between the battery and the fuel cell system. In doing so, it handles the large time constants of the propulsion system. Therefore, an NMPC based on a direct method was implemented within this thesis. The prediction model comprises a steady-state model of the fuel cell system and only considers for the dynamics of the battery SOC. The evaluation pointed out that the NMPC with constant final SOC reference suffers from the lack of information about the power demand beyond the prediction horizon. Consequently, a modification was proposed that adapts the final SOC reference according to an offline optimization of the driving cycle. Assuming perfect power demand prediction, the hydrogen consumption is decreased by 5 % compared to the NMPC with constant final SOC reference. Moreover, it only deviates by 0.2 % from the optimal solution which is attained by dynamic programming.

The intermediate-level control (ILC) was designed to find the optimal operating point of the air supply utilizing a static optimization. It was demonstrated that the optimal operating point should not only be chosen in regard to hydrogen consumption but also in regard to robustness towards uncertain power demands. For that reason, a robustification factor was introduced which improves the dynamic power delivery of the fuel cell system but at the same time leads to an increased hydrogen consumption.

The low-level control (LLC) was designed to track reference trajectories received from the HLC and the ILC. Hence, it needs to deal with the small time constants of the propulsion system. The control was implemented using an NMPC with the toolbox GRAMPC. The prediction model includes an accurate model of the fuel cell system including dynamics of the air supply. In order to speed up the computation time, the required derivatives were calculated by algorithmic differentiation. Despite the short sampling time of 10 ms, the NMPC was successfully tested on a dSpace MicroAutoBox II. The LLC implemented in this thesis manages to track the reference trajectories with minimal lag and delay due to the predictive behavior and inherent decoupling capability of an MPC. Moreover, it complies with the system constraints caused by the limited operating range of the compressor and the prevention of oxygen starvation. The control is even capable to fulfill the objectives under uncertain power demand predictions by deviating from the reference trajectories to relieve the fuel cell system when operating under system constraints.

It was demonstrated within this thesis that the control levels can operate corporately. In doing so, a decision inertia on the HLC is required such the LLC can handle the received reference trajectories. The deviation between the entire hierarchical control and the HLC prediction is only 1.03 % in terms of equivalent hydrogen consumption and below 1 % in terms of the predicted SOC trajectory.

In summary, the proposed hierarchical MPC is capable of dealing with the challenges that come with the power management of an FCHV. It manages to provide a dynamic power delivery and to comply with the system constraints. Furthermore, the control takes advantage of the redundancy of the propulsion system by choosing the operating point such that minimum hydrogen consumption and charge sustainability of the battery is achieved.

Outlook

The evaluation of the HLC identified that the fuel cell system often operates at its minimum power. This indicates a potential for further improvement by applying start-stop strategies. Considering these strategies leads to binary variables in the optimal control problem that cannot be treated by the presented NMPC. The optimization problem can be solved by e.g. stochastic dynamic programming or mixed-integer programming [55, 77, 78]. Alternatively, heuristic approaches can handle start-stop decisions [79]. In general, the control should avoid frequent start-stop switching in order to prevent fuel cell degradation.

The HLC is evaluated based on perfect predictive information. The behavior and optimality of the hierarchical control with uncertain power demand prediction can be further investigated. Several approaches for power demand prediction based on measurement data and navigation systems exist [55, 73, 80].

In this thesis, perfect state measurements are assumed which is not applicable to real-world scenarios. A nonlinear state estimator such as an extended Kalman filter, unscented Kalman filter or sequential Monte Carlo filter is required [68, 69]. Measurement values that are available for the state estimation consist of pressure, air mass flow rates and temperature in the inlet and outlet manifold [68].

Another essential objective that should be taken into account by the hierarchical control scheme is air humidification. The relative air humidity in the cathode must be carefully regulated in order to prevent the fuel cell from flooding or dehydration. The compressor has a large influence on the control, since the dew point of air depends on the system pressure and temperature [3, 35, 41]. Therefore, it is suggested to consider air humidification in the operating point optimization of the ILC. Moreover, the extent to which air humidification restricts the dynamic power delivery of the fuel cell system should be investigated.

A Appendix

A.1 Fuel Cell Hybrid Vehicle Parameter

Tab. A.1: Vehicle parameter

Parameter	Symbol	Value
Vehicle mass	m_{vec}	$1925\,\text{kg}$
Drag coefficient	c_w	0.29
Reference area	A_{vec}	$2.26\,\text{m}^2$
Rolling resistance coefficient	f_{R}	0.007
Moment of inertia	Θ_{vec}	$3.6\,\text{kg}\,\text{m}^2$
Electric motor efficiency	η_{mot}	0.95
Gear efficiency	η_{gear}	0.97

Tab. A.2: Parameters of fuel cell electrochemistry

Parameter	Description	Value
Activation loss parameters	ξ_1	$-0.93\,\text{V}$
	ξ_{2a}	$2.86 \times 10^{-3}\,\text{V/K}$
	ξ_{2b}	$2 \times 10^{-4}\,\text{V/K}$
	ξ_{2c}	$4.3 \times 10^{-5}\,\text{V/K}$
	ξ_3	$1.0 \times 10^{-6}\,\text{V/K}$
	ξ_4	$-1.9 \times 10^{-4}\,\text{1/K}$
Active cell area	A_{cell}	$280\,\text{cm}^2$
Concentration loss parameters	m_{conc}	$-0.0103\,\text{1/A}$
	n_{conc}	$0.0059\,\text{V}$
Membrane water content	λ_M	12.5
Membrane thickness	δ_M	$2\,\text{mm}$
Number of elementary cells	$n_{\text{fc,cell}}$	381

Tab. A.3: Parameters of air supply

Parameter	Description	Value
Manifold volumes	V_{im}	$0.02\,\mathrm{m}^3$
	V_{cat}	$0.0053\,\mathrm{m}^3$
	V_{om}	$0.005\,\mathrm{m}^3$
Linearized flow constants	$k_{\mathrm{cat,in}}$	$0.0036\,\mathrm{g/(Pas)}$
	$k_{\mathrm{cat,out}}$	$0.0021\,\mathrm{g/(Pas)}$
Nozzle parameters	C_{d}	0.0124
	A_{t}	$1\,\mathrm{cm}^2$
Compressor parameters	J_{cm}	$0.05\,\mathrm{g/m}^2$
	η_{cm}	0.98
	k_{T}	$0.0153\,\mathrm{Nm/A}$
	R_{cm}	$0.816\,\Omega$

Tab. A.4: Parameters of battery

Parameter	Description	Value
Battery storage capacity	Q	$6.5\,\mathrm{A\,h}$
Number of packs in battery	n_{packs}	34
Number of cells per pack	$n_{\mathrm{bat,cell}}$	6
Exponential zone amplitude	A	$111\,\mathrm{mV}$
Exponential zone time constant inverse	B	$2.3\,1/\mathrm{Ah}$
Internal resistance	R_i	$2\,\mathrm{m\Omega}$
Polarization constant	K	$9.1\,\mathrm{mV}$
Constant voltage	E_0	$1.28\,\mathrm{V}$

A.2 Control Parameter

Tab. A.5: Parameters of the high-level control.

Parameter	**Symbol**	**Value**
Sampling Time	T_S^{h}	1 s
Control horizon	N_{C}^{h}	Same as N_{P}^{h}
Prediction horizon	N_{P}^{h}	Investigated in Chapter 5
SOC reference	$SOC_{\mathrm{ref}}(N_{\mathrm{P}}^{h})$	Investigated in Chapter 5
Cost weights	q_{SOC}	Investigated in Chapter 5
	$q_{P_{\mathrm{lhv}}}$	0.001
	$q_{S,P_{\mathrm{fcs}}}$	10000
	$q_{S,SOC}$	10000
	$q_{P_{\mathrm{fcs},0}}$	1
	$r_{P_{\mathrm{fcs}}}$	0.0001
	$r_{P_{\mathrm{bat}}}$	0.0001
System constraints	$P_{\mathrm{fcs,bus,ref,min}}$	2 kW
	$P_{\mathrm{fcs,bus,ref,max}}$	42 kW to 46 kW (depends on T_{st})
	$P_{\mathrm{bat,bus,ref,min}}$	−35 kW
	$P_{\mathrm{bat,bus,ref,max}}$	35 kW
	SOC_{min}	0.4
	SOC_{max}	0.8

Tab. A.6: Parameter of the intermediate-level control.

Parameter	**Symbol**	**Value**
Constraints	$\lambda_{O_2,\mathrm{min}}^{i}$	1.7
	Π_{rob}	0.15
	$\dot{m}_{\mathrm{rob}}$	Investigated in Chapter 5
Offline lookup table ranges	T_{st}	20 °C to 90 °C
	$\dot{m}_{\mathrm{rob}}$	0 g/s to 40 g/s
	$P_{\mathrm{fcs,bus}}$	2 kW to 50 kW (dependent on T_{st})

Tab. A.7: Parameters of the low-level control.

Parameter	**Symbol**	**Value**
Sampling Time	T_S^l	10 ms
Control horizon	N_C^l	80
Prediction horizon	N_P^l	80
Weights on reference tracking	q_{P_del}	0.1
	$q_{P_\mathrm{fcs,bus}}$	0.03
	$q_{P_\mathrm{bat,bus}}$	0.01
	$q_{\dot{m}_\mathrm{cr}}$	200
	q_Π	100
Weights on actuator changes	r_{I_st}	0.01
	r_{U_cp}	0.01
	r_{h_om}	0.01
	r_{I_bat}	0.01
Choice of constraints	$\lambda_{O_2,\mathrm{min}}^l$	1.5
	$I_\mathrm{St,min}$	5 A
Minimum penalty	c_min	1000

A.3 Air Supply Coupling Analysis

For the air supply coupling analysis, the fuel cell system model is linearized in several operating points of the compressor map by Taylor expansion. The resulting linear state-space system has the following form:

$$\dot{\mathbf{x}}(t) = \mathbf{A}\mathbf{x}(t) + \mathbf{B}\mathbf{u}(t) \tag{A.1}$$

$$\mathbf{y}(t) = \mathbf{C}\mathbf{x}(t) + \mathbf{D}\mathbf{u}(t) \tag{A.2}$$

The matrix A, B, C and D can be found by utilizing Taylor expansion as given in (A.3). The operating point $(\mathbf{u}_{\text{op}}, \mathbf{x}_{\text{op}})$ is found by solving the nonlinear steady-state model of the fuel cell system with a fixed operating point in the compressor map $(\dot{m}_{\text{cr}}, \Pi)$ and an oxygen excess ratio λ_{O_2} of 2.

$$\begin{aligned} A &= \frac{df(\mathbf{x}(t), \mathbf{u}(t))}{d\mathbf{x}}|_{\mathbf{u}_{\text{op}}, \mathbf{x}_{\text{op}}} & B &= \frac{df(\mathbf{x}(t), \mathbf{u}(t))}{d\mathbf{u}}|_{\mathbf{u}_{\text{op}}, \mathbf{x}_{\text{op}}} \\ C &= \frac{dg(\mathbf{x}(t), \mathbf{u}(t))}{d\mathbf{x}}|_{\mathbf{u}_{\text{op}}, \mathbf{x}_{\text{op}}} & D &= \frac{dg(\mathbf{x}(t), \mathbf{u}(t))}{d\mathbf{u}}|_{\mathbf{u}_{\text{op}}, \mathbf{x}_{\text{op}}} \end{aligned} \tag{A.3}$$

In Table A.8, three representative operating points are chosen in order to analyze the system. They are located in different areas of the compressor map. The eigenvalues λ_{min} and λmax are far apart from each other indicating a stiff system.

Tab. A.8: Representative operating points for analysis of linearized system.

OP	$P_{fc,net}$[kW]	$\Pi[-]$	$\dot{m}_{\text{cr}}[\frac{\text{kg}}{\text{s}}]$	$\lambda_{O_2}[-]$	λ_{min}	λ_{max}
1	4.12	11 1.2	0.018	8	−0.67	−147.59
2	30.86	1.7	0.04	2	−1.20	−145.83
3	49.17	2	0.055	1.6	−1.45	−146.40

The transfer function of the MIMO system of the air supply in the frequency domain is given in (A.4). Inputs to the system are the compressor voltage U_{cp} and the back pressure valve opening h_{om} and the outputs are the air mass flow rate $\dot{m}_{\text{cr}}$ and the pressure ratio Π.

$$\begin{pmatrix} \dot{m}_{\text{cr}} \\ \Pi \end{pmatrix} = \underbrace{\begin{pmatrix} G_{11}(s) & G_{12}(s) \\ G_{21}(s) & G_{22}(s) \end{pmatrix}}_{G(s)} \begin{pmatrix} U_{\text{cp}} \\ h_{\text{om}} \end{pmatrix} \tag{A.4}$$

The relative gain array can be used to quantify the air supply coupling [81]. The steady-state RGA is calculated by (A.5). The columns of the RGA matrix relate to the inputs and the rows relate to the outputs. The results for a few operating points are presented in Table A.9. All entries of the RGA are positive for the air supply. Thus, if the values are distributed evenly (close to 0.5), it indicates strong coupling. If one value is close to 1 and the others are close to 0, it indicates weak coupling.

The compressor flow $\dot{m}_{\mathrm{cr}}$ and pressure ratio Π controlled by the compressor voltage U_{Cp} and h_{OM} are strongly coupled. From the table, it can be seen that the influence of the compressor voltage U_{cp} on $\dot{m}_{\mathrm{cr}}$ rises with increasing $\dot{m}_{\mathrm{cr}}$ and decreasing Π (indicated by a rising value of the upper left entry). In contrast, the influence of the back pressure valve opening h_{OM} on the pressure ratio Π rises with increasing $\dot{m}_{\mathrm{cr}}$ and decreasing Π (indicated by a rising value of the lower right entry).

$$RGA = G(0) \cdot \left(G^{-1}(0)\right)^{T} \tag{A.5}$$

Tab. A.9: Relative gain array for different operating points in the compressor map.

$\dot{m}_{\mathrm{cr}}$	$\Pi = 1.7$		$\dot{m}_{\mathrm{cr}}$	$\Pi = 2$	
40 g/s	0.32	0.68	50 g/s	0.33	0.67
	0.68	0.32		0.67	0.33
50 g/s	0.43	0.57	60 g/s	0.44	0.56
	0.57	0.43		0.56	0.44
60 g/s	0.56	0.44	70 g/s	0.57	0.43
	0.44	0.56		0.43	0.57

Figure A.1 illustrates how the coupling varies for different operating points in the compressor map. The color illustrates the distance of the diagonal elements to 0.5. Therefore a low value indicates a high coupling and a large value indicates low coupling.

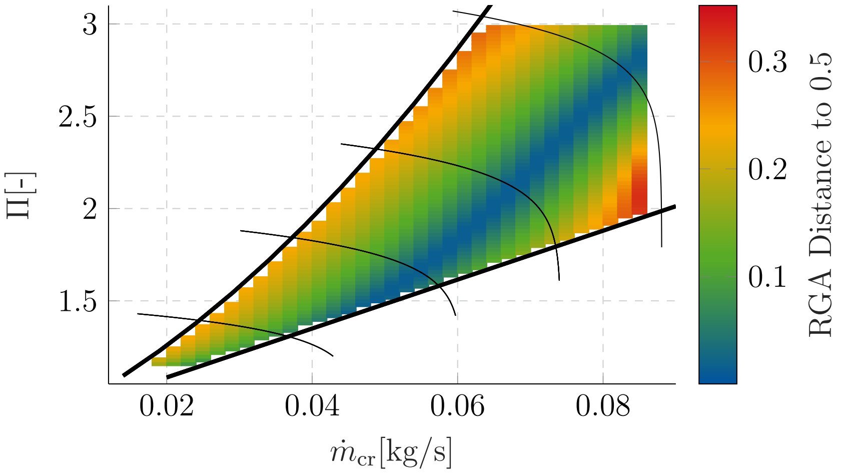

Fig. A.1: Coupling analysis of reduced air mass flow rate and pressure ratio based on relative gain array.

The largest coupling is in the middle of the compressor map. The results differs from the analysis by *Zhao et al.* [35]. However, their fuel cell system is analyzed for low pressure ratio Π and air mass flow rate $\dot{m}_{\mathrm{cr}}$. Moreover, the conclusion is the same in the sense that a decoupling control is necessary.

A.4 Sigmoid Reference Interpolation

In this thesis, a interpolation based on sigmoid functions is proposed. It is similar to the zero-order hold approach, but increases the mathematical conditioning for the optimal control problem at the time of a operating point change.

The value for a single reference trajectory denoted by the subscript j at time step k^l is given by (A.6). The formula is illustrated in Figure A.2 for a single reference trajectory. The black dashed line represents the reference trajectory passed from a higher level $\mathbf{y}^h_{\mathrm{ref}}(\cdot)$. The red dotted line illustrates the influence of a single reference value $y^h_{\mathrm{ref},j}(k^h)$ on the trajectory of the LLC $y^l_{\mathrm{ref},j}(\cdot)$ which is described by (A.6b). The blue solid line presents the resulting trajectory from the LLC and is described by (A.6a). The summation runs from $k^h = -1$ until $k^h = \left\lceil N^l_p \frac{T^l_{\mathrm{S}}}{T^h_{\mathrm{S}}} \right\rceil$ which is the upper bound of the prediction horizon of the LLC. It is worth noticing that the summation starts at $k^h = -1$ which means that the last value of the HLC output has to be stored.

Δt determines the steepness of the sigmoid function and is the only design parameter of the interpolation method. It is set to 20 ms which means that the step is completed by 66.7 % at that time. For $\Delta t \to 0$, the sigmoid interpolation converges against the zero-order hold interpolation.

$$y^l_{\mathrm{ref},j}(k^l) = \sum_{k^h=-1}^{\left\lceil \frac{T^l_{\mathrm{S}}}{T^h_{\mathrm{S}}} \cdot N^l_{\mathrm{P}} \right\rceil} y^l_{\mathrm{ref},j}(k^l|k^h) \tag{A.6a}$$

$$y^l_{\mathrm{ref},j}(k^l|k^h) = \frac{y^h_{\mathrm{ref},j}(k^h)}{1 + \exp\left(\frac{k^l - k^h \frac{T^h_{\mathrm{S}}}{T^l_{\mathrm{S}}}}{\Delta t}\right)} - \frac{y^h_{\mathrm{ref},j}(k^h)}{1 + \exp\left(\frac{k^l - (k^h+1) \frac{T^h_{\mathrm{S}}}{T^l_{\mathrm{S}}}}{\Delta t}\right)} \tag{A.6b}$$

In order to reduce the computational cost, (A.6) can be rewritten in matrix from. In (A.7) the reference trajectory $y^h_{\mathrm{ref},j}(k^h)$ from (A.6b) is factored out such that $f(k^l|k^h)$ is only

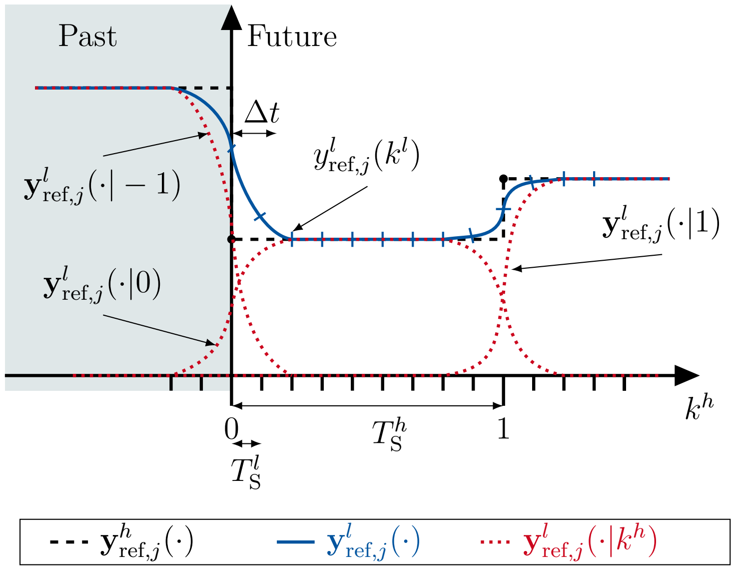

Fig. A.2: Detailed reference trajectory interpolation from the HLC to the LLC.

dependent on k^l and k^h.

$$y^l_{\text{ref},j}(k^l|k^h) = y^h_{\text{ref},j}(k^h)\underbrace{\left(\frac{1}{1+\exp\left(\frac{k^l-k^h\frac{T^h_{\text{S}}}{T^l_{\text{S}}}}{\Delta t}\right)} - \frac{1}{1+\exp\left(\frac{k^l-(k^h+1)\frac{T^h_{\text{S}}}{T^l_{\text{S}}}}{\Delta t}\right)}\right)}_{f(k^l|k^h)} \tag{A.7}$$

(A.7) can be inserted into (A.6a).

$$y^l_{\text{ref},j}(k^l) = \sum_{k^h=-1}^{\left\lceil \frac{T^l_{\text{S}}}{T^h_{\text{S}}}\cdot N^l_{\text{P}}\right\rceil} y^h_{\text{ref},j}(k^h) f^l(k^l|k^h) \tag{A.8}$$

Equation (A.8) gives the reference of the LLC $y^l_{\text{ref},j}(k^l)$ for one point in time k^l. Applying this formula to the whole trajectory $\mathbf{y}^l_{\text{ref},j}(.)$, it can be written in matrix form by (A.9). The resulting matrix $\mathbf{M}$ can be precalculated offline because it is independent of the trajectory $\mathbf{y}^h_{\text{ref},j}(\cdot)$.

$$\begin{aligned}
\mathbf{y}^l_{\text{ref},j}(\cdot) &= \mathbf{M}\mathbf{y}^h_{\text{ref},j}(\cdot)\\
\mathbf{M} &= \begin{pmatrix} f^l(0|-1) & f^l(0|0) & \dots & f^l(0|\left\lceil \frac{T^l_{\text{S}}}{T^h_{\text{S}}}\cdot N^l_{\text{P}}\right\rceil) \\ \vdots & \vdots & \ddots & \vdots \\ f^l(N^l_{\text{P}}|-1) & f^l(N^l_{\text{P}}|0) & \dots & f^l(N^l_{\text{P}}|\left\lceil \frac{T^l_{\text{S}}}{T^h_{\text{S}}}\cdot N^l_{\text{P}}\right\rceil) \end{pmatrix}\\
\mathbf{y}^h_{\text{ref},j}(\cdot) &= \left[\mathbf{y}^h_{\text{ref},j}(-1) \quad \mathbf{y}^h_{\text{ref},j}(0) \quad \dots \quad \mathbf{y}^h_{\text{ref},j}(\left\lceil \frac{T^l_{\text{S}}}{T^h_{\text{S}}}\cdot N^l_{\text{P}}\right\rceil)\right]^T
\end{aligned} \tag{A.9}$$

A.5 Influences of the Fuel Cell System Operating Point on the Efficiency

According to *Larminies et al.* [4, Chapter 4], the benefit of a pressure rise is conducted in this section for the given fuel cell system. Therefore, the impact of rising the pressure from nominal conditions p^0 to a pressure p_1 is conducted. Furthermore, it is assumed the the inlet pressure p_{IM} equals the cathode pressure p_{cat} and the air mass flow rate m_{cr} as well as the stack current I_{st} stay constant.

1. **Electrical power consumption of the compressor**: The electrical power consumption of the compressor depends on the pressure ratio $\Pi = \frac{p_1}{p^0}$ as given in (A.10). P_{cm} equals ΔP_{cm} because the pressure is raised from nominal conditions. The derivation can be found in Appendix A.6. The compressor efficiency η_{cp} is higher in the middle of the operating range and decreases towards the choke and surge boundaries of the compressor map (compare Figure 2.4).

$$P_{\mathrm{cm}} = \Delta P_{\mathrm{cm}} \approx c_{\mathrm{p}} \frac{T_{\mathrm{cp,in}}}{\eta_{\mathrm{cm}} \eta_{\mathrm{cp}}(\Pi, \dot{m}_{\mathrm{cr}})} (\Pi^{\frac{\gamma-1}{\gamma}} - 1) \dot{m}_{\mathrm{cr}} \tag{A.10}$$

2. **Fuel cell efficiency**: The stack power raises with increasing pressure p_1 as given in (A.11) due to the rising reversible voltage E_{rev} and the reduced activation loss ΔU_{act}. The formula is derived in Appendix A.7.

$$\Delta P_{\mathrm{st}} \approx I_{\mathrm{St}} \left(\frac{3 R_{\mathrm{uni}} T_{\mathrm{st}}}{4F} + \xi_{2c} T_{\mathrm{st}} + \xi_3 T_{\mathrm{st}} \right) \cdot \ln(\frac{p_1}{p^0}) \tag{A.11}$$

The power gain ΔP_{gain} of increasing the pressure can be stated as given in (A.12) whereat a pressure gain greater than zero indicates a benefit. According to *Larminies et al.* [4], the gain of increasing the pressure strongly depends on the depicted fuel cell system.

$$\Delta P_{\mathrm{gain}} = \Delta P_{\mathrm{st}} - \Delta P_{\mathrm{cm}} \tag{A.12}$$

The derived formulas give a valuable insight to the impact of the fuel cell system operating point on the fuel cell efficiency $\eta_{\mathrm{fcs,bus}}$. E.g., it can be seen that the power gain ΔP_{gain} increases for raising stack temperature T_{St} and electrochemical coefficients ξ_i. In order to get the quantitative evaluation of the efficiency $\eta_{\mathrm{fcs,bus}}$ depending on the operating point of the fuel cell system, a numerical analysis is conducted in Section 4.3.1.

A.6 Electrical Power Consumption for Pressure Increase

Increasing the pressure ratio across the compressor leads to an increasing electrical power consumption. In this section, the derivation for the results shown in (A.10) is presented. According to the model of the electric motor in Figure 3.2, the compressor voltage U_{cp} can be described as follow:

$$U_{\mathrm{cp}} = I_{\mathrm{cm}} R_{\mathrm{cm}} + k_{\mathrm{T}} \omega_{\mathrm{cp}} \tag{A.13}$$

The electrical power consumption as given in (3.22) can be reformulated by (A.14). The motor resistance R_{cm} is small such that the second term is dominant. Thus, the first term of the electrical power consumption P_{cm} is neglected.

$$P_{\mathrm{cm}} = U_{\mathrm{cp}} I_{\mathrm{cm}} = I_{\mathrm{cm}}^2 R_{\mathrm{cm}} + I_{\mathrm{cm}} k_{\mathrm{T}} \omega_{\mathrm{cp}} \approx I_{\mathrm{cm}} k_{\mathrm{T}} \omega_{\mathrm{cp}} \tag{A.14}$$

According to (3.14), the generated motor torque τ_{cm} equals the required compressor torque τ_{cp} for steady-state.

$$\tau_{\mathrm{cm}} = \eta_{\mathrm{cm}} k_{\mathrm{T}} I_{\mathrm{cm}} = \tau_{\mathrm{cp}} = c_{\mathrm{p}} \frac{T_{\mathrm{cp,in}}}{\omega_{\mathrm{cp}} \eta_{\mathrm{cp}}} (\Pi^{\frac{\gamma-1}{\gamma}} - 1) \dot{m}_{\mathrm{cr}} \tag{A.15}$$

The equation can be solved for I_{cm} as given in (A.16) and substituted in (A.14) as stated by (A.17).

$$I_{\mathrm{cm}} = c_{\mathrm{p}} \frac{T_{\mathrm{cp,in}}}{\eta_{\mathrm{cm}} k_{\mathrm{T}} \omega_{\mathrm{cp}} \eta_{\mathrm{cp}}} (\Pi^{\frac{\gamma-1}{\gamma}} - 1) \dot{m}_{\mathrm{cr}} \tag{A.16}$$

$$P_{\mathrm{cm}} \approx c_{\mathrm{p}} \frac{T_{\mathrm{cp,in}}}{\eta_{\mathrm{cm}} \eta_{\mathrm{cp}}} (\Pi^{\frac{\gamma-1}{\gamma}} - 1) \dot{m}_{\mathrm{cr}} \tag{A.17}$$

A.7 Stack Power for Pressure Increase

When the cathode pressure p_{cat} is increased, the efficiency of the fuel cell stack increases. In this section, the derivation of A.11 is given.

The voltage U_{fc} increases when the cathode pressure p_{cat} increases caused by two influences. Firstly, the reversible voltage E_{rev} in (3.5) raises and secondly the activation loss in (3.7) reduces. According to (3.6), the reversible voltage can be described by (A.18) with $p_{H_2} = p_{\text{cat}}$. Thus, we reformulate E_{rev} such that the cathode pressure p_{cat} is extracted.

$$\begin{aligned} E_{\text{rev}} &= E_{\text{rev}}^0 - k_{\text{t}}\left(T_{\text{st}} - T^0\right) + \frac{R_{\text{u}}T_{\text{st}}}{2F} \cdot \ln\left(p_{\text{cat}} \cdot \sqrt{p_{O_2}}\right) \\ &= E_{\text{rev}}^0 - k_{\text{t}}\left(T_{\text{st}} - T^0\right) + \frac{R_{\text{u}}T_{\text{st}}}{2F} \cdot \ln\left(p_{\text{cat}} \cdot \sqrt{X_{O_2,\text{out}}p_{\text{cat}}}\right) \\ &= E_{\text{rev}}^0 - k_{\text{t}}\left(T_{\text{st}} - T^0\right) + \frac{3R_{\text{u}}T_{\text{st}}}{4F} \cdot \ln\left(p_{\text{cat}}\right) + \frac{R_{\text{u}}T_{\text{st}}}{4F} \cdot \ln\left(X_{O_2,\text{out}}\right) \end{aligned} \tag{A.18}$$

The same reformulation can be done for the activation loss which is stated in (3.7) and (3.8). Thereby, only terms that relate to the cathode pressure p_{cat} are considered denoted by $\Delta U_{\text{act},p_{\text{cat}}}$.

$$\begin{aligned} \Delta U_{\text{act},p_{\text{cat}}} = \quad & -\xi_{2c}T_{\text{st}}\ln\left(p_{\text{cat}}9.174\cdot 10^{-7}\exp\left(\frac{-77}{T_{\text{st}}}\right)\right) \\ & -\xi_3 T_{\text{st}}\ln\left(X_{O_2,\text{out}}p_{\text{cat}}1.97\cdot 10^{-7}\cdot\exp\left(\frac{498}{T_{\text{st}}}\right)\right) \\ = \quad & -\xi_{2c}T_{\text{st}}\ln\left(p_{\text{cat}}\right) + \xi_{2c}T_{\text{st}}\ln\left(9.174\cdot 10^{-7}\exp\left(\frac{-77}{T_{\text{st}}}\right)\right) \\ & -\xi_3 T_{\text{st}}\ln\left(p_{\text{cat}}\right) + \xi_3 T_{\text{st}}\ln\left(X_{O_2,\text{out}}1.97\cdot 10^{-7}\cdot\exp\left(\frac{498}{T_{\text{st}}}\right)\right) \end{aligned} \tag{A.19}$$

The value of interest is the change in fuel cell voltage ΔU_{fc} when p_{cat} is increased from p^0 to p_1. Therefore, all constant term can be neglected and ΔU_{fc} is as given in (A.20) according to (3.4). Thereby, it is assumed that the output mole fraction of oxygen $X_{O_2,\text{out}}$ is independent of the cathode pressure p_{cat}.

$$\Delta U_{\text{fc}} \approx \left(\frac{3R_{\text{uni}}T_{\text{st}}}{4F} + \xi_{2c}T_{\text{st}} + \xi_3 T_{\text{st}}\right) \cdot \ln\left(\frac{p_1}{p^0}\right) \tag{A.20}$$

The change in stack power it is proportional to U_{fc} by the stack current I_{st} as given in (3.2).

$$\Delta P_{\text{st}} \approx I_{\text{st}}\left(\frac{3R_{\text{uni}}T_{\text{st}}}{4F} + \xi_{2c}T_{\text{st}} + \xi_3 T_{\text{st}}\right) \cdot \ln\left(\frac{p_1}{p^0}\right) \tag{A.21}$$

A.8 Further Results of High-Level Control Parameter Evaluation

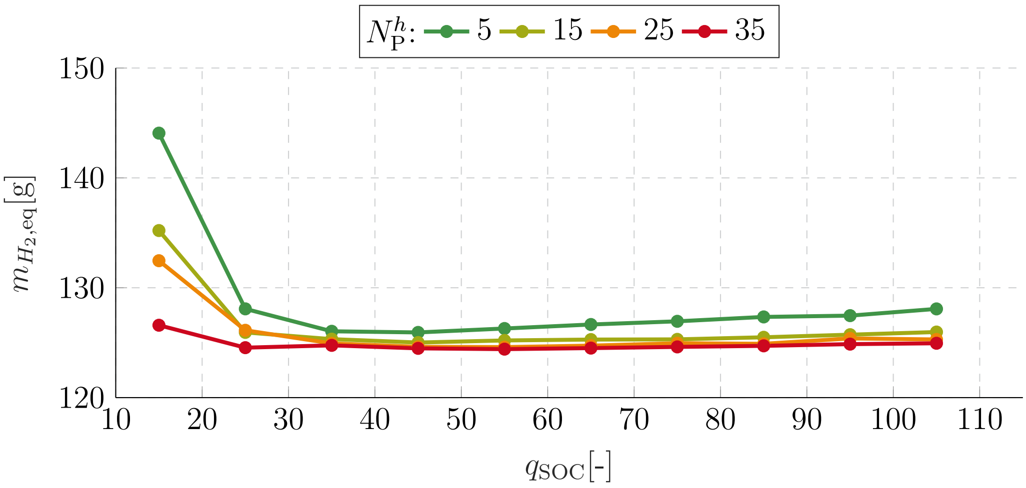

Fig. A.3: MPC parameter evaluation on NEDC driving cycle.

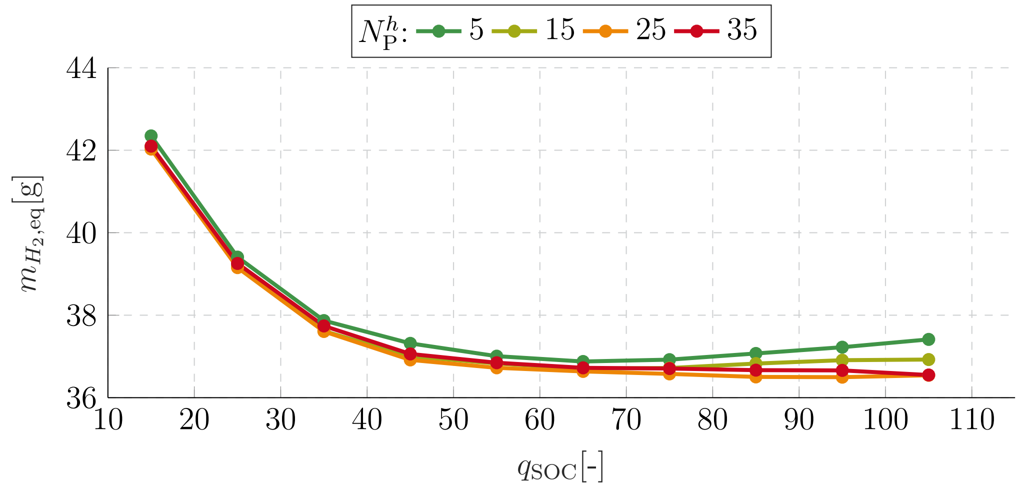

Fig. A.4: MPC parameter evaluation on Japanese 10-15 driving cycle.

Bibliography

[1] Dröge, Susanne. “The Paris Agreement 2015: turning point for the international climate regime”. In: *SWP Research Papers* (2016).

[2] Bundesministerium für Umwelt, Naturschutz und nukleare Sicherheit. *Klimaschutz in Zahlen.* 2018.

[3] Ahluwalia, Rajesh K. and Wang, Xiaohua. “Fuel cell systems for transportation: Status and trends”. In: *Journal of Power Sources* 177.1 (2008), pp. 167–176.

[4] Larminie, James. *Fuel cell systems explained.* 2nd ed. SAE International, 2006.

[5] Kim, Namwook; Cha, Sukwon, and Peng, Huei. “Optimal control of hybrid electric vehicles based on Pontryagin’s minimum principle”. In: *IEEE Transactions on Control Systems Technology* (2011), pp. 1279–1287.

[6] Rawlings, James B. and Mayne, David Q. *Model predictive control: Theory and design.* Nob Hill Publishing, 2009.

[7] Dirkes, Steffen. “Modellierung und modellbasierte Regelung eines Brennstoffzellenhybridfahrzeugs”. Master Thesis [unpublished, IRT-internal available]. RWTH Aachen, 2018.

[8] Chan, Ching Chue. “The state of the art of electric, hybrid, and fuel cell vehicles”. In: *Proceedings of the IEEE* 95.4 (2007), pp. 704–718.

[9] Pukrushpan, Jay T.; Stefanopoulou, Anna G., and Peng, Huei. *Control of fuel cell power systems: Principles, modeling, analysis and feedback design.* 2. printing. London: Springer, 2005.

[10] Töpler, Johannes and Lehmann, Jochen. *Wasserstoff und Brennstoffzelle: Technologien und Marktperspektiven.* Berlin: Springer Vieweg, 2014.

[11] Schmitt, Lukas. “Modell-Prädiktive Betriebsstrategie für ein Hybridfahrzeug”. Master Thesis [unpublished, IRT-internal available]. RWTH Aachen, 2019.

[12] Yi, Hyeon-Seop; Jeong, Jin-Beom; Cha, Suk-Won, et al. “Optimal component sizing of fuel cell-battery excavator based on workload”. In: *International Journal of Precision Engineering and Manufacturing-Green Technology* 5.1 (2018), pp. 103–110.

[13] Hu, Xiaosong; Murgovski, Nikolce; Johannesson, Lars Mardh, et al. “Optimal dimensioning and power management of a fuel cell/battery hybrid bus via convex programming”. In: *IEEE/ASME Transactions on Mechatronics* 20.1 (2015), pp. 457–468.

[14] Jain, Manu; Chriag, Desai, and Williamson, Sheldon S. “Genetic algorithm based optimal powertrain component sizing and control strategy design for a fuel cell hybrid electric bus”. In: *IEEE Vehicle Power.* 2009, pp. 980–985.

[15] Corbo, Pasquale; Migliardini, Fortunato, and Veneri, Ottorino. *Hydrogen fuel cells for road vehicles.* London: Springer London, 2011.

[16] Kongkanand, Anusorn; Subramanian, Nalini P.; Yu, Yingchao, et al. "Achieving high-power PEM fuel cell performance with an ultralow-Pt-content core–shell catalyst". In: *ACS Catalysis* 6.3 (2016), pp. 1578–1583.

[17] O'Hayre, Ryan P.; Cha, Suk-Won; Colella, Whitney G., et al. *Fuel cell fundamentals.* 2nd ed. Hoboken, New Jersey: John Wiley & Sons Inc, 2009.

[18] Puig, Vicenç; Rosich, Albert; Ocampo-Martinez, Carlos, et al. "Fault-tolerant explicit MPC of PEM fuel cells". In: *Conference on Decision and Control.* 2007, pp. 2657–2662.

[19] Grimsmann, Florian. "Auswirkungen des Ladeprofils auf das Lithium-Plating-Verhalten von Lithium-Ionen-Zellen". Master Thesis. University of Oldenburg, 2014.

[20] Kurzweil, Peter and Dietlmeier, Otto. *Elektrochemische Speicher: Superkondensatoren, Batterien, Elektrolyse-Wasserstoff, Rechtliche Rahmenbedingungen.* 2nd ed. Wiesbaden: Springer Vieweg, 2018.

[21] Englert, Tobias; Völz, Andreas; Mesmer, Felix, et al. "A software framework for embedded nonlinear model predictive control using a gradient-based augmented Lagrangian approach (GRAMPC)". In: *Optimization and Engineering* (2019).

[22] Diehl, Moritz and Groß, Sebastien. "Numerical Optimal Control". Lecture Notes. University of Freiburg, 2017.

[23] Bertsekas, Dimitri P. *Dynamic programming and optimal control.* 3. ed. Vol. 3. Athena scientific optimization and computation series. Belmont, Mass.: Athena Scientific, 2005.

[24] Bellman, Richard. "The theory of dynamic programming". In: *Bulletin of the American Mathematical Society* 60.6 (1954), pp. 503–515.

[25] Nocedal, Jorge and Wright, Stephen J. *Numerical optimization.* 2nd ed. New York: Springer, 2006.

[26] Wächter, Andreas and Biegler, Lorenz T. "On the implementation of an interior-point filter line-search algorithm for large-scale nonlinear programming". In: *Mathematical Programming* 106.1 (2006), pp. 25–57.

[27] Bertsekas, Dimitri P. *Constrained optimization and Lagrange multiplier methods.* Academic press, 2014.

[28] Rockafellar, Ralph T. "Augmented Lagrange multiplier functions and duality in nonconvex programming". In: *SIAM Journal on Control* 12.2 (1974), pp. 268–285.

[29] Hairer, Ernst and Wanner, Gerhard. *Solving ordinary differential equations II: stiff and differential-algebraic problems.* 2., rev. ed. Vol. 14. Springer series in computational mathematics. Berlin, Heidelberg: Springer-Verlag Berlin Heidelberg, 2010.

[30] Barzilai, Jonathan and Borwein, Jonathan M. "Two-point step size gradient methods". In: *IMA journal of numerical analysis* 8.1 (1988), pp. 141–148.

[31] Abel, Dirk. *Regelungstechnik und Ergänzungen (Höhere Regelungstechnik): Umdruck zur Vorlesung.* 39th ed. Aachen: Mainz, 2018.

[32] Rawlings, James B.; Angeli, David, and Bates, Cuyler N. "Fundamentals of economic model predictive control". In: *51st IEEE Conference on Decision and Control*. 2012, pp. 3851–3861.

[33] Onori, Simona; Serrao, Lorenzo, and Rizzoni, Giorgio. *Hybrid electric vehicles: Energy management strategies*. 1st ed. London: Springer London, 2016.

[34] Yang, Woong-chul, Bates, Bradford, Fletcher, Nicholas, and Pow, Ric. "Control challenges and methodologies in fuel cell vehicle development," in: *SAE Technical Paper* (1998).

[35] Zhao, Dongdong; Blunier, Benjamin; Gao, Fei, et al. "Control of an ultrahigh-speed centrifugal compressor for the air management of fuel cell systems". In: *IEEE transactions on industry applications* 50.3 (2014), pp. 2225–2234.

[36] Garcia, Pablo; Torreglosa, Juan P.; Fernández, Luis M., et al. "Control strategies for high-power electric vehicles powered by hydrogen fuel cell, battery and supercapacitor". In: *Expert Systems with Applications* 40.12 (2013), pp. 4791–4804.

[37] Chen, Jian; Liu, Zhiyang; Wang, Fan, et al. "Optimal oxygen excess ratio control for PEM fuel cells". In: *IEEE Transactions on Control Systems Technology* 26.5 (2018), pp. 1711–1721.

[38] Gruber, Jorn and Bordons, Carlos. "Nonlinear MPC for the airflow in a PEM fuel cell using a Volterra series model". In: *Control Engineering Practice* 20.2 (2012), pp. 205–217.

[39] Liu, Shiqi; Bin, Yang; Li, Yaoyu, et al. "Hierarchical MPC control scheme for fuel cell hybrid electric vehicles". In: *IFAC PapersOnline* 51 (2018), pp. 646–652.

[40] Blunier, Benjamin and Miraoui, Abdellatif. "Air management in PEM fuel cells: State-of-the-art and prospectives". In: *2007 International Aegean Conference on Electrical Machines and Power Electronics*. 2007, pp. 245–254.

[41] Pischinger, Stefan; Schönfelder, Carsten, and Ogrzewalla, Jürgen. "Analysis of dynamic requirements for fuel cell systems for vehicle applications". In: *Journal of Power Sources* 154.2 (2006), pp. 420–427.

[42] Baroud, Zakaria; Benmiloud, Mohammed, and Benalia, Atallah. "Sliding mode controller for breathing subsystem on a PEM fuel cell system". In: *2015 3rd International Conference on Control, Engineering & Information Technology (CEIT)*. 2015, pp. 1–6.

[43] Chen, Qihong; Quan, Shuhai, and Xie, Changjun. "Nonlinear predictive control for oxygen supply of a fuel cell system". In: *International Joint Conference*. 2009, pp. 518–521.

[44] Arce, Alicia; Ramirez, Daniel R.; Del Real, A. J., et al. "Constrained explicit predictive control strategies for PEM fuel cell systems". In: *IEEE Conference on Decision and Control*. 2007, pp. 6088–6093.

[45] Rodatz, Paul; Paganelli, Gino, and Guzzella, Lino. "Optimizing air supply control of a PEM fuel cell system". In: *Proceedings of the American Control Conference*. Vol. 3. 2003, pp. 2043–2048.

[46] Hähnel, Christian. “Regelung zum effizienten Betrieb eines PEM-Brennstoffzellensystems”. Dissertation. Helmut-Schmidt-University, 2017.

[47] Vahidi, Ardalan; Stefanopoulou, Anna, and Peng, Huei. “Current management in a hybrid fuel cell power system: A model-predictive control approach”. In: *IEEE Transactions on Control Systems Technology* 14.6 (2006), pp. 1047–1057.

[48] Di Domenico, Domenico. and Fiengo, Giovanni. “Power split strategy for fuel cell hybrid electric system”. In: *Oil & Gas Science and Technology–Revue de l’Institut Français du Pétrole* 65.1 (2010), pp. 145–154.

[49] Odeim, Farouk; Roes, Jurgen, and Heinzel, Angelika. “Power management optimization of a fuel cell/battery/supercapacitor hybrid system for transit bus applications”. In: *IEEE Transactions on Vehicular Technology* 65.7 (2016), pp. 5783–5788.

[50] Corcau, Jenica-Ileana; Dinca, Liviu; Grigorie, Teodor Lucian, et al. “Fuzzy energy management for hybrid fuel cell/battery systems for more electric aircraft”. In: *Applied Mathematics and Computer Science.* 2017.

[51] Thounthong, Phatiphat; Raël, Stéphane, and Davat, Bernard. “Control strategy of fuel cell/supercapacitors hybrid power sources for electric vehicle”. In: *Journal of Power Sources* 158.1 (2006), pp. 806–814.

[52] Jiang, Qi; Bethoux, Olivier; Ossart, Florence, et al. “A-ECMS and SDP energy management algorithms applied to a fuel cell electric scooter”. In: *IEEE Vehicle Power and Propulsion Conference.* 2017, pp. 1–5.

[53] Zheng, Chunhua.; Xu, Guoqing, and Cha, Suk-Won. “Numerical comparison of ECMS and PMP-based optimal control strategy in hybrid vehicles”. In: *International Journal of Automotive Technology* 15.7 (2014), pp. 1189–1196.

[54] Bordons, Carlos; Ridao, Miguel A.; Perez, Antonio, et al. “Model predictive control for power management in hybrid fuel cell vehicles”. In: *IEEE Vehicle Power.* 2010, pp. 1–6.

[55] Josevski, Martina. “Predictive energy management of hybrid electric vehicles with uncertain torque demand forecast for on-road operation”. Disseration. RWTH Aachen, 2018.

[56] Murugesan, Karthik; Vijayachitra, S., and Gomathi, K. “Modeling of PEM fuel cell stack system using feed-forward and recurrent neural networks for automotive applications”. In: *International Journal of Engineering and Technology* 6 (2014), pp. 559–569.

[57] Heliocentris Academia International GmbH. *Hybrid Energy Lab-System.* URL: `http://heliocentrisacademia.com/portfolio-item/hybrid-energy-lab-system/` (visited on 04/14/2019).

[58] Amphlett, John C.; Baumert, Rob M.; Mann, Ronald F., et al. “Performance modeling of the Ballard Mark IV solid polymer electrolyte fuel cell I. Mechanistic model development”. In: *Journal of the Electrochemical Society* 142.1 (1995), pp. 1–8.

[59] Mannhardt, Jacob. “Nichtlineare Optimierung in einer Hierarchischen Modellprädiktiven Regelung eines Brennstoffzellen-Hybridsystems”. Bachelor Thesis [unpublished, IRT-internal available]. RWTH Aachen, 2018.

[60] Leonhardt, Steffen. “Mechatronische Systeme 1”. Lecture Notes. 2018.

[61] Jensen, J-P; Kristensen, A. F.; Sorenson, Spencer C., et al. *Mean value modeling of a small turbocharged diesel engine*. Ed. by SAE Technical Paper. 1991.

[62] Tremblay, Olivier; Dessaint, Louis-A, and Dekkiche, Abdel-Illah. “A generic battery model for the dynamic simulation of hybrid electric vehicles”. In: *IEEE Vehicle Power and Propulsion Conference*. 2007, pp. 284–289.

[63] Shepherd, Clarence M. “Design of primary and secondary cells II. An equation describing battery discharge”. In: *Journal of the Electrochemical Society* 112.7 (1965), pp. 657–664.

[64] Füting, Michael. “Modellierung und Betriebsoptimierung eines hybriden Energiespeichersystems (Bleiakkumulator und Brennstoffzelle) im Kontext eines regenerativen virtuellen Kraftwerks”. Master Thesis [unpublished, IRT-internal available]. RWTH Aachen, 2018.

[65] Rezaei, Amir and Burl, Jeffrey B. “Prediction of vehicle velocity for model predictive control”. In: *IFAC-PapersOnLine* 48 (2015), pp. 257–262.

[66] Li, Huan; Ravey, Alexandre; N’Diaye, Abdoul, et al. “Equivalent consumption minimization strategy for fuel cell hybrid electric vehicle considering fuel cell degradation”. In: *IEEE Transportation Electrification Conference*. 2017, pp. 540–544.

[67] Xu, Liangfei; Li, Jianqiu; Hua, Jianfeng, et al. “Optimal vehicle control strategy of a fuel cell/battery hybrid city bus”. In: *International Journal of Hydrogen Energy* 34.17 (2009), pp. 7323–7333.

[68] Tumuluri, Uma. “Nonlinear state estimation in polymer electrolyte membrane fuel cells”. PhD thesis. Cleveland State University, 2008.

[69] Vepa, Ranjan. “Adaptive state estimation of a PEM fuel cell”. In: *IEEE Transactions on Energy Conversion* 27.2 (2012), pp. 457–467.

[70] Niemeyer, Jens. “Modellprädiktive Regelung eines PEM-Brennstoffzellensystems”. Dissertation. Karlsruhe Institute of Technology, 2008.

[71] Griewank, Andreas and Walther, Andrea. *Evaluating derivatives: Principles and techniques of algorithmic differentiation*. 2nd ed. Philadelphia: Society for Industrial and Applied Mathematics, 2008.

[72] Andersson, Joel A. E.; Gillis, Joris; Horn, Greg, et al. “CasADi: a software framework for nonlinear optimization and optimal control”. In: *Mathematical Programming Computation* 11.1 (2019), pp. 1–36.

[73] Bartholomaeus, Ralf; Klingner, Matthias, and Lehnert, Martin. “Prediction of power demand for hybrid vehicles operating in fixed-route service”. In: *IFAC Proceedings Volumes* 41.2 (2008), pp. 5640–5645.

[74] Ciuffo, Biagio; Marotta, Alessandro; Tutuianu, Monica, et al. "The development of the world-wide harmonized test procedure for light duty vehicles (WLTP) and the pathway for its implementation into the EU legislation". In: *TRB Annual Meeting.* 2015.

[75] Sundstrom, Olle and Guzzella, Lino. "A generic dynamic programming Matlab function". In: *IEEE Control Applications, (CCA) Intelligent Control, (ISIC).* 2009, pp. 1625–1630.

[76] Guzzella, Lino and Sciarretta, Antonio. *Vehicle propulsion systems: Introduction to modeling and optimization.* 3rd ed. 2013. Berlin and Heidelberg: Springer, 2013.

[77] Fletcher, Tom; Thring, Rob, and Watkinson, Martin. "An energy management strategy to concurrently optimise fuel consumption & PEM fuel cell lifetime in a hybrid vehicle". In: *International Journal of Hydrogen Energy* 41.46 (2016), pp. 21503–21515.

[78] Lin, Chan-Chiao; Kim, Min-Joong; Peng, Huei, et al. "System-level model and stochastic optimal control for a PEM fuel cell hybrid vehicle". In: *Journal of dynamic systems, measurement, and control* 128.4 (2006), pp. 878–890.

[79] Bubna, Piyush; Brunner, Doug; Advani, Suresh G., et al. "Prediction-based optimal power management in a fuel cell/battery plug-in hybrid vehicle". In: *Journal of Power Sources* 195.19 (2010), pp. 6699–6708.

[80] Tianheng, Feng; Lin, Yang; Qing, Gu, et al. "A supervisory control strategy for plug-in hybrid electric vehicles based on energy demand prediction and route preview". In: *IEEE Transactions on Vehicular Technology* 64.5 (2015), pp. 1691–1700.

[81] Skogestad, Sigurd and Postlethwaite, Ian. *Multivariable feedback control: Analysis and design.* 2. ed., reprinted with corr. Chichester: Wiley, 2007.